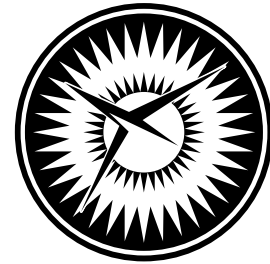


NASA/CR-2007-214879  
NIA Report No. 2007-07



NATIONAL  
INSTITUTE OF  
AEROSPACE



# Analysis of Composite Panel-Stiffener Debonding Using a Shell/3D Modeling Technique

*Ronald Krueger and James Ratcliffe  
National Institute of Aerospace (NIA), Hampton, Virginia*

*Pierre J. Minguet  
The Boeing Company, Philadelphia, Pennsylvania*

---

June 2007

## The NASA STI Program Office . . . in Profile

Since its founding, NASA has been dedicated to the advancement of aeronautics and space science. The NASA Scientific and Technical Information (STI) Program Office plays a key part in helping NASA maintain this important role.

The NASA STI Program Office is operated by Langley Research Center, the lead center for NASA's scientific and technical information. The NASA STI Program Office provides access to the NASA STI Database, the largest collection of aeronautical and space science STI in the world. The Program Office is also NASA's institutional mechanism for disseminating the results of its research and development activities. These results are published by NASA in the NASA STI Report Series, which includes the following report types:

- **TECHNICAL PUBLICATION.** Reports of completed research or a major significant phase of research that present the results of NASA programs and include extensive data or theoretical analysis. Includes compilations of significant scientific and technical data and information deemed to be of continuing reference value. NASA counterpart of peer-reviewed formal professional papers, but having less stringent limitations on manuscript length and extent of graphic presentations.
- **TECHNICAL MEMORANDUM.** Scientific and technical findings that are preliminary or of specialized interest, e.g., quick release reports, working papers, and bibliographies that contain minimal annotation. Does not contain extensive analysis.
- **CONTRACTOR REPORT.** Scientific and technical findings by NASA-sponsored contractors and grantees.

- **CONFERENCE PUBLICATION.** Collected papers from scientific and technical conferences, symposia, seminars, or other meetings sponsored or co-sponsored by NASA.
- **SPECIAL PUBLICATION.** Scientific, technical, or historical information from NASA programs, projects, and missions, often concerned with subjects having substantial public interest.
- **TECHNICAL TRANSLATION.** English-language translations of foreign scientific and technical material pertinent to NASA's mission.

Specialized services that complement the STI Program Office's diverse offerings include creating custom thesauri, building customized databases, organizing and publishing research results ... even providing videos.

For more information about the NASA STI Program Office, see the following:

- Access the NASA STI Program Home Page at [\*\*http://www.sti.nasa.gov\*\*](http://www.sti.nasa.gov)
- E-mail your question via the Internet to [\*\*help@sti.nasa.gov\*\*](mailto:help@sti.nasa.gov)
- Fax your question to the NASA STI Help Desk at (301) 621-0134
- Phone the NASA STI Help Desk at (301) 621-0390
- Write to:  
NASA STI Help Desk  
NASA Center for AeroSpace Information  
7115 Standard Drive  
Hanover, MD 21076-1320

NASA/CR-2007-214879  
NIA Report No. 2007-07



# Analysis of Composite Panel-Stiffener Debonding Using a Shell/3D Modeling Technique

*Ronald Krueger and James Ratcliffe*  
*National Institute of Aerospace (NIA), Hampton, Virginia*

*Pierre J. Minguet*  
*The Boeing Company, Philadelphia, Pennsylvania*

National Aeronautics and  
Space Administration

Langley Research Center  
Hampton, Virginia 23681-2199

Prepared for Langley Research Center  
under Contract NAS1-02117

---

June 2007

Trade names and trademarks are used in this report for identification only. Their usage does not constitute an official endorsement, either expressed or implied, by the National Aeronautics and Space Administration.

Available from:

NASA Center for AeroSpace Information (CASI)  
7115 Standard Drive  
Hanover, MD 21076-1320  
(301) 621-0390

National Technical Information Service (NTIS)  
5285 Port Royal Road  
Springfield, VA 22161-2171  
(703) 605-6000

# ANALYSIS OF COMPOSITE PANEL-STIFFENER DEBONDING USING A SHELL/3D MODELING TECHNIQUE

Ronald Krueger<sup>1</sup>, James Ratcliffe<sup>1</sup> and Pierre J. Minguet<sup>2</sup>

## ABSTRACT

Interlaminar fracture mechanics has proven useful for characterizing the onset of delaminations in composites and has been used successfully primarily to investigate onset in fracture toughness specimens and laboratory size coupon type specimens. Future acceptance of the methodology by industry and certification authorities, however, requires the successful demonstration of the methodology on the structural level. For this purpose, a panel was selected that is reinforced with stiffeners. Shear loading causes the panel to buckle, and the resulting out-of-plane deformations initiate skin/stiffener separation at the location of an embedded defect. A small section of the stiffener foot, web and noodle as well as the panel skin in the vicinity of the delamination front were modeled with a local 3D solid model. Across the width of the stiffener foot, the mixed-mode strain energy release rates were calculated using the virtual crack closure technique. A failure index was calculated by correlating the results with a mixed-mode failure criterion of the graphite/epoxy material. Computed failure indices were compared to corresponding results where the entire web was modeled with shell elements and only a small section of the stiffener foot and panel were modeled locally with solid elements. Including the stiffener web in the local 3D solid model increased the computed failure index. Further including the noodle and transition radius in the local 3D solid model changed the local distribution across the width. The magnitude of the failure index decreased with increasing transition radius and noodle area. For the transition radii modeled, the material properties used for the noodle area had a negligible effect on the results. The results of this study are intended to be used as a guide for conducting finite element and fracture mechanics analyses of delamination and debonding in complex structures such as integrally stiffened panels.

## 1. INTRODUCTION

Many composite components in aerospace structures are made of flat or curved panels with co-cured or adhesively bonded frames and stiffeners. Recent studies focused on the investigation of the debonding mechanism and included testing of skin/stiffener panels and failure analysis using shell models [1-4]. Over the last decade, a consistent step-wise approach has been developed which uses experiments to detect the failure mechanism, computational stress analysis to determine the location of first matrix cracking and computational fracture mechanics to investigate the potential for delamination growth. Testing of thin-skin stiffened panels designed for use in pressurized aircraft fuselages has shown that bond failure at the tip of the frame flange is an important and very likely failure mode [5]. Comparatively, simple specimens consisting of a stiffener flange bonded onto a skin have been developed to study skin/stiffener debonding [6-8]. The failure that initiates at the tip of the flange in these specimens is nearly identical to the failure observed in the full-scale panels and the frame pull-off specimens [7, 9, 10]. A methodology based on fracture mechanics [11] has been used

---

<sup>1</sup> National Institute of Aerospace (NIA), 100 Exploration Way, Hampton, VA 23666, resident at Durability, Damage Tolerance and Reliability Branch, NASA Langley Research Center, MS 188E, Hampton, VA, 23681.

<sup>2</sup> The Boeing Company, Philadelphia, Pennsylvania

successfully to investigate the onset and growth of delaminations in composites, and has been used with limited success primarily to investigate delamination onset and debonding in simple characterization specimens and laboratory size coupon type specimens [9, 10]. Future acceptance of the methodology by industry and certification authorities, however, requires the successful demonstration of the methodology on a structural level.

For the demonstration of the methodology on the structural level, a stiffened panel, as shown in Figure 1, had been analyzed previously [12, 13]. The square (1016 mm x 1016 mm) panel made of IM7/8552 carbon/epoxy tape is reinforced with three stiffeners made of IM7/8552 carbon/epoxy plain weave fabric. The material properties are given in Table 1. Other details will be discussed in the following sections. During manufacturing, an artificial defect of about 82 mm in length was placed at the termination of the center stiffener. The stiffened panel was bolted to a steel picture frame and subjected to shear loading as shown in Figure 1a. The shear loading caused the panel to buckle as shown in Figure 1a. The resulting out-of-plane deformation caused skin/stiffener separation to initiate at the location of the artificial defect. A typical finite element model is shown in Figure 1b [12, 13]. A small section of the stiffener foot and the panel skin in the vicinity of the embedded defect were modeled with a local 3D solid model as shown in the enlargement in Figure 1b. The mixed-mode strain energy release rates were calculated using the virtual crack closure technique [14, 15] across the width of the stiffener foot. A failure index was calculated by correlating the results with the mixed-mode failure criterion of the graphite/epoxy material [12, 13].

The objective of the current research was to study the effect of the fidelity of the local 3D finite element model on the computed mixed-mode strain energy release rates and the failure index. In the original model, shell elements represented the skin and stiffener foot [12, 13]. Stiff beam elements served as multi point constraints to connect the skin and the stiffener as shown in Figure 2a. In previous studies, a model was introduced where only the stiffener foot and skin were included in a local 3D model, while the web and hat were modeled with shell elements as shown in Figure 2b. The illustrations in Figure 2 are cross sections of the local 3D finite element model [12, 13]. In the current set of analyses, these models were used for a mesh refinement study across the width of the stiffener foot. In a new set of models, as shown in Figure 2c, the stiffener web was included in the local solid model. Another set of models included the transition radius between the web and foot as well as the detailed noodle region in the local solid model as shown in Figure 2d. The triangular region underneath the web, where the stiffener connects to the skin, is usually referred to as a *noodle*. The stiffener web, radius and noodle were included in the model in order to study the effect of detailed modeling on the failure index distribution across the width of the stiffener foot. The stiffener hat, modeled with shell elements, was kept unchanged.

In this paper, failure indices were calculated at the delamination front for different modeling approaches:

- Three different options in ABAQUS® for modeling the contact in the plane of delamination were studied using the models shown in Figure 2b
- The effect of introducing and modeling a resin layer at the delaminated interface was studied using the models shown in Figure 2b
- Mesh refinement studies across the width of the stiffener foot were performed using models as shown in Figure 2b

- Mesh refinement studies across the width of the stiffener foot were performed using models which included a 3D representation of the web as shown in Figure 2c
- Mesh refinement studies across the width of the stiffener foot were performed using models which included a 3D representation of the web, the noodle and the transition radius as shown in Figure 2d
  - Four different transition radii were studied
  - Two different materials in the noodle region were studied

A list of all models used is provided in Tables 2 and 3. The results of this study are intended to be used as a guide for modeling structures such a post-buckled skin/stiffener panels containing delaminations. The current research complements previous studies [12, 13].

## 2. METHODOLOGY

### 2.1. Linear Elastic Fracture Mechanics

Linear elastic fracture mechanics has proven useful for characterizing the onset and growth of delamination in composite laminates [11, 16]. When using fracture mechanics, the total strain energy release rate,  $G_T$ , is calculated along the delamination front. The term,  $G_T$ , consists of three individual components, as shown in Figure 3a. The first component,  $G_I$ , arises due to interlaminar tension. The second component,  $G_{II}$ , arises due to interlaminar sliding shear (shear stresses parallel to the plane of delamination and perpendicular to the delamination front). The third component,  $G_{III}$ , arises due to interlaminar scissoring shear (shear stresses parallel to the plane of delamination and parallel to the delamination front). The calculated  $G_I$ ,  $G_{II}$ , and  $G_{III}$  components are then compared to interlaminar fracture toughness values in order to predict delamination onset or growth. The interlaminar fracture toughness values are determined experimentally over a range of mode mixity from pure mode I loading to pure mode II loading [17-19].

A quasi static mixed-mode fracture criterion is determined by plotting the interlaminar fracture toughness,  $G_c$ , versus the mixed-mode ratio,  $G_{II}/G_T$ . The fracture criteria is generated experimentally using pure Mode I ( $G_{II}/G_T=0$ ) Double Cantilever Beam (DCB) tests, pure Mode II ( $G_{II}/G_T=1$ ) four point End-Notched Flexure (4ENF) tests, and Mixed Mode Bending (MMB) tests of varying ratios of  $G_I$  and  $G_{II}$ . A typical fracture criterion is presented in Figure 3b for IM7/8852 carbon epoxy material. A fracture criterion was suggested by Benzeggah and Kenane [20] using a simple mathematical relationship between  $G_c$  and  $G_{II}/G_T$

$$G_c = G_{Ic} + (G_{IIc} - G_{Ic}) \cdot \left( \frac{G_{II}}{G_T} \right)^\eta \quad (1)$$

In this expression  $G_{Ic}$  and  $G_{IIc}$  are the experimentally-determined fracture toughness data for mode I and II as shown in Figure 3b [21]. The factor  $\eta$  was determined by a curve fit using the Levenberg-Marquardt algorithm in KaleidaGraph<sup>TM</sup> [22], which yields

$$G_c = 207.7 + 1126.8 \cdot \left( \frac{G_{II}}{G_T} \right)^{4.46} . \quad (2)$$

Fracture initiation is expected when, for a given mixed mode ratio  $G_{II}/G_T$ , the calculated total energy release rate,  $G_T$ , exceeds the interlaminar fracture toughness,  $G_c$ . Although several specimens have been suggested for the measurement of the mode III interlaminar fracture toughness property [23-25], an interaction criterion incorporating the mode III shear, however, has not yet been established. The edge-cracked torsion test (ECT) is being considered for standardization as a pure mode III test [26, 27].

For three-dimensional analysis, which also yields results for the scissoring mode  $G_{III}$ , a modified definition is introduced where  $G_S$  denotes the sum of the in-plane shearing components  $G_{II}+G_{III}$  [12, 13]. This is necessary since a mixed-mode failure criterion, which accounts for all three modes, is currently not available. For analyses where  $G_{III}=0$ , this definition is equal to the commonly used definition of the mixed mode ratio,  $G_{II}/G_T$  mentioned above.

To determine failure along the delamination front, the critical energy release rate  $G_c$  is calculated using equation (2) with  $G_{II} = G_S$  at each point along the delamination front. Subsequently the failure index  $G_T/G_c$  is determined from the computed total energy release rate,  $G_T$ , and the critical energy release rate  $G_c$  with the assumption that delamination propagation occurs for

$$\frac{G_T}{G_c} \geq 1. \quad (3)$$

## 2.2. Analysis Tools

### 2.2.1 Virtual Crack Closure Technique

A variety of methods are used in the literature to compute the strain energy release rate based on results obtained from finite element analysis. For delaminations in laminated composite materials where the failure criterion is highly dependent on the mixed-mode ratio (as shown in Figure 3b) the virtual crack closure technique (VCCT) [14, 15] has been most widely used for computing energy release rates. VCCT calculations using continuum (2D) and solid (3D) finite element analyses provide the mode separation required when using the mixed-mode fracture criterion.

The mode I, and mode II components of the strain energy release rate,  $G_I$ ,  $G_{II}$  are computed using VCCT as shown in Figure 4a for a 2D four-noded element. The terms  $X'_i$ ,  $Z'_i$  are the forces at the crack tip at nodal point  $i$  and  $u'_\ell$ ,  $w'_\ell$  and  $u'_{\ell*}$ ,  $w'_{\ell*}$  are the displacements at the corresponding nodal points  $\ell$  and  $\ell^*$  behind the crack tip. Note that  $G_{III}$  is identical to zero in the 2D case. For geometric nonlinear analysis where large deformations may occur, both forces and displacements obtained in the global coordinate system need to be transformed into a local coordinate system ( $x'$ ,  $z'$ ) which originates at the crack tip as shown in Figure 4a. The local crack tip system defines the tangential ( $x'$ , or mode II) and normal ( $z'$ , or mode I) coordinate directions at the crack tip in the deformed configuration. The extension to 3D is straight forward as shown in Figure 4b and the total energy release rate  $G_T$  is calculated from the individual mode components as  $G_T = G_I + G_{II} + G_{III}$ . For the two-dimensional case shown in Figure 4a  $G_{III} = 0$ .



### 2.2.2 A Global/Local Shell 3D Modeling Technique

Built-up structures are traditionally modeled and analyzed using plate or shell finite elements, as shown in Figure 1b, to keep the modeling and computational effort affordable. Computed mixed mode strain energy release rate components, however, depend on many variables. These variables include element type, order of the shape functions and shear deformation assumptions, kinematic constraints in the neighborhood of the delamination front, and continuity of material properties and section stiffnesses in the vicinity of the debond when delaminations or debonds are modeled with plate or shell finite elements [28-30]. These problems may be avoided by using three-dimensional models. Since many layers of brick elements through the thickness are often necessary to model the individual plies, the size of finite element models required for accurate analyses may become prohibitively large.

For detailed modeling and analysis of the delaminations, the shell/3D modeling technique will reduce the modeling time compared to that required to run a fully three-dimensional finite element model. The technique will also reduce computational time because only a relatively small section of the mesh needs to be modeled with solid elements, minimizing the overall size of the model. The technique combines the accuracy of the full three-dimensional solution with the computational efficiency of a plate or shell finite element model. The technique has been demonstrated for various applications such as fracture toughness characterization specimens [31, 32], on the coupon level for the skin/stiffener separation specimen [33, 34] and in related studies for skin/stiffener separation [12, 13]. Figure 1b illustrates the regions within the stiffened panel that are modeled with shells and solid elements.

## 3. FINITE ELEMENT MODELING

In the current study, a finite element analysis of the three-stiffener panel shown in Figure 1b was conducted. The load frame and the three-stiffener panel were modeled with beam and shell elements. Initially a small section of the stiffener and the panel skin in the vicinity of the embedded defect was modeled with a local 3D model. Only the stiffener foot and skin were included in a local 3D model, while the web and hat were modeled with shell elements as shown in Figure 2b. In a new set of models, as shown in Figure 2c, the stiffener web was included in the local solid model. Another set of models included the transition radius between the web and foot as well as the detailed noodle region in the local solid model as shown in Figure 2d. The triangular region underneath the web, where the stiffener connects to the skin, is usually referred to as a *noodle*. The stiffener web, radius and noodle were included in the model in order to study the effect of detailed modeling on the failure index distribution across the width of the stiffener foot. For all analyses, the stiffener hat was modeled with shell elements.

### 3.1 Global Shell Model of Stiffener Stiffened Panel

The global model includes the steel load frame and attachments, the panel made of graphite/epoxy prepreg tape, and the stiffeners made of graphite/epoxy fabric, as shown in Figure 5. The outer steel load frame and the attachment bolts were modeled with beam elements (ABAQUS<sup>®</sup> element type B21), as shown in Figure 5a [35]. The inner steel load frame, which overlaps the panel edge, was modeled with shell elements (ABAQUS<sup>®</sup> element type S4). Shell elements were also used to model the panel bay, the reinforced panel bay, and the reinforced

panel perimeter, as shown in Figure 5a. The stiffener components, such as the foot, web and hat as shown in Figure 5b, were modeled with shell elements. Material data are given in Table 1 (supplied by Boeing).

A detail of the global finite element model in the vicinity of the stiffener termination is shown in Figure 6. The stacking sequence for the different skin/stiffener components are included in Figure 6. In the detail, it is shown that the panel skin and the stiffener foot are modeled as separate entities. The S4 shell elements are located at the panel skin and stiffener foot respective mid-planes. The shell elements are connected by beam elements (ABAQUS® element type B31 modeled as steel) to provide point-to-point constraints between the two surfaces [36]. Additional detail is provided in Figure 2a. In the section containing the artificial defect, the beam elements were replaced by gap elements (ABAQUS® element type GAPUNI). The gap elements allow the modeling of contact between two nodes. The nodes can be in contact (gap closed), which prevents element interpenetration or separated (gap open) which allows the skin/stiffener separation [35].

In preparation for the global/local modeling approach, shell elements representing the foot of the stiffener and the panel were removed from a small section,  $c$ , of the original shell model around the center stiffener termination, as shown in Figure 7. These shell elements lying within the region bounded by the edges **PNLLEFT**, **PNLBOT**, **PNLRGHT**, **PNLEND** and **STRFOOT**, **PNLFRNT** were replaced by solid elements to model the panel skin and stiffener foot. Additional shell elements lying within the region bounded by **STRFRNT**, **STRHAT** and **STREND** were replaced for certain models by solid elements to model the stiffener web. The shell elements used to model the stiffener hat, however, were kept in place. At the boundaries, the shell edges shown were used to connect the shell model with the local 3D solid model. The connection was accomplished using the shell to solid coupling option in ABAQUS®, which allows the connection between non-conforming shell and solid models. The coupling option uses a set of internally defined distributing coupling constraints to couple the motion of a row of nodes along the edge of the shell model to the motion of a set of nodes defined on a surface of the solid model [35].

### 3.2 Local 3D Model of the Stiffener Foot and Panel Skin

#### 3.2.1 Delamination Modeled at Skin/Stiffener interface

The local 3D model of the stiffener foot and panel skin was generated using brick elements (ABAQUS® element type C3D8I) and consisted of an intact section and a delaminated section with a fine mesh around the delamination front. An example is shown in Figure 8a. Surfaces **FRONT1**, **FRONT2**, **LEFT2**, **RIGHT2**, **REAR1**, **REAR2** and **SOLTOP** were defined in ABAQUS® on the outer faces of the 3D model to provide a connection with the global shell model. The artificial defect is located at the bondline between the stiffener foot and the panel as shown in Figure 8b. This defect was treated as a delamination and modeled as a discrete discontinuity using two unconnected nodes with identical coordinates on each side of the delamination. Since the delamination occurs at an interface between materials with dissimilar properties, care must be exercised in interpreting the values for  $G_I$  and  $G_{II}$  obtained using the virtual crack closure technique. For interfacial delaminations between two differing orthotropic solids the observed oscillatory singularity at the crack tip becomes an issue for small element lengths [37, 38]. Hence, a value of crack tip element length,  $\Delta a$ , was chosen (approximately one

ply thickness) in the range over which the strain energy release rate components exhibit a reduced sensitivity to the value of  $\Delta a$ .

A refined mesh was used along the stiffener boundary in order to capture edge effects as shown in Figure 8b. Contact was modeled between the delaminated surfaces to avoid interpenetration during the analysis using the finite sliding and small sliding options as well as gap elements available in ABAQUS<sup>®</sup> [35]. ABAQUS<sup>®</sup>/Standard provides several possibilities for modeling contact. One is a small-sliding formulation in which the contacting surfaces can undergo only relatively small sliding relative to each other but arbitrary rotation of the surfaces is permitted. Another is the more general finite-sliding formulation where separation and sliding of finite amplitude and arbitrary rotation of the surfaces may arise. Gap elements may also be used to define contact between two nodes. The contact behavior is defined by the initial clearance of the gap and the contact direction. Gap elements allow for the nodes to be in contact (gap closed) or separated (gap open) [35].

Four elements over the thickness were used to model the foot of the stiffener made of carbon/epoxy fabric as shown in Figure 8b. The  $-45^\circ$  skin ply made from carbon/epoxy tape which is adjacent to the plane of the delamination was modeled with one element. The remaining 10 plies of carbon/epoxy tape were modeled with three elements over the thickness as shown in Figure 8b. Local 3D models with this type of mesh in the thickness direction are referred to as *L0* (see also Table 2).

### **3.2.2 Delamination Modeled at the Midplane of a Resin Layer at the Skin/Stiffener Interface**

Two different local 3D models of the stiffener foot and panel skin containing an artificial resin layer at the interface were generated. As the delamination exists in a homogeneous isotropic material (the resin interface layer) the oscillatory singularity at the crack tip - as mentioned above - does not exist [37]. For convenience, the delamination was assumed to exist centrally within the resin layer. Therefore, the resin was modeled with two layers of elements with the delamination located between the two layers. The thickness of the resin layer was assumed to be 0.127 mm (provided by Boeing). Resin or adhesive properties were assigned to the elements forming these layers which are summarized in Table 1. The strain energy release rate distribution calculated across the delamination front was compared to the distribution calculated from models without a resin layer. The details of the local models are shown in Figure 9. For the mesh shown in Figure 9a, the total number of elements in the local 3D model was kept constant by keeping the number of elements over the thickness the same. Keeping the number of elements constant appeared sensible to prevent the local 3D model from getting too large. Therefore, only the number of plies grouped into each element layer over the thickness was modified. The local 3D model of the stiffener foot and panel skin shown in Figure 9a is referred to as *L1*. For the mesh shown in Figure 9b, the artificial resin layer was modeled by adding two layers of elements to the original model (Figure 8), one on each side of the delaminated interface. Adding layers of elements conserved the original fidelity of the model over the skin panel and stiffener foot laminate thickness. However, it increased the total number of elements in the local 3D model. The model is referred to as *L2*.

### 3.3 Local 3D Model of the Panel Skin, Stiffener Foot and Web

The modeling fidelity was increased by including the stiffener web in the local 3D model as shown in Figure 10. The local 3D model shown consisted of two separately meshed sections: The stiffener web and the panel skin/stiffener foot. The web was modeled with eight brick elements (ABAQUS® element type C3D8I) over the thickness. The section of the panel skin and stiffener foot including the delamination was modeled with a resin layer on each side of the delaminated interfaces as discussed above for model *L1*. The two models are connected to each other using multi point constraints (ABAQUS® MPC option \*TIE). The multi point constraints are used to tie two surfaces together for the duration of a simulation, which makes the translational and rotational motion equal for a pair of surfaces. Nodes on the slave surface (defined by the user) are constrained to have the same motion as the point on the master surface (defined by the user) to which it is closest [35].

### 3.4 Local 3D Model of the Panel Skin, Stiffener Foot and Web Including the Noodle and Transition Radius

The modeling fidelity was increased further by including the noodle region and transition radius in the local 3D model as shown in Figure 11. As above, the local 3D model shown consisted of two separately meshed sections which are connected with tie constraints: The model of the T-stiffener including the web, noodle region and transition radius as shown in the cross section of Figure 11a and the model of panel skin and delaminated interface as shown in Figure 11b.

The detailed discretization of the noodle region required the use of triangular prism elements at the corner of the noodle. This element type was also used in the transition region between the flange foot and stiffener web (Figure 11b). Additionally, the mesh in the noodle region was highly irregular. The calculation of mixed-mode strain energy release rates across the width of the specimen using VCCT, however, requires a conforming mesh on both sides of the plane of delamination.

In order to account for the different modeling requirements such as detailed modeling of the noodle region, conforming meshes on both sides of the plane of delamination for VCCT and simple mesh generation using existing routines, an additional resin layer was introduced at the skin/stiffener interface as discussed above (Figure 11b).

#### 3.4.1 Solid Model of the Panel Skin and Delaminated Interface

The solid model of the stiffener foot and delamination consisted of brick elements (ABAQUS® element type C3D8I) and included an intact section and a delaminated section with a fine mesh around the delamination front, as shown in Figure 12. The model corresponds to the models discussed in Section 3.2. The resin was modeled with two layers of elements with the delamination located between the two layers. Resin or adhesive properties were assigned to the elements forming this layer and are summarized in Table 1. The -45° skin ply (carbon/epoxy tape) which is adjacent to the plane of delamination, was modeled with one element through the thickness. The remaining 10 plies of carbon/epoxy tape were modeled with two elements over the thickness as shown in Figure 12b. The model is referred to as *L3*.

### 3.4.2 Solid Models of the T-stiffener Including the Web, the Noodle and Different Transition Radii

Solid models representing the stiffener foot, the web and the noodle region were generated. Since the exact transition radius of the test specimens was not known, the influence of detailed local 3D modeling on computed strain energy release rates was studied. In this case, a number of models were generated with different foot/web transition radii. Four models were generated with radius values of 0.254 mm, and 0.711 mm, 2.54 mm and 5.08 mm. Models with radii 2.54 mm and 0.711 mm were thought to correspond to actual values (Figures 13a and b). The models for the radii 0.254 mm and 5.08 mm are shown in Figures 14a and b respectively. The small radius 0.254 mm was selected to determine if the computed results were similar to those obtained from the model discussed in section 3.3 which did not include the radius and noodle. The larger radius 5.08 mm was arbitrarily chosen as an upper limit. It did not appear to be meaningful from a design standpoint to assume larger radii. The mesh consists of eight-noded C3D8I brick elements, with a small number of triangular prism elements C3D6 used to model part of the noodle region as shown in the cross sections of Figures 13 and 14. Surfaces **TBOTN**, **FOOTFR**, **WEBFR**, **WEBRE**, and **WEBTOP** as shown in Figure 13a were defined to facilitate the connection of the T-stiffener models to the global shell model and the panel skin/delamination model discussed above [35].

### 3.4.3 Combining Sections to Create Local 3D Models of T-Stiffener, Panel Skin and Interface

The models discussed in sections 3.4.1 and 3.4.2 were combined for a local 3D representation of the panel skin, the delaminated interface, the stiffener foot and web including the transition region with detailed modeling of the radius and the noodle as shown in Figure 15 for delamination length  $a=81.9$  mm. Shell elements had been removed from the global shell model as discussed earlier, and the model of the panel skin and delaminated interface was placed as shown in Figure 15a. The T-stiffener model mesh was placed to complete the local 3D model as shown in Figure 15b. The solid models were joined using the \*TIE option in ABAQUS® and connected to the global shell model using the solid-to-shell coupling technique ABAQUS® [35].

### 3.5 Finite Model Assembly, Load and Boundary Conditions

An example of an assembled model is shown in Figure 16. For modeling the experiment, which was performed under displacement control, uniform displacements  $u$ ,  $v$  were applied at one corner node to introduce shear as shown in Figure 16a. The in-plane displacements  $u$ ,  $v$  were suppressed at the diagonally opposite corner and the out-of-plane displacements  $w$  were suppressed along all four edges across the entire width of the inner and outer steel load frame. The section around the stiffener termination, modeled with solid elements, is shown in the detail of Figure 16b for the local 3D model discussed in section 3.4 with a model length  $c=50.2$  mm and a transition radius  $r=0.711$  mm. Two local 3D models where only the panel skin and stiffener foot were modeled with solid elements (as discussed in section 3.2) are shown in Figures 17a and b for model lengths  $c=113.1$  mm and  $c=38.1$  mm, respectively.

For all models, geometrically non-linear analyses were performed using ABAQUS® Standard to account for the inherently unstable nature of the buckling problem [35]. The displacements  $u$ ,  $v$  at the corner node were applied in a single analysis step. Note, the

introduction of geometrical imperfections, including the delamination modeled in the current analyses, were not required to initiate buckling.

### 3.6 Analysis Overview

A total of 41 different model combinations were analyzed. An overview of all models generated is given in Tables 2 and 3. The following cases were studied in detail:

- Three different options in ABAQUS<sup>®</sup> for modeling the contact in the plane of delamination were studied as discussed in section 3.2.1
- The effect of introducing and modeling a resin layer at the delaminated interface was studied as discussed in section 3.2.2
- Mesh refinement studies across the width of the stiffener foot were performed using models of different length  $c$  shown in Figure 17. Uniform meshes with 30, 40, 50 and 60 elements across the width of the stiffener were used in the study as shown in Figures 18b to e. In order to capture the local failure near the edges, a model with a locally refined fine mesh was chosen as shown in Figure 18a. In order to capture the local failure index distribution in the vicinity of the web termination, a model with a fine mesh in the center was chosen as shown in Figure 18e.
- Mesh refinement studies across the width of the stiffener foot were performed using models which included a 3D representation of the web as shown in Figure 19
- Mesh refinement studies across the width of the stiffener foot were performed using models which included a 3D representation of the web, the noodle and two transition radii ( $r=0.711$  mm and  $r=2.54$  mm) as shown in Figure 20
- Two additional transition radii ( $r=0.254$  mm and  $r=5.08$  mm) were studied using models with a refined center and a refined mesh as discussed in section 3.4
- The effect of varying the material properties in the noodle region was also studied for two transition radii ( $r=0.711$  mm and  $r=2.54$  mm). In one analysis it was assumed that the entire noodle region was filled with resin. Another analysis was performed based on the assumption that the noodle was filled with unidirectional tape material, where the fibers were aligned along the stiffener in the global  $z$ -direction. It is believed that the assumptions capture the lower and upper bounds for realistic material properties in the noodle. The material properties are given in Table 1.

## 4. ANALYSIS RESULTS

### 4.1 Model Deformation

#### 4.1.1 Global Deformation

Under the applied shear loading, the analysis predicts the buckling deformation shown in Figure 21. For the simulated delamination length ( $a=81.9$  mm), three peaks and one trough can be observed in the panel bays adjacent to the center stiffener as shown in Figure 21a. The color contour plots in Figure 21b illustrate the out-of-plane deformation  $w$ . The color limits range from dark blue for a negative displacement (trough) to bright red for a positive displacement (peak). More details may be found in a previous study [12].

#### 4.1.2 Local Deformations

Details of the deformed finite element models are shown in Figures 22 to 24 after the entire external displacement  $u=v=6.35$  mm had been applied in all cases. Mode I opening was observed across the entire width of the stiffener over the entire delaminated length. The deformed stiffener terminations for local 3D models where the entire length of the delamination ( $a=81.9$  mm) was included in the local 3D solid model ( $c=113.7$  mm) are shown in Figure 22. The original model with a fine mesh near the edges and a coarser mesh in the center is shown in Figure 22a [12]. The other meshes used in the mesh refinement study are shown in Figures 22b to f.

The local deformations of the center stiffener near the termination are shown in Figure 23 for local 3D models where only a small section in front and behind the delamination front were included in the local 3D solid model ( $c=38.1$  mm).

The deformed stiffener termination for local models where the stiffener web was included in the local 3D solid model is shown in Figure 24a for a fine mesh in the center. Another set of models included the transition radius between web and foot as well as the detailed noodle region in the local solid model. The deformed models for two different transition radii (0.711 mm and 2.54 mm) between stiffener foot and web are shown in Figures 24b and c.

#### 4.2 Calculation of Mixed-Mode Strain Energy Release Rates and Failure Indices

For each nodal point along the delamination front, the critical energy release rate,  $G_c$ , was calculated from a mixed mode failure criterion (Figure 3) for the computed mixed-mode ratio,  $G_S/G_T$ . Subsequently, the failure index  $G_T/G_c$  was calculated for the final load increment and plotted versus the location  $s$  across the width of the stiffener,  $b$ , where

$$s(y) = \frac{y - y_0}{b}; \quad 0.0 \leq s \leq 1.0.$$

At the left edge of the stiffener, the nodal point coordinates are equal to  $y=y_0$  which yields  $s=0.0$ , and the right edge nodal point coordinates are equal to  $y=y_b$  which results in  $s=1.0$  as depicted in Figures 16b and 17.

##### 4.2.1 Failure Indices Computed from Local Solid Models of Panel Skin and Stiffener Foot

###### 4.2.1.1 Failure indices computed for different contact options

The set of models where only the panel skin and stiffener foot were part of the local 3D model were studied first. The computed failure index distributions across the width of the stiffener are plotted in Figure 25 for the model shown in Figure 21a. The delamination is modeled at the interface between the stiffener foot and the panel as shown in Figure 8. The distributions were obtained from the analyses where contact was modeled using either the finite sliding option, the small sliding option or gap elements in ABAQUS®. The failure index peaked at the edges ( $s=0.0$  and  $s=1.0$ ) with an additional peak around the center ( $s \sim 0.5$ ) underneath the stiffener. The results were in excellent agreement and showed that the failure index was nearly insensitive to the contact algorithms used in these analyses.

#### 4.2.1.2 Failure indices computed for models including a resin layer

The effect of including a resin rich layer on the computed failure indices was studied. The  $G_T/G_c$  distributions obtained from the analysis without the resin layer (Figure 8), with the resin layer (type  $L1$ , Figure 9a), and with the resin layer (type  $L2$ , Figure 9b), are plotted in Figure 26. The results were in good agreement and showed that the failure index was nearly insensitive to the introduction of the resin layer into the model. Based on the comparison, local models without the resin layer were used for all studies where only the panel skin and stiffener foot were part of the local 3D model.

#### 4.2.1.3 Mesh refinement study for local 3D models of different length $c$

The results of a mesh refinement study are plotted in Figures 27 to 29. The computed failure index distributions across the width of the stiffener are plotted in Figure 27 for the case where the entire delaminated section was included in the local 3D solid model ( $c=113.7$  mm) as shown in Figure 22. Fine meshes were able to give a better representation of the distribution near the edges and the center where local peaks in the failure index distribution were observed. Overall, the results were in excellent agreement and showed that the computed failure index did not depend on the mesh size across the width.

The computed failure index distributions across the width of the stiffener are plotted in Figure 28 for the case where only a small section in front and behind the delamination front was included in the local 3D solid model ( $c=38.1$  mm) as shown in Figure 23. As above, fine meshes were able to give a better representation of the distribution near the edges and the center where local peaks in the failure index distribution were observed.

A comparison of distributions obtained from the models is shown in Figure 29 where the results from the model with the refined edges (Figure 18a) and refined center (Figure 18e) were combined. The results were in excellent agreement and confirmed that the entire delamination does not have to be included in the local solid model. The results reconfirm the findings published in reference [13].

#### 4.2.2 Failure Indices Computed from Local 3D Models Which Included the Web

The computed failure index distributions across the width of the stiffener are plotted in Figure 30 for a set of models that include the web in the local 3D model as shown in Figures 19 and 24a. As before, the failure index peaked at the edges ( $s=0.0$  and  $s=1.0$ ) with an additional peak around the center ( $s\approx 0.5$ ) underneath the web of the stiffener. Fine meshes were able to give a better representation of the distribution near the edges and the center, where local peaks in the failure index distribution were observed. Overall the results were in excellent agreement and showed that the computed failure index did not depend on the mesh size across the width. Results were compared to failure index distributions obtained from other models. The findings are discussed in a later section.

#### 4.2.3 Failure Indices Computed from Local Solid Models Which Include the Web, Noodle and Different Transition Radii

For local 3D solid models which included the web, the noodle region and the web/flange transition radius (shown in Figure 20), the calculated failure indices are shown in Figures 31 through 36. Failure indices were calculated for different transition radii  $r=0.711$  mm,  $r=2.54$  mm,  $r=5.08$  mm and  $r=0.254$  mm. For transition radii  $r=0.711$  mm and  $r=2.54$  mm, the effect of assigning different material data to the noodle region was also studied. For all cases, the



failure index peaked at the edges ( $s=0.0$  and  $s=1.0$ ) with an additional peak around the center ( $s\approx 0.5$ ) underneath the stiffener web.

#### **4.2.3.1 Failure Indices Computed for Transition Radius $r=0.711$ mm**

The computed failure index distributions across the width of the stiffener are plotted in Figures 31 and 32 for the models including a transition radius  $r=0.711$  mm as shown in Figure 24b. The results of a mesh refinement study are plotted in Figure 31 for the models where the noodle was represented as a unidirectional tape material (fibers aligned in the global  $x$ -direction). An additional small plateau was observed for  $0.47 < s < 0.49$  ( $G_T/G_c \approx 29$ ). Results obtained from an analysis where it was assumed that the entire noodle region was filled with resin are plotted in Figure 32. Included in the figure were the corresponding results from above for a model with 60 elements across the width of the stiffener foot with a refined center section. The results were in excellent agreement and demonstrated that little difference is seen when the noodle is modeled as a region filled with resin or a region filled with unidirectional tape. Results also show that the noodle region corresponds to changes in the trend of calculated energy release rate. As will be shown later, this effect becomes more prominent as the transition radius increases (see Figures 30 to 36).

#### **4.2.3.2 Failure Indices Computed for Transition Radius $r=2.54$ mm**

The results of a mesh refinement study are plotted in Figure 33 for the models including a transition radius  $r=2.54$  mm as shown in Figure 24c, where the noodle was represented as a unidirectional tape material (fibers aligned in the global  $x$ -direction). An additional local maximum was observed for  $0.44 < s < 0.46$  ( $G_T/G_c \approx 15$ ). Results obtained for a model with 60 elements across the width of the stiffener foot with a refined center section are plotted in Figure 34. Also included are results from an analysis where it was assumed that the entire noodle region was filled with resin. The results were in excellent agreement and confirmed that little difference is seen when the noodle is modeled as a region filled with resin or a region filled with unidirectional tape. Again, the results show that the trend in the failure index along the delamination front changes in the region of the noodle.

#### **4.2.3.3 Failure Indices Computed for Transition Radius $r=0.254$ mm**

The computed failure index distributions across the width of the stiffener are plotted in Figure 35 for two models including a transition radius  $r=0.254$  mm as shown in Figure 14a. Again, the results show that the trend in the failure index along the delamination front changes in the region of the noodle.

#### **4.2.3.4 Failure Indices Computed for Transition Radius $r=5.08$ mm**

The results obtained for two models including a transition radius  $r=5.08$  mm (as shown in Figure 14b) are plotted in Figure 36. An additional local maximum was observed for  $s \approx 0.4$  ( $G_T/G_c \approx 5$ ). Results obtained for a model with 60 elements across the width of the stiffener foot with the refined center section are plotted in Figure 36 together with results from an analysis where it was assumed that the entire noodle region was filled with resin. The results were in excellent agreement and confirmed that little difference is seen when the noodle is modeled as a region filled with resin or a region filled with unidirectional tape. Results for all radii were compared to failure index distributions obtained from other models. The findings are discussed in the following section.

#### 4.2.4 Comparison of Failure Indices Computed from Different Local 3D Models

The computed failure index distributions across the width of the stiffener obtained from different models were plotted in Figures 37 to 43 for comparison with reference results. The failure indices obtained for the case where only a small section in front and behind the delamination front was included in the local 3D solid model ( $c=38.1$  mm) were selected as reference results. The combined results from the models with refined edges and center (Figures 23a and f) were used as reference results in all the figures. For all cases, the failure index peaked at the edges ( $s=0.0$  and  $s=1.0$ ) with an additional peak around the center ( $s\approx 0.5$ ) underneath the stiffener web.

First, the results obtained from a model that included the panel skin, stiffener foot and the web in the local solid model as shown in Figures 24a were plotted in Figure 37 for comparison with the reference result. Qualitatively, both distributions followed the same trend. In two areas to the left and right of the web ( $0.0 \leq s \leq 0.4$  and  $0.7 \leq s \leq 1.0$ ), the results are in good agreement. Locally, near the web ( $0.4 \leq s \leq 0.7$ ) the distributions differ. The peak values computed for the local solid model that included the web exceed the reference values by about 49%. The peak location is also offset. To find an explanation, the mode I, mode II and mode III components were compared as will be discussed later.

The results obtained for a transition radius  $r=0.711$  mm (as shown in Figure 24b) are plotted in Figure 38. In the area to the left of the web ( $0.0 \leq s \leq 0.4$ ), the results are in good agreement. In the areas to the right of the web ( $0.7 \leq s \leq 1.0$ ), the results are higher for the models which included the web and the noodle. An additional small plateau was observed for  $0.47 < s < 0.49$  ( $G_T/G_c \approx 29$ ) which was not observed in the results used as reference. Also the peak values computed for the local solid model that included the web and the noodle exceed the reference values by about 67%. As before the peak location is offset compared to the reference results.

For the results computed for the larger transition radius ( $r=2.54$  mm as shown in Figure 24), an additional local maximum was observed for  $0.44 < s < 0.46$  ( $G_T/G_c \approx 15$ ) as shown in Figure 39. In the areas to the right of the web ( $0.7 \leq s \leq 1.0$ ), the results are higher for the models which included the web and the noodle. Also the peak values computed for the local solid model that included the web and the noodle exceed the reference values by about 53%. For this transition radius, the peak location is almost identical to the peak observed for the reference results.

The results obtained for a smaller transition radius ( $r=0.254$  mm as shown in Figure 14a) are plotted in Figure 40. In two areas to the left and right of the web ( $0.0 \leq s \leq 0.4$  and  $0.7 \leq s \leq 1.0$ ), the results are in good agreement. Locally, near the web ( $0.4 \leq s \leq 0.7$ ) the distributions differ. The peak values computed for the local solid model that included the web exceed the reference values by about 52%. The peak location is also offset.

The results computed for a larger transition radius ( $r=5.08$  mm as shown in Figure 14b) are plotted in Figure 41. In the area to the left of the web ( $0.0 \leq s \leq 0.4$ ), the results are in good agreement. An additional local maximum was observed for  $s \approx 0.4$  ( $G_T/G_c \approx 5$ ) which was not observed in the results used as a reference. In the areas right of the web ( $0.7 \leq s \leq 1.0$ ), the results are higher for the models which included the web and the noodle. For this transition radius, the peak value is almost identical to the peak failure index computed for the reference results.

For closer comparison, the computed failure index distributions across the width of the stiffener are plotted in Figures 42 and 43 for all models discussed. In the area to the left of the web ( $0.0 \leq s \leq 0.4$ ), the failure index is low and all results are generally in good agreement. The peak values computed for the local solid models that included the web and the models that included the web and the noodle exceed the reference values which were obtained from models where the web had been modeled with shell elements. The location where the peak failure index was observed shifted from model to model. The results obtained from models where only the web was included in the local solid model were in excellent agreement with the failure indices computed from the model with the smallest radius ( $r=0.254$  mm) and, therefore the smallest noodle region (Figure 42). In two areas to the left and right of the web ( $0.0 \leq s \leq 0.4$  and  $0.7 \leq s \leq 1.0$ ), the results are in good agreement with the reference results. Locally, near the web ( $0.4 \leq s \leq 0.7$ ) the distributions differ up to 67% as discussed above. For models with larger radii ( $r=0.711$  mm,  $r=2.54$  mm and  $r=5.08$  mm), an additional local maxima or plateau was observed for  $0.4 < s < 0.5$  as shown in Figure 43. With increasing radius, the peak value decreases and shifts to the right of the center  $0.5 < s < 0.6$ . Also, in the area to the right of the web ( $0.7 \leq s \leq 1.0$ ), the results are lower for the models with larger transition radius. To find an explanation for the differences observed, the mode I, mode II and mode III components were compared and discussed below.

#### 4.2.5 Comparison of Energy Release Rate Components Computed from Different Local 3D Models

In order to find an explanation for the variations in failure index for the different models, the normalized mode I, mode II and mode III energy release rate distributions  $G_I/G_T$ ,  $G_{II}/G_T$  and  $G_{III}/G_T$  were plotted across the width of the stiffener as shown in Figures 44 to 48 for all models discussed. The normalized mode I energy release rate is near zero at the left edge ( $s = 0.0$ ) of the stiffener foot and increases towards the center ( $0.0 \leq s \leq 0.5$ ) where it reaches a peak as shown in Figures 44 and 45. In this section, the results from all models are in good agreement. Towards the right edge ( $0.5 \leq s \leq 1.0$ ), the normalized mode I energy release rate decreases. The results obtained from the models where only the web was modeled with solid elements follow the same trend as the results obtained from the model where the web was modeled with shell elements as shown in Figure 44. The results computed from the model with the smallest radius ( $r=0.254$  mm) also follow the same trend. The absolute  $G_I/G_T$  values differ, particularly near the edge ( $s \approx 1.0$ ). An additional local maximum and minimum were observed for models with larger radii ( $r=0.711$  mm,  $r=2.54$  mm and  $r=5.08$  mm) as shown in Figure 45. For larger radii, this local maximum/minimum is more pronounced. With increasing radius, and consequently larger noodle area, the peak value increases and shifts to the right of the center  $0.5 < s < 0.6$ . In the area to the right of the web ( $0.7 \leq s \leq 1.0$ ), the results are higher for models that include the web and noodle compared to the  $G_I/G_T$  values used as reference computed from the model where the web was modeled with shell elements. However, comparing only the results obtained from models that included the web and noodle, the values are lower for the models with larger transition radius.

The normalized mode II energy release rates are plotted in Figures 46 and 47. The mode II contribution is near zero at the left edge ( $s = 0.0$ ) of the stiffener foot, increases towards the center ( $0.0 \leq s \leq 0.3$ ), reaches a local maximum for  $s \approx 0.35$ , then decreases and reaches a local minimum near the center of the stiffener  $s \approx 0.55$  underneath the web. In this section, the results

from all models follow the same trend. However, the local maximum values obtained from the model where only the web was modeled with solid elements are about 14% lower than the reference results. The local maximum  $G_{II}/G_T$  values computed from the model with the smallest radius ( $r=0.254$  mm) are about 9% higher than the reference results as shown in Figure 46. Towards the right edge ( $0.5 \leq s \leq 1.0$ ), the normalized mode II energy release rate increases and reaches another local maximum for  $s \approx 0.65$  before it drops off towards the right edge then peaks again. An additional local maximum and minimum were observed for models with larger radii ( $r=0.711$  mm,  $r=2.54$  mm and  $r=5.08$  mm) for  $0.4 < s < 0.5$  as shown in Figure 47. A possible explanation is discussed below. For larger radii, this local maximum/minimum is more pronounced. However, absolute  $G_{II}/G_T$  values tend to be lower.

The normalized mode III energy release rates are plotted in Figures 48 and 49. The mode III contribution is near 1 at the left edge ( $s = 0.0$ ) of the stiffener foot, decreases towards the center ( $0.0 \leq s \leq 0.5$ ) and reaches zero for  $s \approx 0.50$  underneath the web. In this section, the results from all models follow the same trend. Towards the right edge ( $0.5 \leq s \leq 1.0$ ), the normalized mode III energy release rate increases and reaches a local maximum for  $s \approx 0.95$  before it drops off towards the right edge. The results obtained from the models where only the web was modeled with solid elements are higher and in good agreement with the results obtained from the model where the web was modeled with shell elements as shown in Figure 48. Both results were in good agreement with  $G_{III}/G_T$  values computed from the model with the smallest radius ( $r=0.254$  mm). Towards the right edge ( $0.6 \leq s \leq 1.0$ ), the normalized mode III energy release rate distribution computed for the model with the largest radius follows closely the distribution obtained from the model where the web was modeled with shell elements.

Differences in the energy release rate distributions were likely caused by a different local deformation behavior due to different local stiffnesses of the six different models. The local differences in stiffness were mainly caused by the local modeling of the noodle and the transition radius. The effect is most pronounced for the largest radius modeled ( $r=5.08$  mm) which corresponds to a large noodle cross section.

## 5. SUMMARY AND CONCLUDING REMARKS

The skin/stiffener separation of a graphite/epoxy composite panel reinforced with three stiffeners and subjected to shear loading was studied using computational fracture mechanics analysis. The shear loading causes the panel to buckle and the resulting out-of-plane deformation initiates skin/stiffener separation at the location of an embedded defect. The panel and surrounding load fixture were modeled with shell elements.

A small section of the stiffener foot, web and noodle as well as the panel skin in the vicinity of the delamination front were modeled with a local 3D solid model. The skin/stiffener interface was modeled as a separate layer of elements, which were given resin properties. The mixed-mode strain energy release rates were calculated along a straight delamination front across the width of the stiffener foot using the virtual crack closure technique. A failure index was calculated by correlating the results with a mixed-mode failure criterion of the graphite/epoxy material. Computed failure indices were compared to corresponding results where the entire web was modeled with shell elements and only a small section of the stiffener foot and panel was modeled locally with solid elements.

The results showed the following

- the failure index was insensitive to the contact algorithm used in the analysis.

- the computed failure index was insensitive to the introduction of the resin layer into the model.
- changing the mesh density across the width of the stiffener had a negligible effect on the results. However, local refinements were able to give a better representation of the distribution near the edges and the center where local peaks in the failure index distribution were observed.
- including the stiffener web in the local 3D model increased the computed failure index by about 49% compared to the reference results where the web was modeled with shells.
- including the web, the noodle and transition radius in the local 3D solid model increased the magnitude of the failure index up to 67% and changed the local distribution across the width.
- the magnitude of the failure index decreased with increasing transition radius.
- for all transition radii modeled, the material properties used for the noodle area had a negligible effect on the results.

Differences in the failure index distributions were likely caused by a different local deformation behavior due to different local stiffnesses of the models studied. The local differences in stiffness were mainly caused by the local modeling of the noodle and the transition radius. Based on the increase in computed failure index, it is suggested to use a high fidelity model including the noodle and transition radius whenever accurate analysis results are required. The results of this study are intended to be used as a guide for conducting finite element analyses of structures such as integrally stiffened panels. In particular, this guidance is aimed towards analyses that attempt to simulate delamination growth and debonding.

## **ACKNOWLEDGEMENTS.**

This research was partially supported by The Boeing Company and the Aviation Applied Technology Directorate under Technology Investment Agreement No. DAAH10-02-2-0001 as part of the Survivable, Affordable, Repairable, Airframe Program (SARAP).

This research was partially supported by the Aircraft Ageing and Durability Program as part of NASA's Aeronautics Program.

The analyses were performed at the Durability, Damage Tolerance and Reliability Branch at NASA Langley Research Center, Hampton, Virginia, USA.

## REFERENCES

- [1] I.S. Raju, R. Sistla, and T. Krishnamurthy, *Fracture Mechanics Analyses for Skin-Stiffener Debonding*, Engineering Fracture Mechanics, vol. 54, pp. 371-385, 1996.
- [2] E.H. Glaessgen, I.S. Raju, and C.C. Poe, *Fracture Mechanics Analysis of Stitched Stiffener-Skin Debonding*, in The 39th AIAA/ASME/ASCE/AHS/ASC Structures, Structural Dynamics and Materials Conference, Long Beach, California, AIAA 98-2022, April 20-23, 1998.
- [3] B.G. Falzon, G.A.O. Davies, and E. Greenhalgh, *Failure of Thick-Skinned Stiffener Runout Sections Loaded in Uniaxial Compression*, Composite Structures, vol. 53, pp. 223-233, 2001.
- [4] J.W.H. Yap, M.L. Scott, R.S. Thomson, and D. Hachenberg, *The Analysis of Skin-to-Stiffener Debonding in Composite Aerospace Structures*, Composite Structures, vol. 57, pp. 425-435, 2002.
- [5] P.J. Minguet, M.J. Fedro, T.K. O'Brien, R.H. Martin, and L.B. Ilcewicz, *Development of a Structural Test Simulating Pressure Pillowing Effects in Bonded Skin/Stringer/Frame Configuration*, in Proceedings of the Fourth NASA/DoD Advanced Composite Technology Conference, Salt Lake City, Utah, 1993.
- [6] P.J. Minguet and T.K. O'Brien, *Analysis of Composite Skin/Stringer Bond Failures Using a Strain Energy Release Rate Approach*, in The Tenth International Conference on Composite Materials, vol. I, A. Poursartip and K. Street, Eds., pp. 245-252, 1995.
- [7] P.J. Minguet and T.K. O'Brien, *Analysis of Test Methods for Characterizing Skin/Stringer Debonding Failures in Reinforced Composite Panels*, in Composite Materials: Testing and Design (Twelfth Volume), ASTM STP 1274, pp. 105-124, 1996.
- [8] P.J. Minguet, *Analysis of the Strength of the Interface Between Frame and Skin in a Bonded Composite Fuselage Panel*, in The 38th AIAA/ASME/ASCE/AHS/ASC Structures, Structural Dynamics and Materials Conference, pp. 2783-2790, 1997.
- [9] R. Krueger, M.K. Cvitkovich, T.K. O'Brien, and P.J. Minguet, *Testing and Analysis of Composite Skin/Stringer Debonding Under Multi-Axial Loading*, Journal of Composite Materials, vol. 34, pp. 1263-1300, 2000.
- [10] R. Krueger, I.L. Paris, T.K. O'Brien, and P.J. Minguet, *Fatigue Life Methodology for Bonded Composite Skin/Stringer Configurations*, Journal of Composites Technology and Research, vol. 24, pp. 56-79, 2002.
- [11] T.K. O'Brien, *Fracture Mechanics of Composite Delamination*, in ASM Handbook, Volume 21: Composites, ASM International, pp. 241-245, 2001.
- [12] R. Krueger and P.J. Minguet, *Skin-Stiffener Debond Prediction Based on Computational Fracture Analysis*, NIA Report No. 2005-06, NASA/CR-2005-213915, 2005.
- [13] R. Krueger and P.J. Minguet, *Analysis of Composite Panel-Stiffener Debonding Using a Shell/3D Modeling Technique*, NIA Report No. 2006-02, NASA/CR-2006-214299, 2006.
- [14] E.F. Rybicki and M.F. Kanninen, *A Finite Element Calculation of Stress Intensity Factors by a Modified Crack Closure Integral*, Engineering Fracture Mechanics, vol. 9, pp. 931-938, 1977.
- [15] R. Krueger, *Virtual Crack Closure Technique: History, Approach and Applications*, Applied Mechanics Reviews, vol. 57, pp. 109-143, 2004.
- [16] R.H. Martin, *Incorporating Interlaminar Fracture Mechanics Into Design*, in International Conference on Designing Cost-Effective Composites: IMechE Conference Transactions, London, U.K., pp. 83-92, 1998.
- [17] *ASTM D 5528-94a, Standard Test Method for Mode I Interlaminar Fracture Toughness of Unidirectional Fiber-Reinforced Polymer Matrix Composites*, in Annual Book of ASTM Standards, vol. 15.03: American Society for Testing and Materials, 2000.
- [18] *ASTM D 6671-01, Standard Test Method for Mixed Mode I-Mode II Interlaminar Fracture Toughness of Unidirectional Fiber Reinforced Polymer Matrix Composites*, in Annual Book of ASTM Standards, vol. 15.03: American Society for Testing and Materials, 2000.
- [19] R.H. Martin and B.D. Davidson, *Mode II Fracture Toughness Evaluation Using A Four Point Bend End Notched Flexure Test*, Plastics, Rubber and Composites, vol. 28, pp. 401-406, 1999.
- [20] M.L. Benzeggagh and M. Kenane, *Measurement of Mixed-Mode Delamination Fracture Toughness of Unidirectional Glass/Epoxy Composites with Mixed-Mode Bending Apparatus*, Composites Science and Technology, vol. 56, pp. 439-449, 1996.
- [21] I. Paris, P.J. Minguet, and T.K. O'Brien, *Comparison of Delamination Characterization for IM7/8552 Composite Woven and Tape Laminates*, in ASTM STP 1436, Composite Materials: Testing and Design Fourteenth Volume, 2003.
- [22] *KaleidaGraph: Data Analysis/Graphing Application for Macintosh and Windows Operating Systems*: Synergy Software, 1996.

- [23] R.H. Martin, *Evaluation of the Split Cantilever Beam for Mode III Delamination Testing*, in Composite Materials: Fatigue and Fracture (Third Volume), ASTM STP 1110, pp. 243-266, 1991.
- [24] S.M. Lee, *An Edge Crack Torsion Method for Mode III Delamination Fracture Testing*, Journal of Composite Technology and Research., pp. 193-201, 1993.
- [25] P. Robinson and D.Q. Song, *A New Mode III Delamination Test for Composites*, Advanced Composites Letters, vol. 1, pp. 160-164, 1992.
- [26] J. Li, S.M. Lee, E.W. Lee, and T.K. O'Brien, *Evaluation of the Edge Crack Torsion ECT Test for Mode III Interlaminar Fracture Toughness of Laminated Composites*, Journal of Composites Technology and Research, vol. 19, pp. 174-183, 1997.
- [27] J.G. Ratcliffe, *Characterization of the Edge Crack Torsion (ECT) Test for Mode III Fracture Toughness Measurement of Laminated Composites*, NASA/TM-2004-213269, 2004.
- [28] E.H. Glaessgen, W.T. Riddell, and I.S. Raju, *Effect of Shear Deformation and Continuity on Delamination Modeling with Plate Elements*, in The 39th AIAA/ASME/ASCE/AHS/ASC Structures, Structural Dynamics and Materials Conference, 1998.
- [29] E.H. Glaessgen, W.T. Riddell, and I.S. Raju, *Nodal Constraint, Shear Deformation and Continuity Effects Related to the Modeling of Debonding of Laminates, Using Plate Elements*, CMES, vol. 3, pp. 103-116, 2002.
- [30] J.T. Wang and I.S. Raju, *Strain Energy Release Rate Formulae for Skin-Stiffener Debond Modeled with Plate Elements*, Engineering Fracture Mechanics, vol. 54, pp. 211-228, 1996.
- [31] R. Krueger and T.K. O'Brien, *A Shell/3D Modeling Technique for the Analysis of Delaminated Composite Laminates*, NASA/TM-2000-210287, ARL-TR-2207, 2000.
- [32] R. Krueger and T.K. O'Brien, *A Shell/3D Modeling Technique for the Analysis of Delaminated Composite Laminates*, Composites Part A: Applied Science and Manufacturing, vol. 32, pp. 25-44, 2001.
- [33] R. Krueger and P.J. Minguet, *Analysis of Composite Skin-Stiffener Debond Specimens Using a Shell/3D Modeling Technique and Submodeling*, NIA Report No. 2004-04, NASA/CR-2004-212684, 2004.
- [34] R. Krueger and P.J. Minguet, *Analysis of Composite Skin-stiffener Debond Specimens Using Volume Elements and a Shell/3D Modeling Technique*, NASA/CR-2002-211947, ICASE Report No. 2002-38, 2002.
- [35] ABAQUS 6.6, *Analysis User's Manual*: ABAQUS, Inc., 2005.
- [36] P. Minguet, *Boeing SARAP Status Report - Durability (2nd Quarter 2002)*, 2002.
- [37] I.S. Raju, J.H. Crews, and M.A. Aminpour, *Convergence of Strain Energy Release Rate Components for Edge-Delaminated Composite Laminates*, Engineering Fracture Mechanics, vol. 30, pp. 383-396, 1988.
- [38] C.T. Sun and M.G. Manoharan, *Strain Energy Release Rates of an Interfacial Crack Between Two Orthotropic Solids*, Journal of Composite Materials, vol. 23, pp. 460--478, 1989.

Table 1.  
*Material Properties*

IM7/8552 Unidirectional Graphite/Epoxy Prepreg (nominal ply thickness $h=0.15$ mm)		
$E_{11} = 150$ GPa	$E_{22} = 10.7$ GPa	$E_{33} = 10.7$ GPa
$\nu_{12} = 0.33$	$\nu_{13} = 0.33$	$\nu_{23} = 0.45$
$G_{12} = 4.8$ GPa	$G_{13} = 4.8$ GPa	$G_{23} = 3.4$ GPa
IM7/8552 Graphite/Epoxy Plain Weave Fabric (nominal ply thickness $h=0.2$ mm)		
$E_{11} = 73$ GPa	$E_{22} = 73$ GPa	$E_{33} = 10.7$ GPa
$\nu_{12} = 0.04$	$\nu_{13} = 0.35$	$\nu_{23} = 0.35$
$G_{12} = 4.8$ GPa	$G_{13} = 4.1$ GPa	$G_{23} = 4.1$ GPa
8552 Resin		
$E = 4.7$ GPa	$\nu = 0.37$	(assumed isotropic)
Steel		
$E = 207$ GPa	$\nu = 0.33$	(assumed isotropic)

The material properties are given with reference to the ply coordinate axes where index 11 denotes the ply principal axis that coincides with the direction of maximum in-plane Young's modulus (fiber direction). Index 22 denotes the direction transverse to the fiber in the plane of the lamina, and index 33 is the direction perpendicular to the plane of the lamina.



Table 2.  
Finite Element Model Specification

Designation	<sup>+</sup> b <sub>1</sub> [mm]	<sup>+</sup> b <sub>2</sub> [mm]	<sup>+</sup> n	<sup>+</sup> n <sub>1</sub>	<sup>+</sup> n <sub>2</sub>	web	*noodle	radius [mm]	<sup>§</sup> resin	<sup>†</sup> contact
<i>Axxx</i>	<i>Local 3D model of panel skin and stiffener foot c= 113.7 mm (Figures 17a, 18, 22)</i>									
AF-8/10/8	5.08	35.56	-	8	10	shell	-	-	L0	F
AS-8/10/8	5.08	35.56	-	8	10	shell	-	-	L0	S
AG-8/10/8	5.08	35.56	-	8	10	shell	-	-	L0	G
AFL1-8/10/8	5.08	35.56	-	8	10	shell	-	-	L1	F
AFL2-8/10/8	5.08	35.56	-	8	10	shell	-	-	L2	F
AF-U30	-	-	30	-	-	shell	-	-	L0	F
AF-U40	-	-	40	-	-	shell	-	-	L0	F
AF-U50	-	-	50	-	-	shell	-	-	L0	F
AF-U60	-	-	60	-	-	shell	-	-	L0	F
AF-20/20/20	19.05	7.62	-	20	20	shell	-	-	L0	F
<i>Bxxx</i>	<i>Local 3D model of panel skin and stiffener foot c= 38.1 mm (Figures 17b, 18, 23)</i>									
BF-8/10/8	5.08	35.56	-	8	10	shell	-	-	L0	F
BF-U30	-	-	30	-	-	shell	-	-	L0	F
BF-U40	-	-	40	-	-	shell	-	-	L0	F
BF-U50	-	-	50	-	-	shell	-	-	L0	F
BF-U60	-	-	60	-	-	shell	-	-	L0	F
BF-20/20/20	19.05	7.62	-	20	20	shell	-	-	L0	F

Delamination length a= 81.9 mm and foot width b= 45.7 mm for all models as defined in Figures 16 and 17.

<sup>+</sup>Section widths b<sub>1</sub> and b<sub>2</sub> as defined in Figure 18. Number of elements n across the width b. Number of elements n<sub>1</sub> and n<sub>2</sub> in sections b<sub>1</sub> and b<sub>2</sub>.

\*Noodle material: C – unidirectional prepreg tape; R – matrix resin.

<sup>§</sup>Resin layer: Finite element models L1 and L2 as shown in Figure 9 and L3 in Figure 12.

<sup>†</sup>Contact: F – finite sliding, S – small sliding, G – gap elements as discussed in section 3.2.1

Table 3.  
Finite Element Model Specification

Designation	<sup>+</sup> b <sub>1</sub> [mm]	<sup>+</sup> b <sub>2</sub> [mm]	<sup>+</sup> n	<sup>+</sup> n <sub>1</sub>	<sup>+</sup> n <sub>2</sub>	web	*noodle	radius [mm]	<sup>§</sup> resin	<sup>†</sup> contact
<i>T<sub>xxx</sub></i>	<i>Local 3D model of the panel skin, stiffener foot and web c=50.17 mm (Figures 11, 19, 24a)</i>									
TFL1-8/10/8	5.08	35.56	-	8	10	3D	-	-	L1	F
TFL1-U30	-	-	30	-	-	3D	-	-	L1	F
TFL1-U40	-	-	40	-	-	3D	-	-	L1	F
TFL1-U50	-	-	50	-	-	3D	-	-	L1	F
TFL1-U60	-	-	60	-	-	3D	-	-	L1	F
TFL1-20/20/20	19.05	7.62	-	20	20	3D	-	-	L1	F
<i>TN<sub>xxx</sub></i>	<i>Local 3D model of the panel skin, stiffener foot and web including the noodle and transition radius c=50.17 mm (Figures 16, 20, 24b and c)</i>									
TN1L3C-8/10/8	5.08	35.56	-	8	10	3D	C	0.711	L3	F
TN1L3C-U30	-	-	30	-	-	3D	C	0.711	L3	F
TN1L3C-U40	-	-	40	-	-	3D	C	0.711	L3	F
TN1L3C-U50	-	-	50	-	-	3D	C	0.711	L3	F
TN1L3C-U60	-	-	60	-	-	3D	C	0.711	L3	F
TN1L3R-20/20/20	19.05	7.62	-	20	20	3D	R	0.711	L3	F
TN1L3C-20/20/20	19.05	7.62	-	20	20	3D	C	0.711	L3	F
TN2L3C-8/10/8	5.08	35.56	-	8	10	3D	C	2.54	L3	F
TN2L3C-U30	-	-	30	-	-	3D	C	2.54	L3	F
TN2L3C-U40	-	-	40	-	-	3D	C	2.54	L3	F
TN2L3C-U50	-	-	50	-	-	3D	C	2.54	L3	F
TN2L3C-U60	-	-	60	-	-	3D	C	2.54	L3	F
TN2L3R-20/20/20	19.05	7.62	-	20	20	3D	R	2.54	L3	F
TN2L3C-20/20/20	19.05	7.62	-	20	20	3D	C	2.54	L3	F
TN3L3C-8/10/8	5.08	35.56	-	8	10	3D	C	0.254	L3	F
TN3L3C-20/20/20	19.05	7.62	-	20	20	3D	C	0.254	L3	F
TN4L3C-8/10/8	5.08	35.56	-	8	10	3D	C	5.08	L3	F
TN4L3R-20/20/20	19.05	7.62	-	20	20	3D	R	5.08	L3	F
TN4L3C-20/20/20	19.05	7.62	-	20	20	3D	C	5.08	L3	F

Delamination length a= 81.9 mm and foot width b= 45.7 mm for all models as defined in Figures 16 and 17.

<sup>+</sup>Section widths b<sub>1</sub> and b<sub>2</sub> as defined in Figure 18. Number of elements n across the width b. Number of elements n<sub>1</sub> and n<sub>2</sub> in sections b<sub>1</sub> and b<sub>2</sub>.

\*Noodle material: C – unidirectional prepreg tape; R – matrix resin.

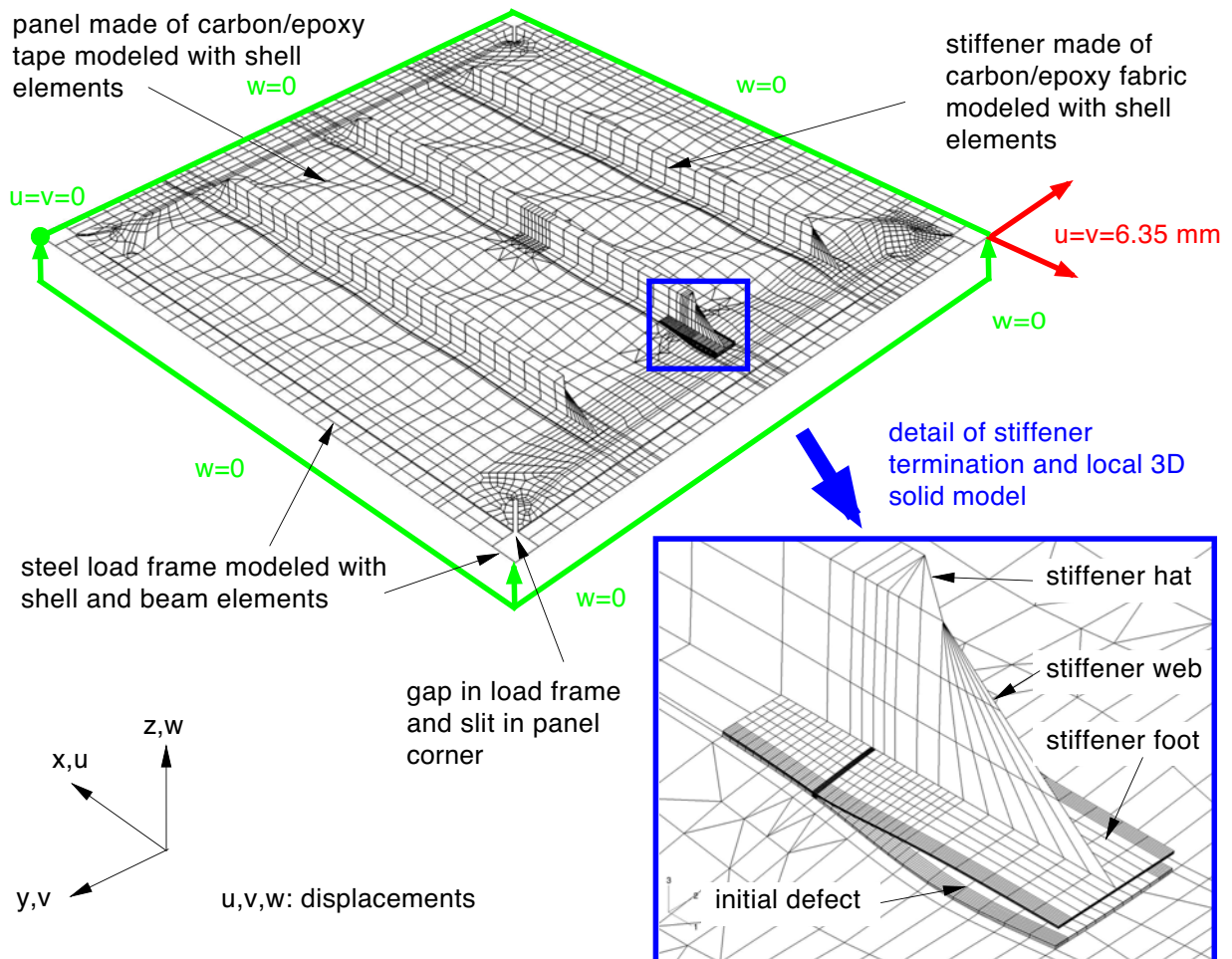
<sup>§</sup>Resin layer: Finite element models L1 and L2 as shown in Figure 9 and L3 in Figure 12.

<sup>†</sup>Contact: F – finite sliding, S – small sliding, G – gap elements as discussed in section 3.2.1



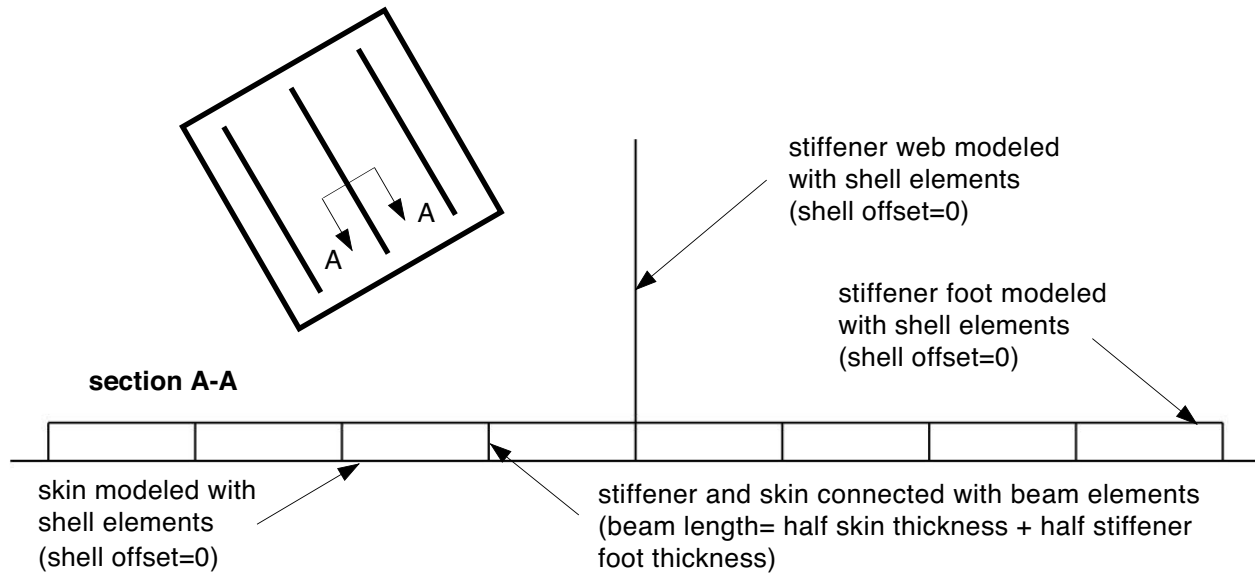
- initial defect at termination of center stiffener
- panel made of carbon/epoxy tape
- stiffener made of carbon/epoxy fabric
- gap in load frame and slit in panel corner
- inner steel load frame with attachment bolts
- outer steel load frame

a. Buckled composite panel under shear loading with picture frame.

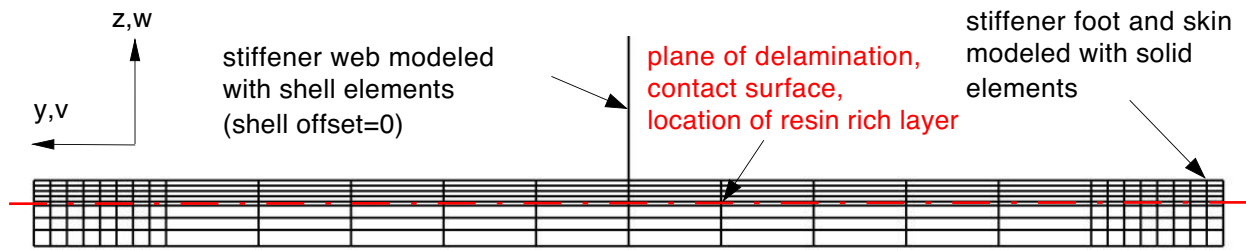


b. Finite Element model of stiffened panel and load frame.

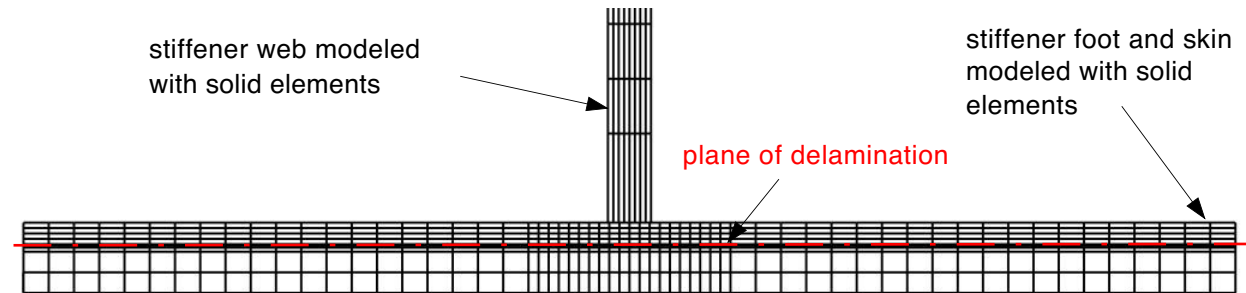
Figure 1. Stiffened composite panel (1016 mm x 1016 mm) [12,13].



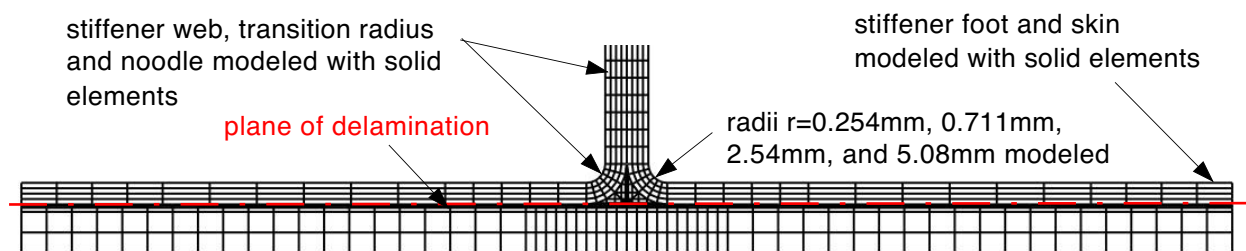
a. Shell model of skin/stiffener configuration.



b. Shell-3D model of skin/stiffener configuration [12,13 ].

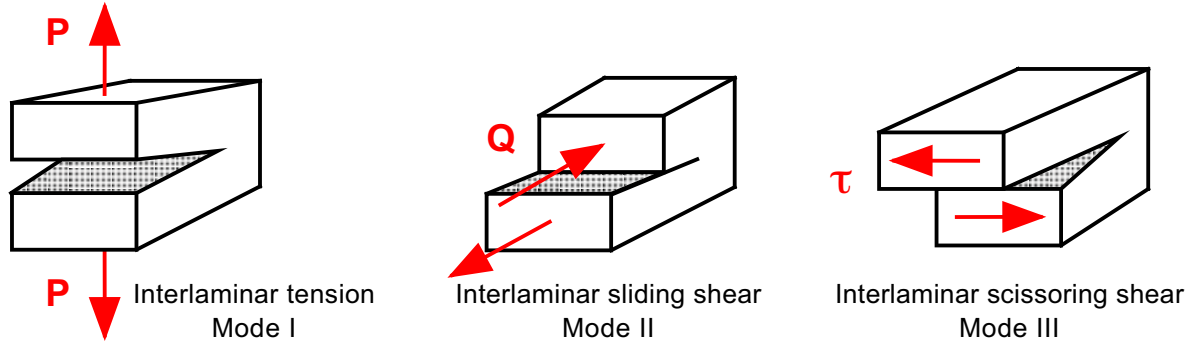


c. Solid model of skin/stiffener configuration.

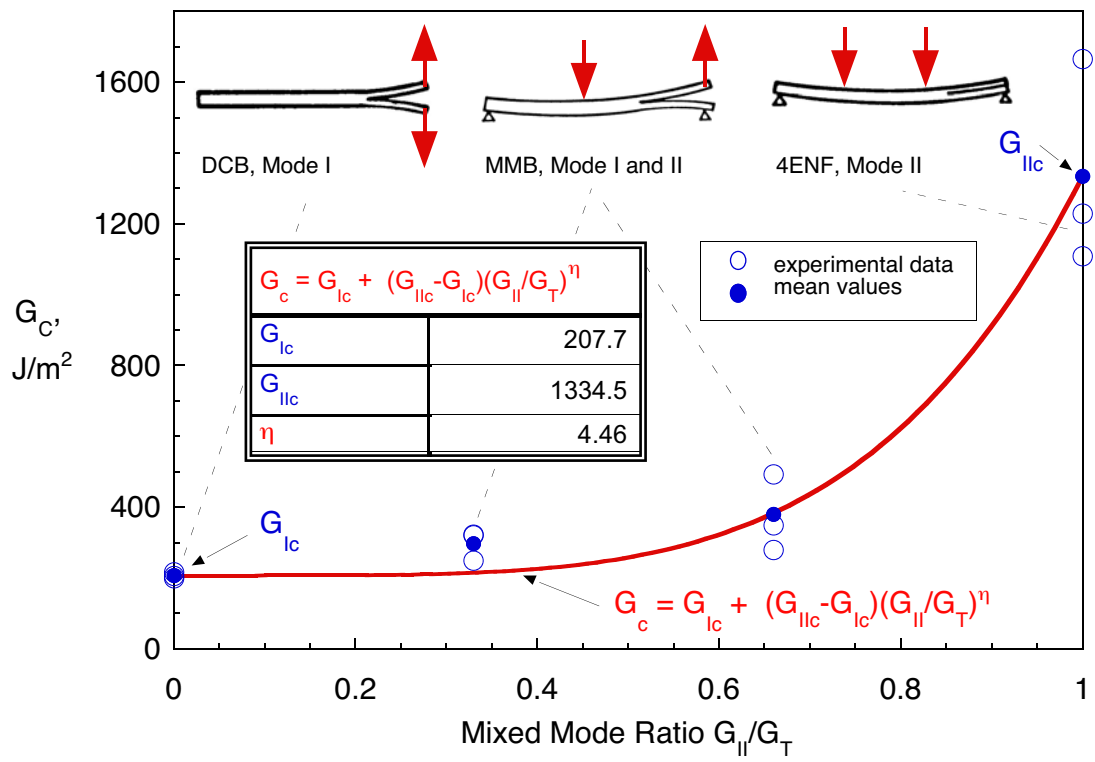


d. Solid model including transition radius and noodle area.

Figure 2. Modeling approaches for skin/stiffener panel.

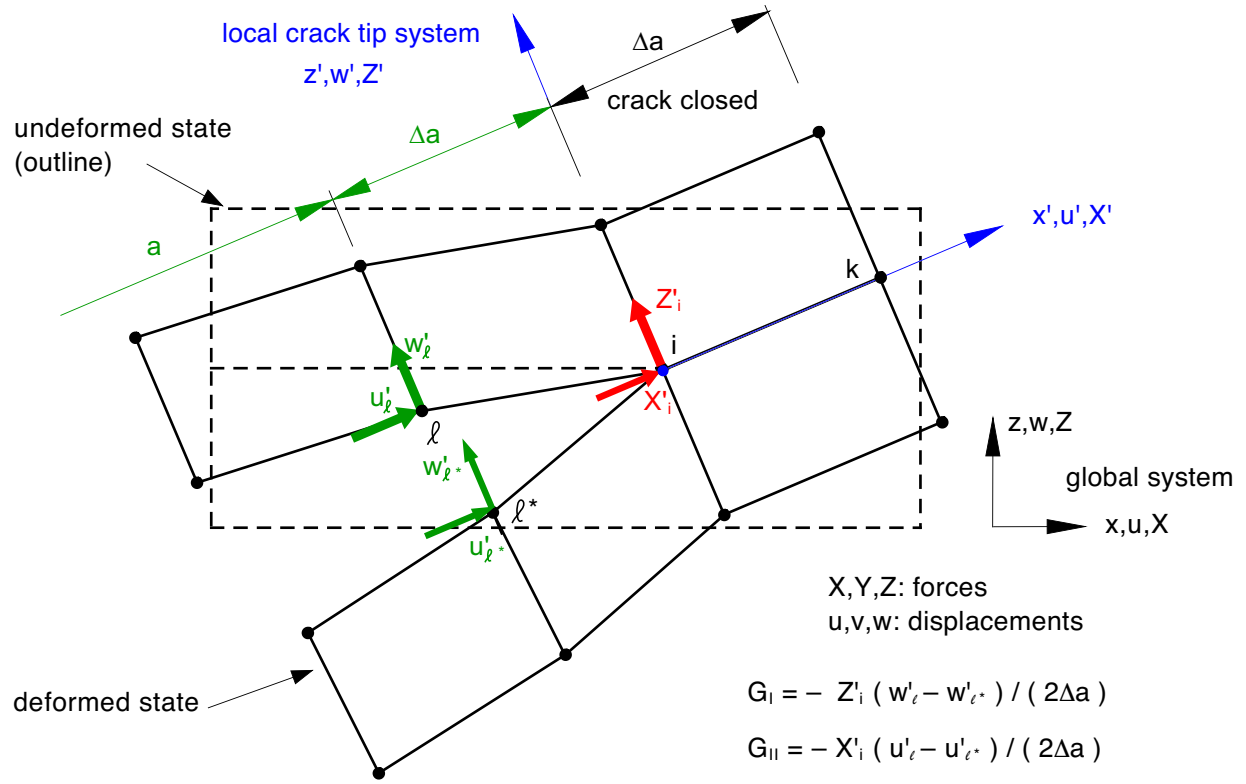


a. *Fracture Modes.*

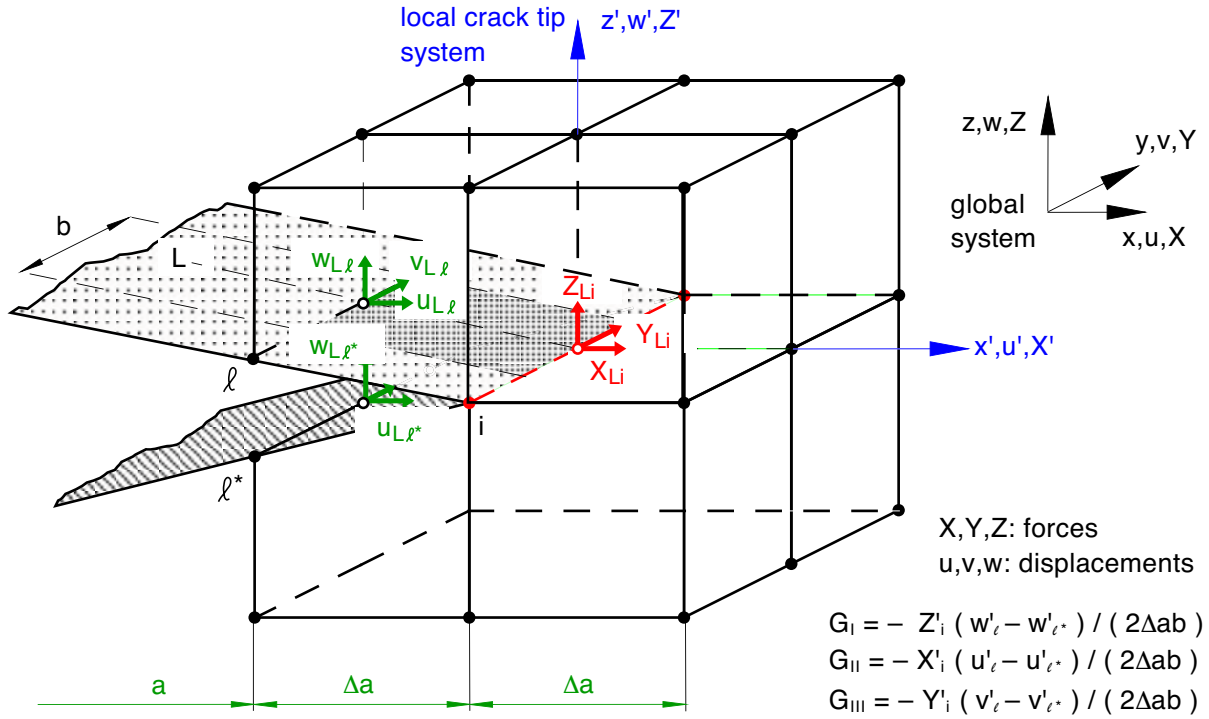


b. *Mixed-mode fracture criterion for IM7/8552.*

Figure 3. *Fracture mechanics approach.*



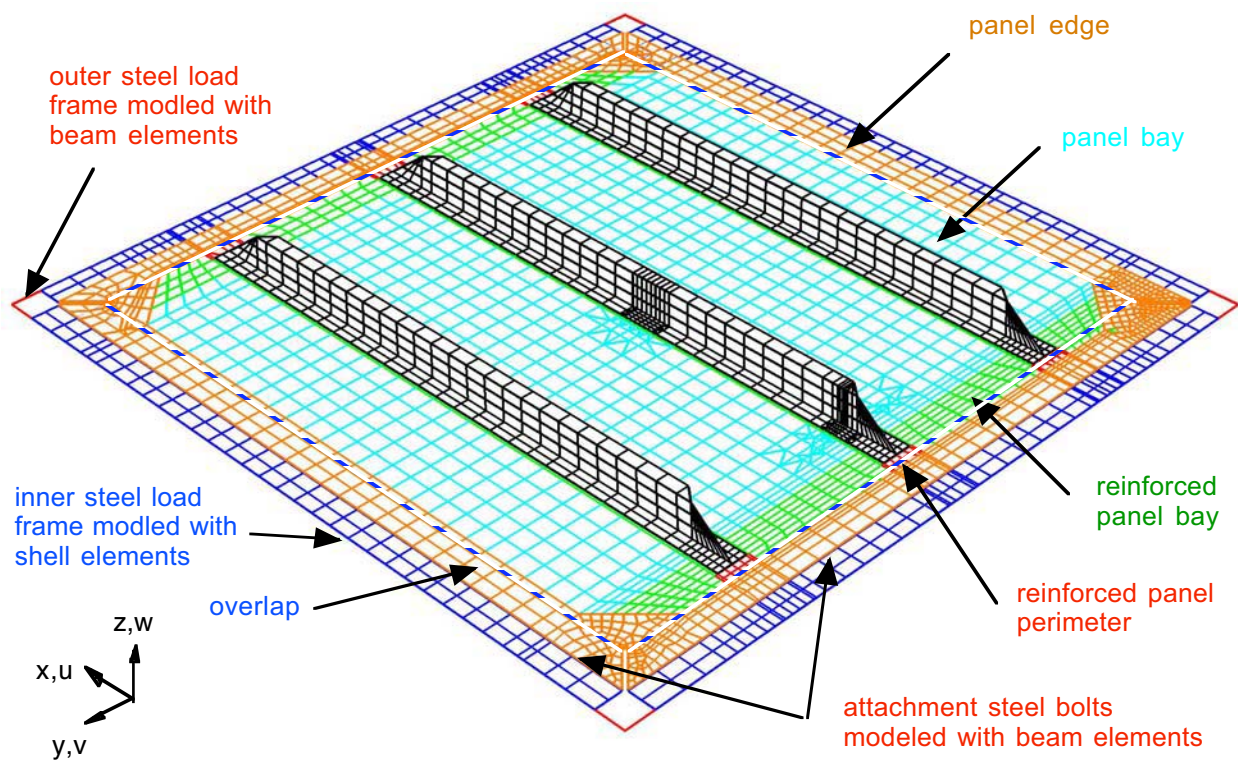
a. VCCT for geometrically nonlinear analysis.



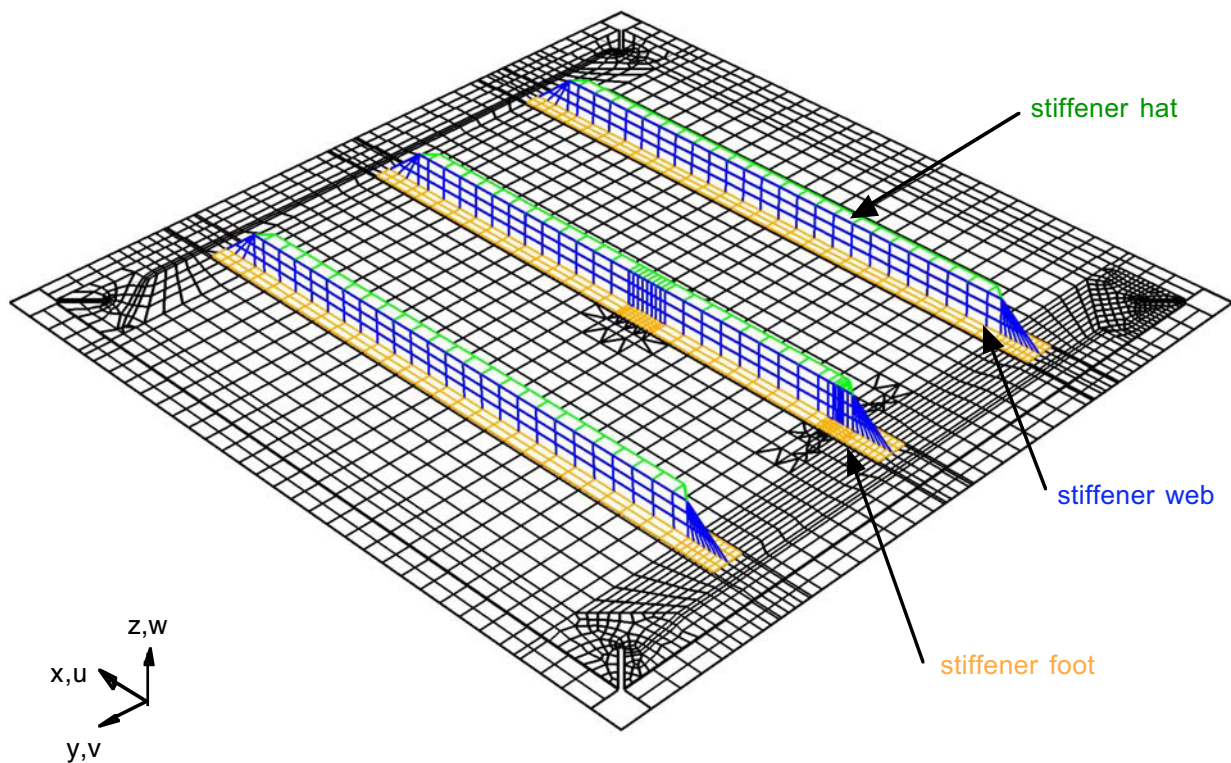
b. VCCT for eight noded solid elements.

Figure 4. Virtual Crack Closure Technique (VCCT).





a. Composite panel and load frame components.



b. Stiffener components.

Figure 5. Finite element model of stiffened composite panel and load frame.

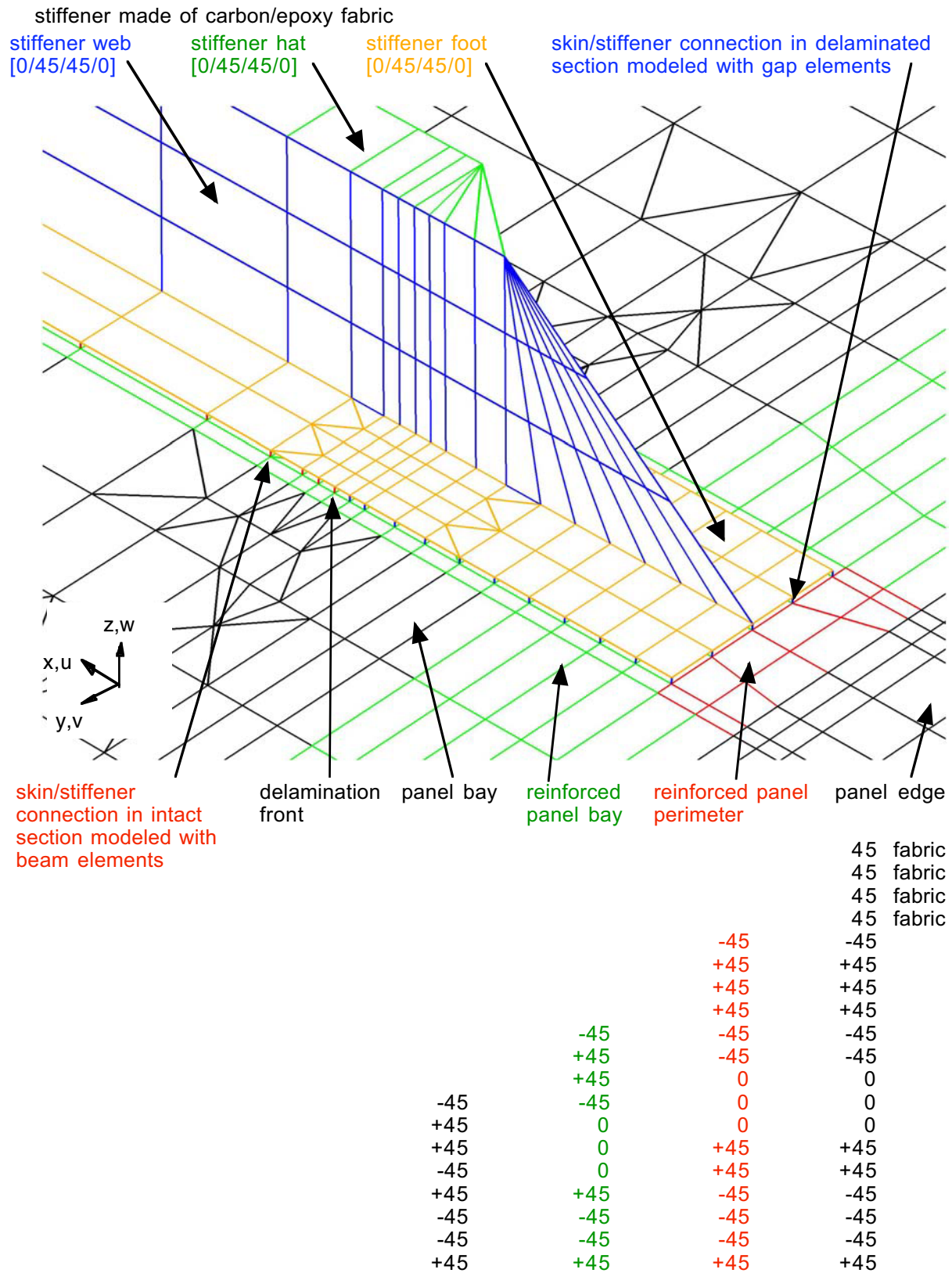
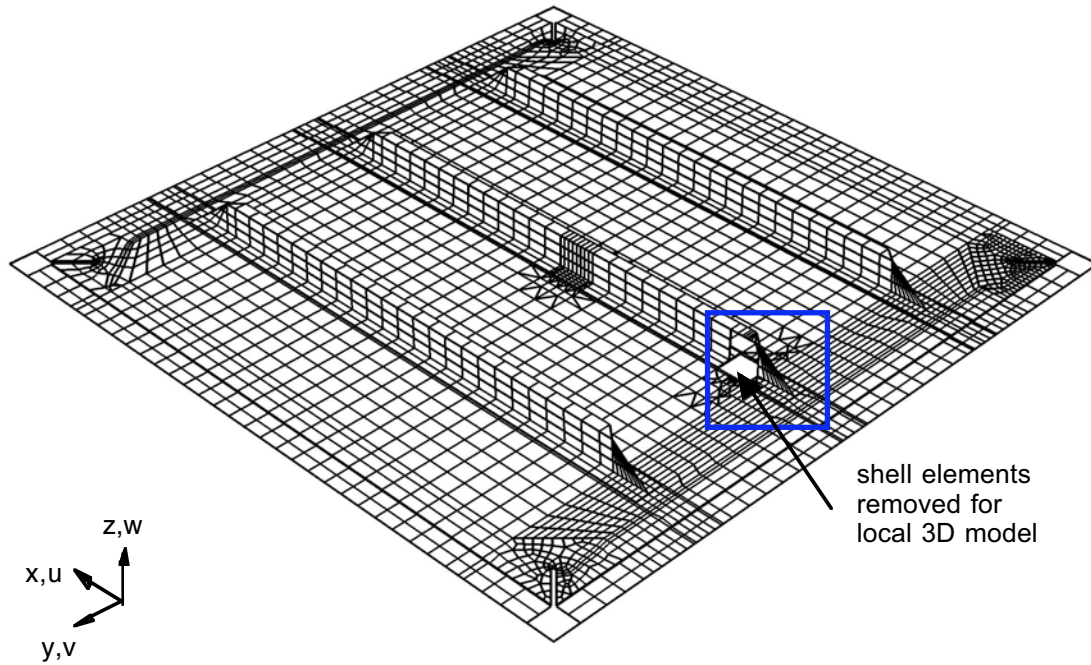
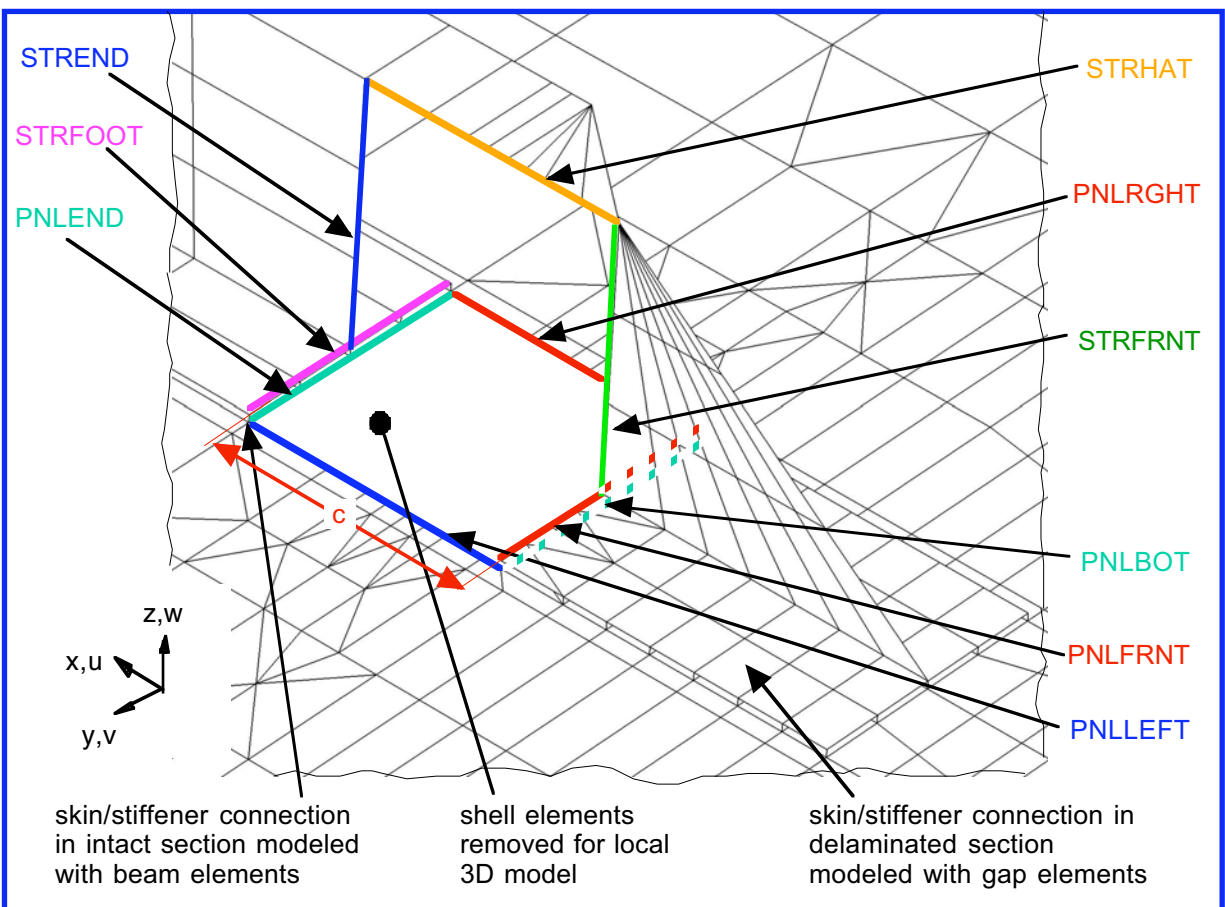


Figure 6. Detail of finite element model at stiffener termination.



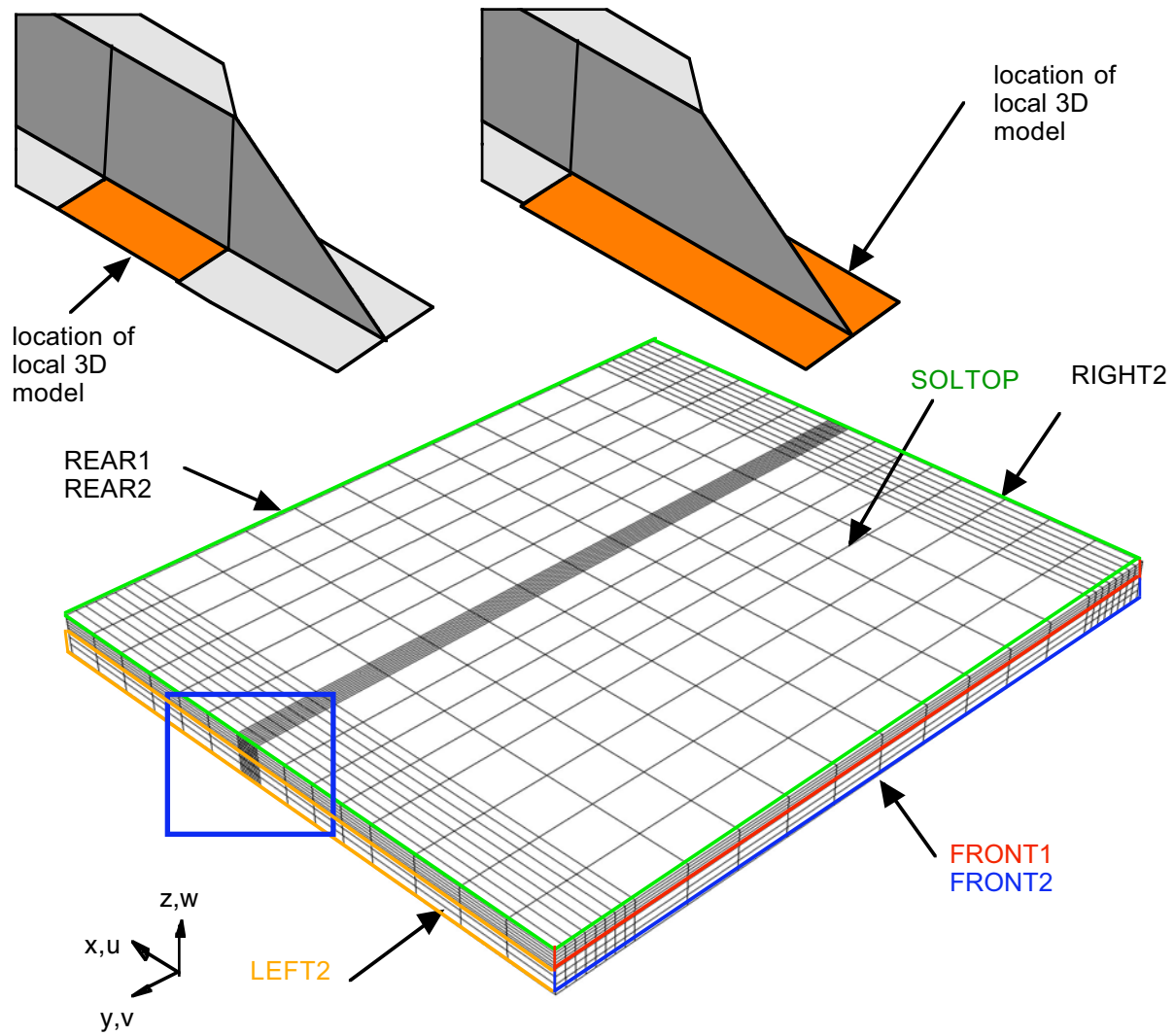


a. Composite panel and load frame components with removed shell elements.

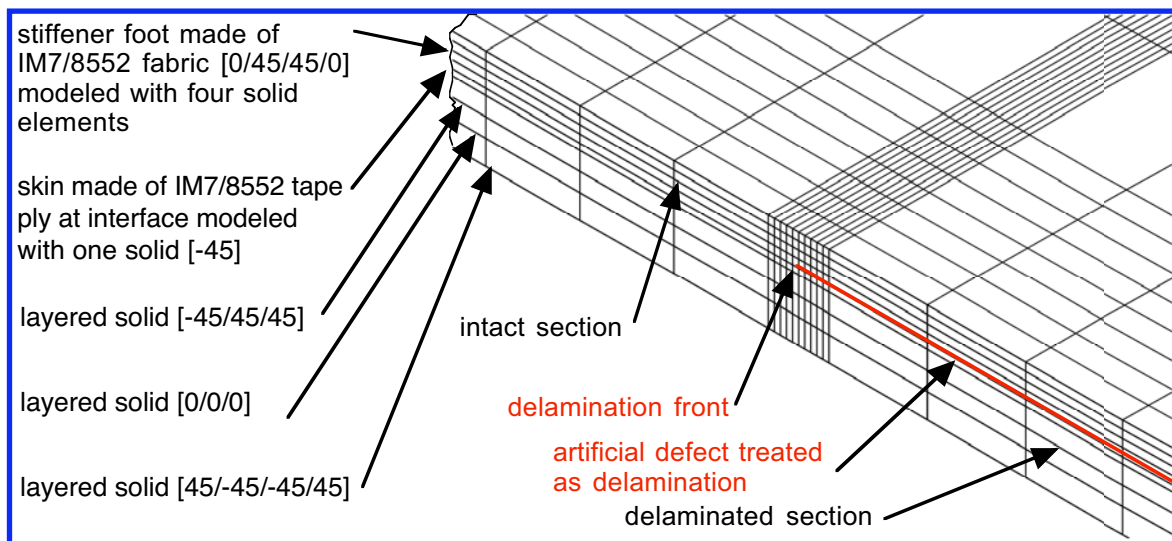


b. Detail of global shell model with edges for shell to solid coupling.

Figure 7. Global shell model of stiffened panel.

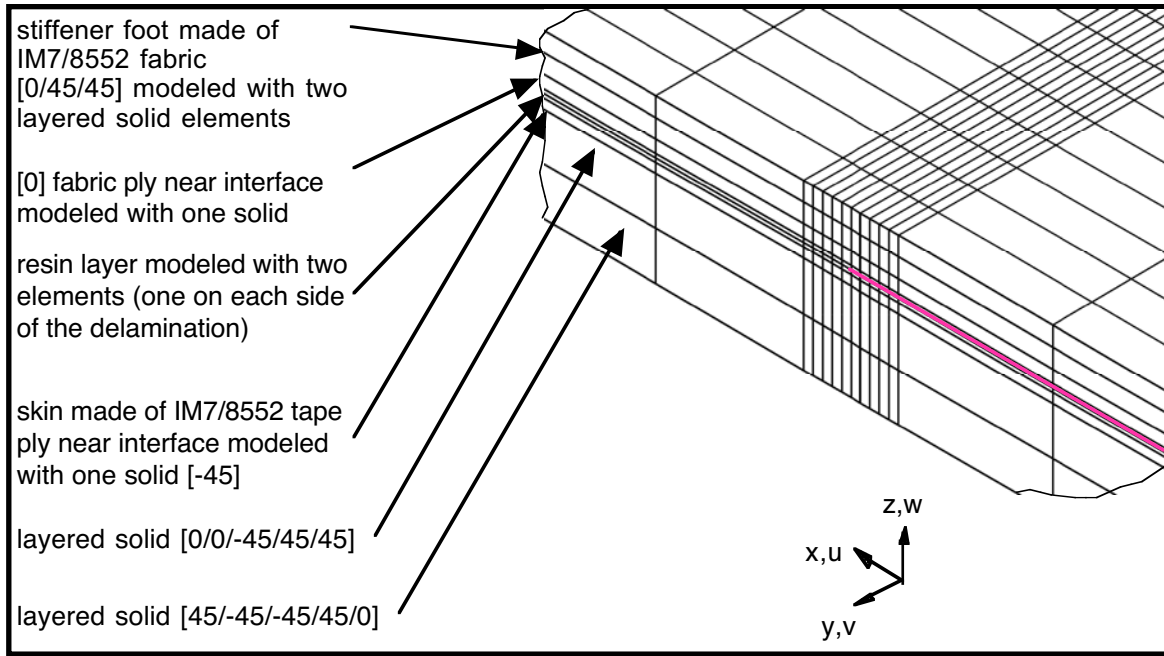


a. Local 3D model and surfaces for shell to solid coupling (L0).

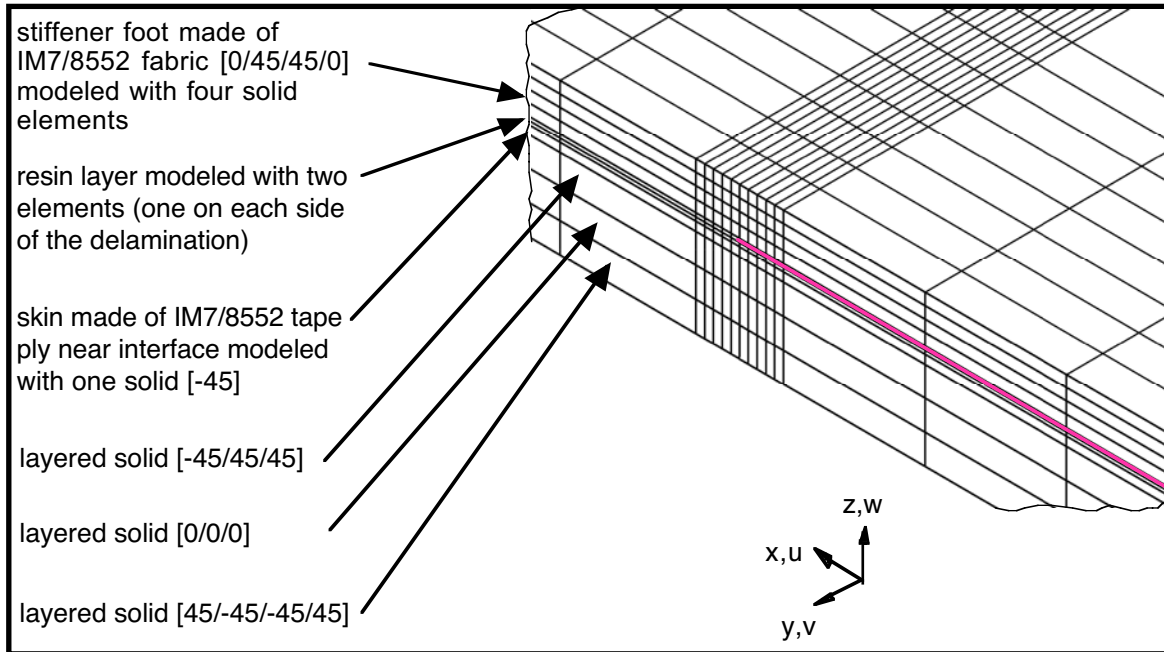


b. Detail of local 3D model around delamination front.

Figure 8. Local 3D model (L0).



a. Detail of modified local 3D skin/delamination model with resin layer (L1).



b. Detail of original local 3D skin/delamination model with resin layer (L2).

Figure 9. Local models with resin layer.

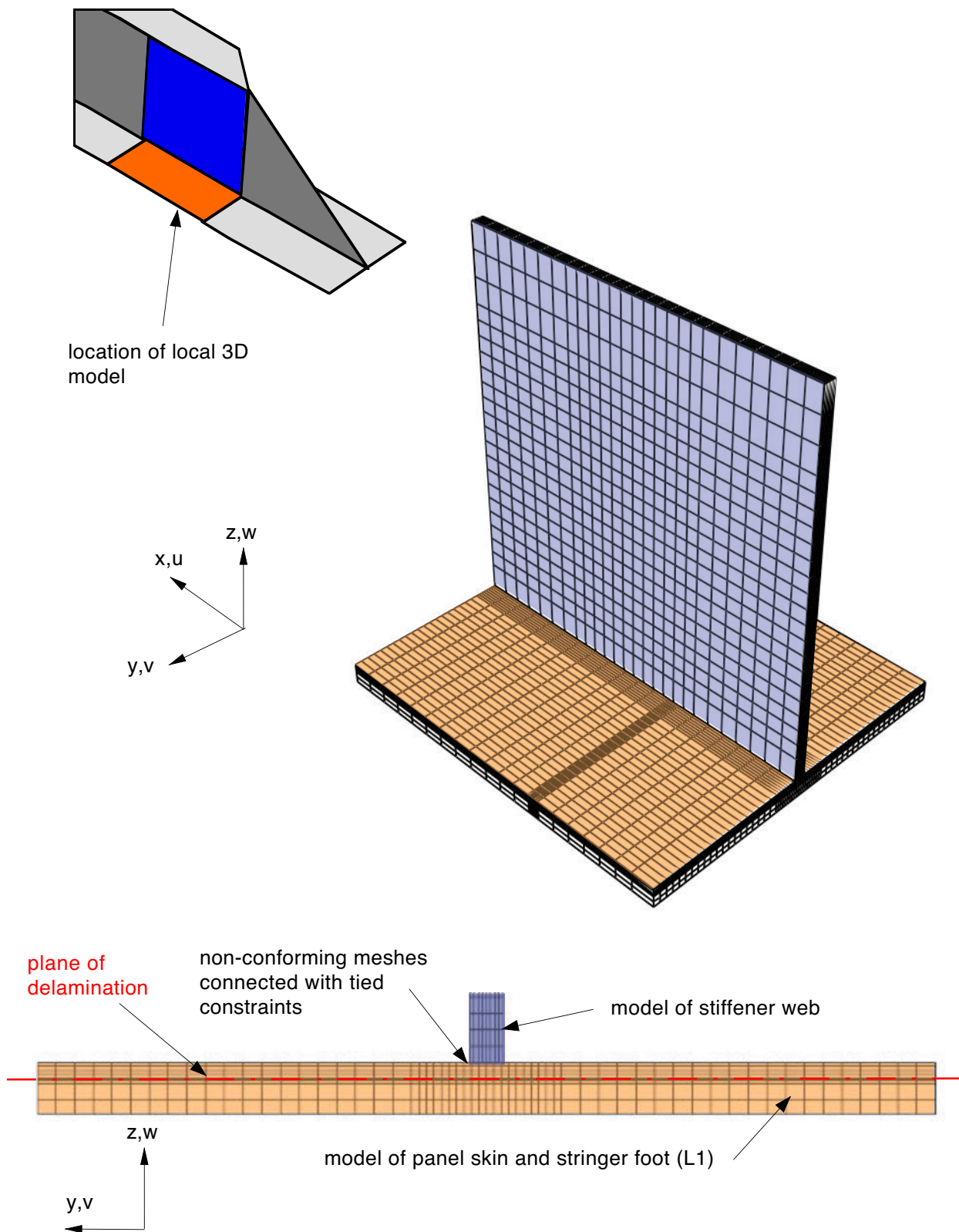
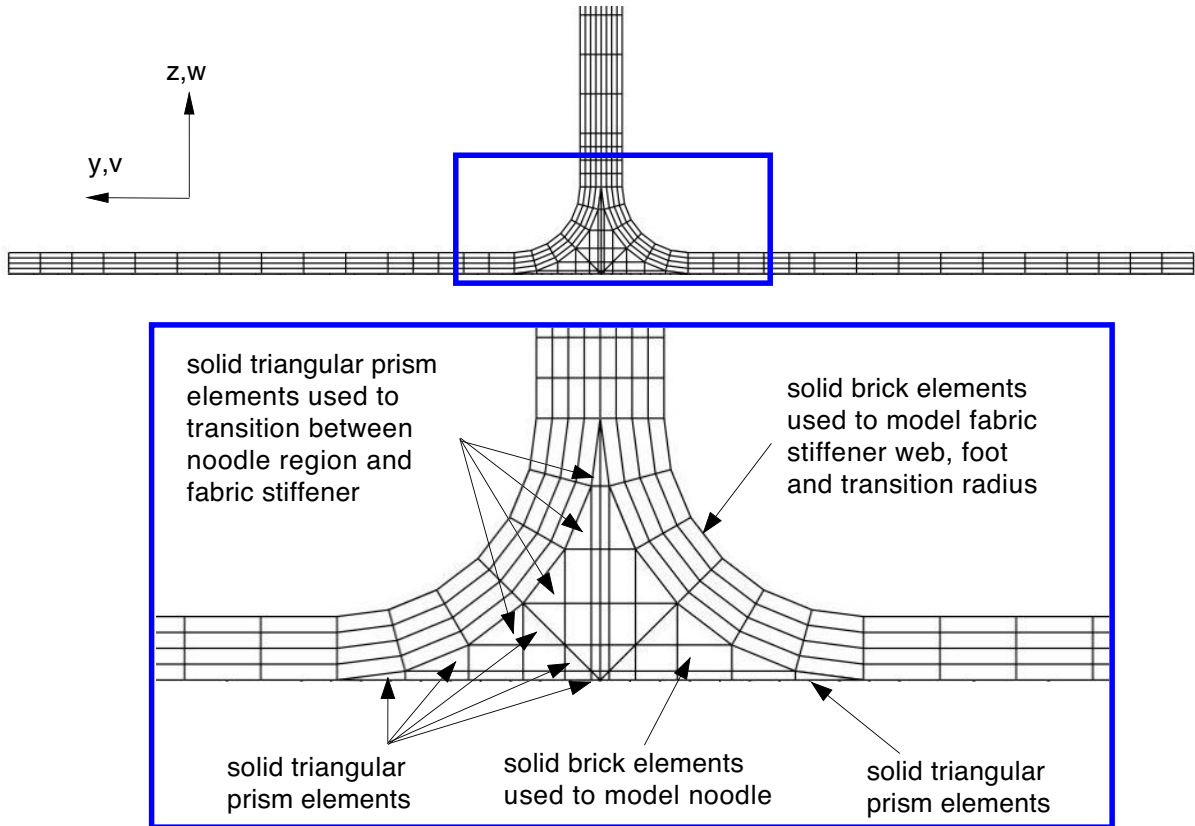
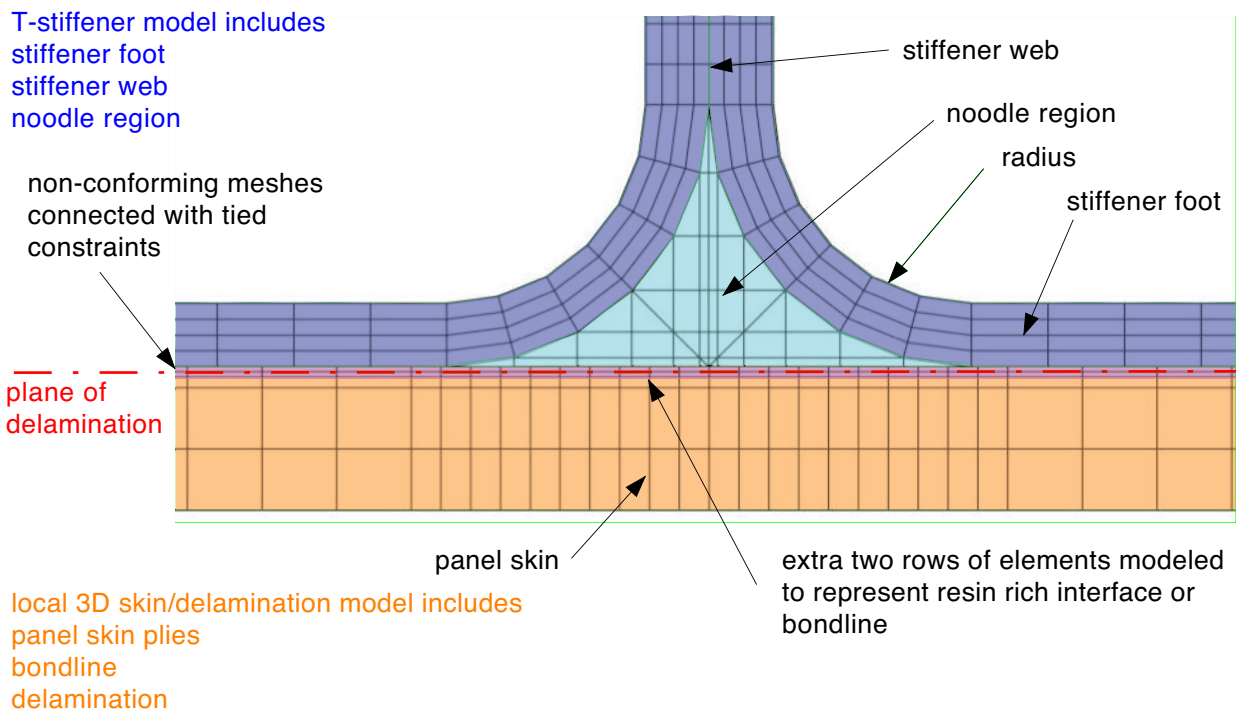


Figure 10. *Local 3D T-stiffener models.*



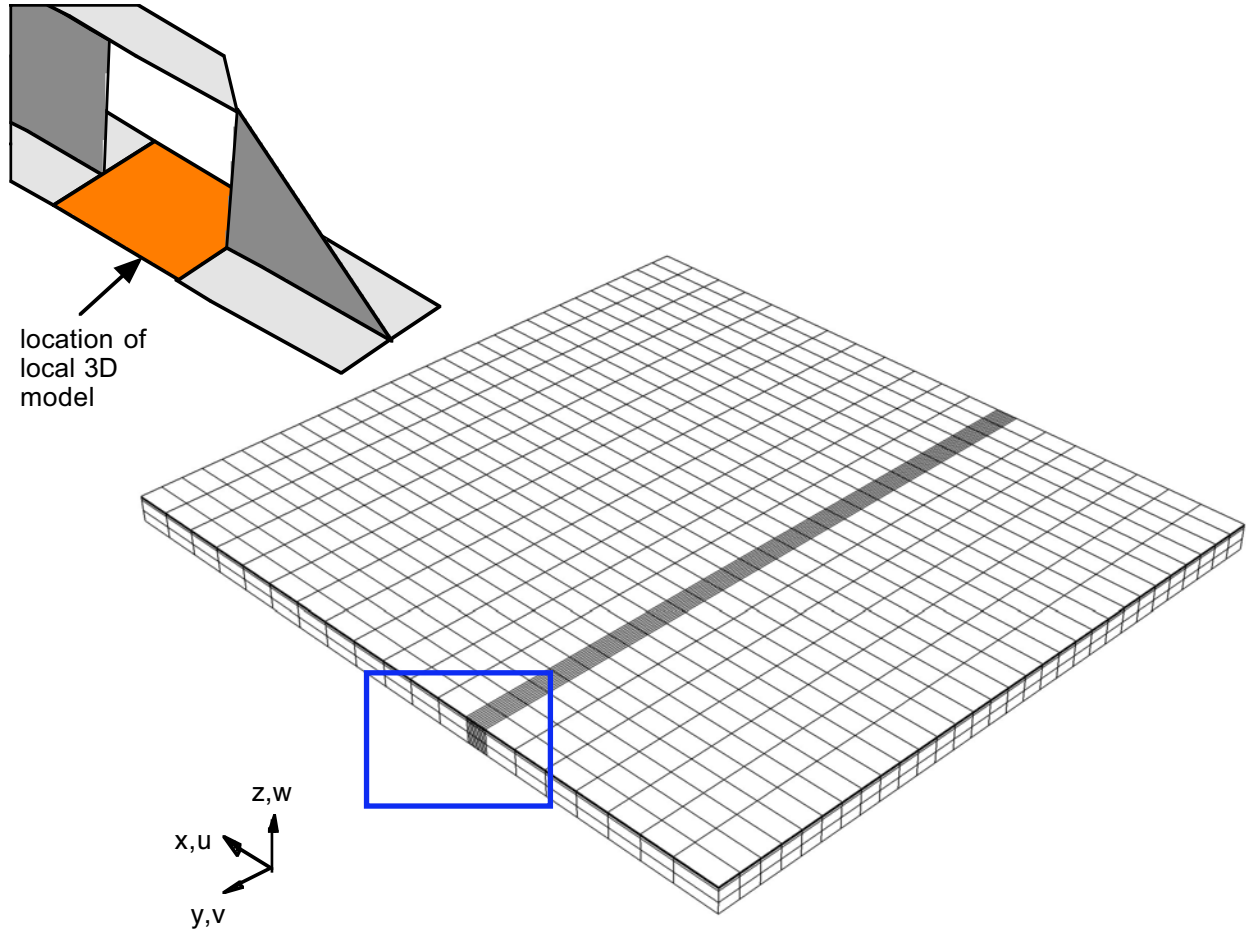


a. Cross section of local 3D T-stiffener model.

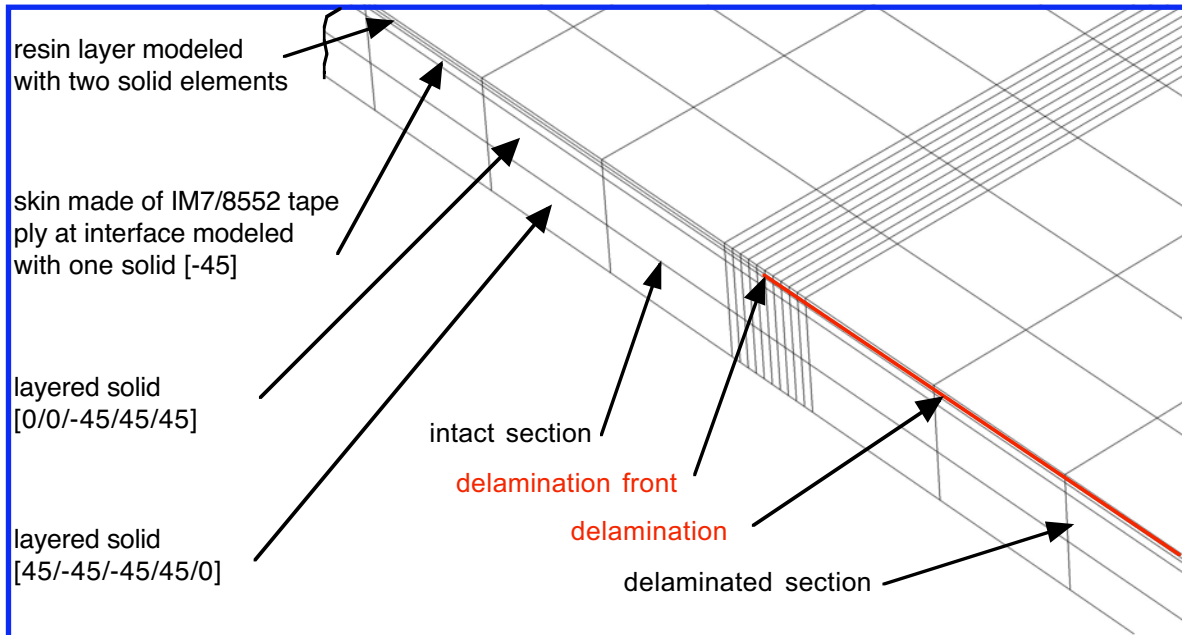


b. Cross section of assembled models.

Figure 11. Combined 3D T-stiffener and local 3D skin/delamination model.

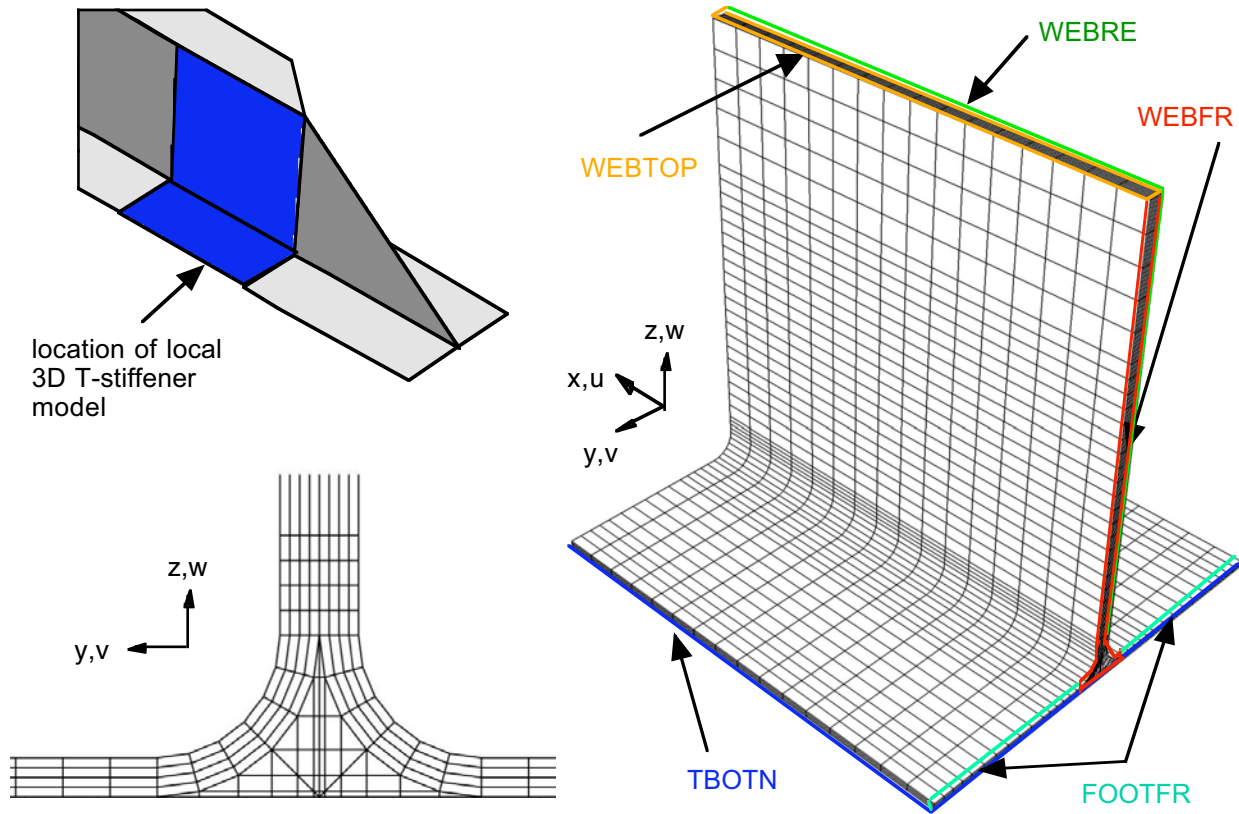


a. Local 3D skin/delamination model with uniform mesh across the width.

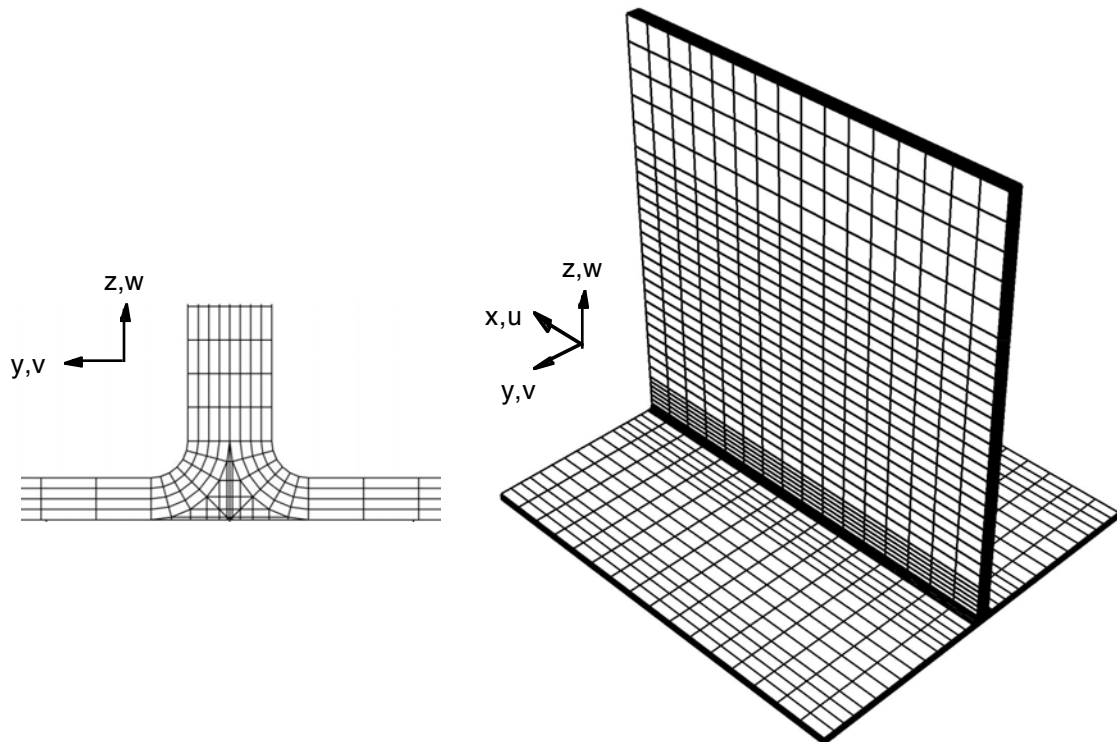


b. Detail of local 3D skin/delamination model around delamination front.

Figure 12. Local model for combination with T-stiffener model (L3).

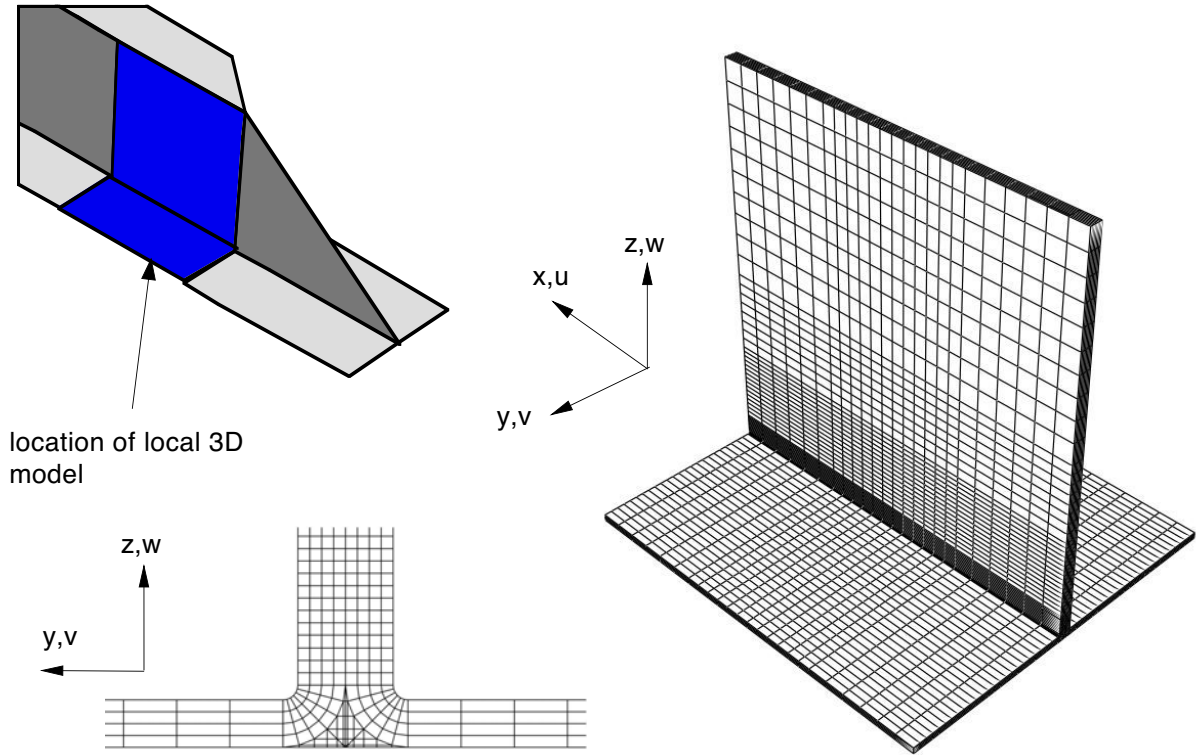


a. Local 3D T-stiffener model for  $r=2.54$  mm with surfaces for shell to solid coupling.

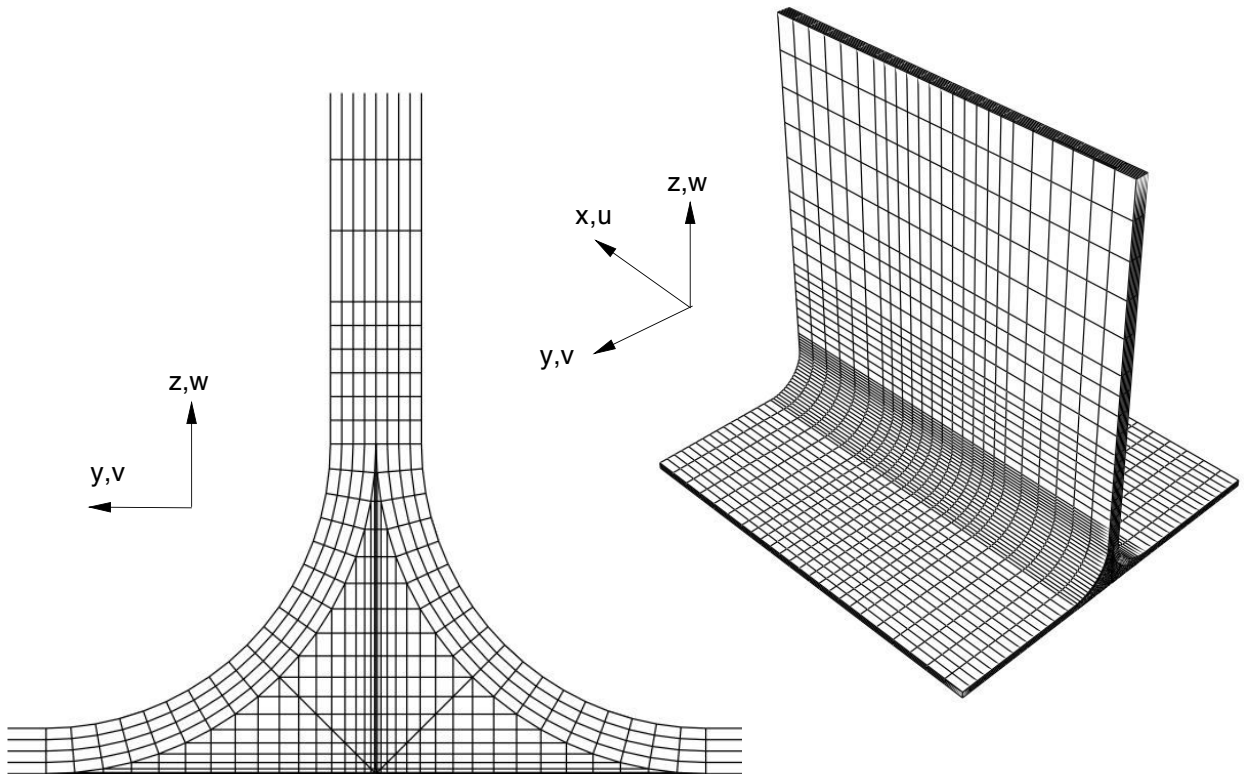


b. Local 3D T-stiffener model for  $r=0.711$  mm.

Figure 13. Local 3D T-stiffener model.



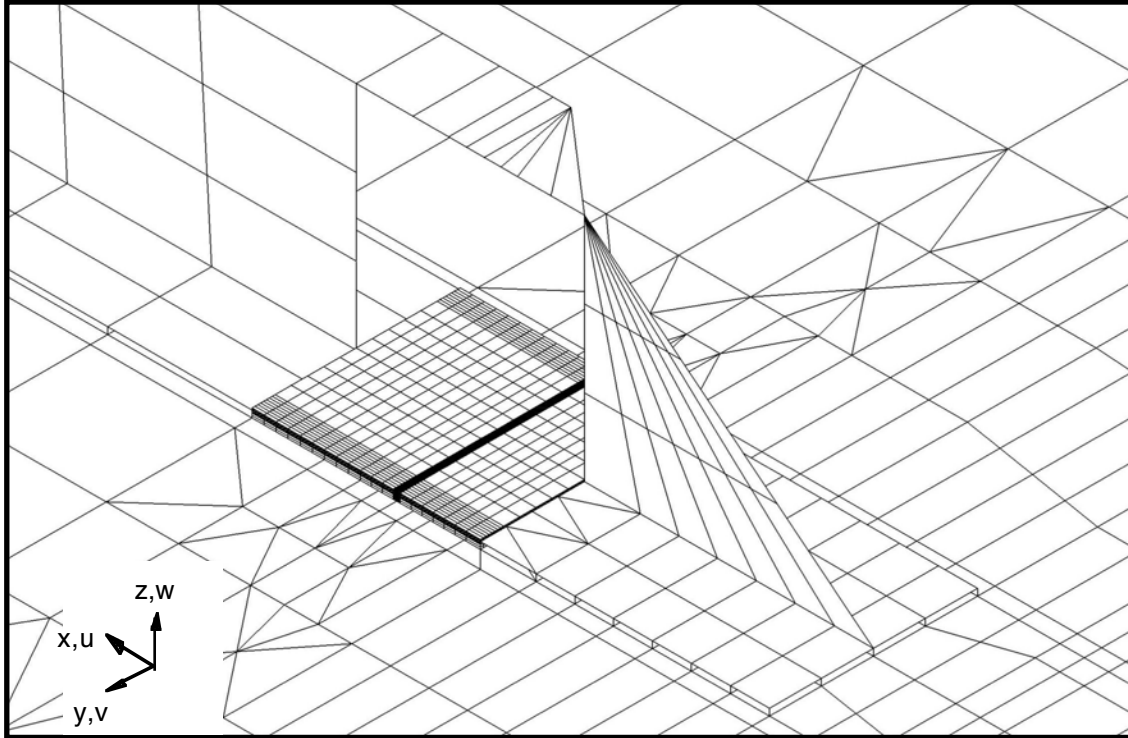
a. Local 3D *T*-stiffener model for  $r=0.254$  mm.



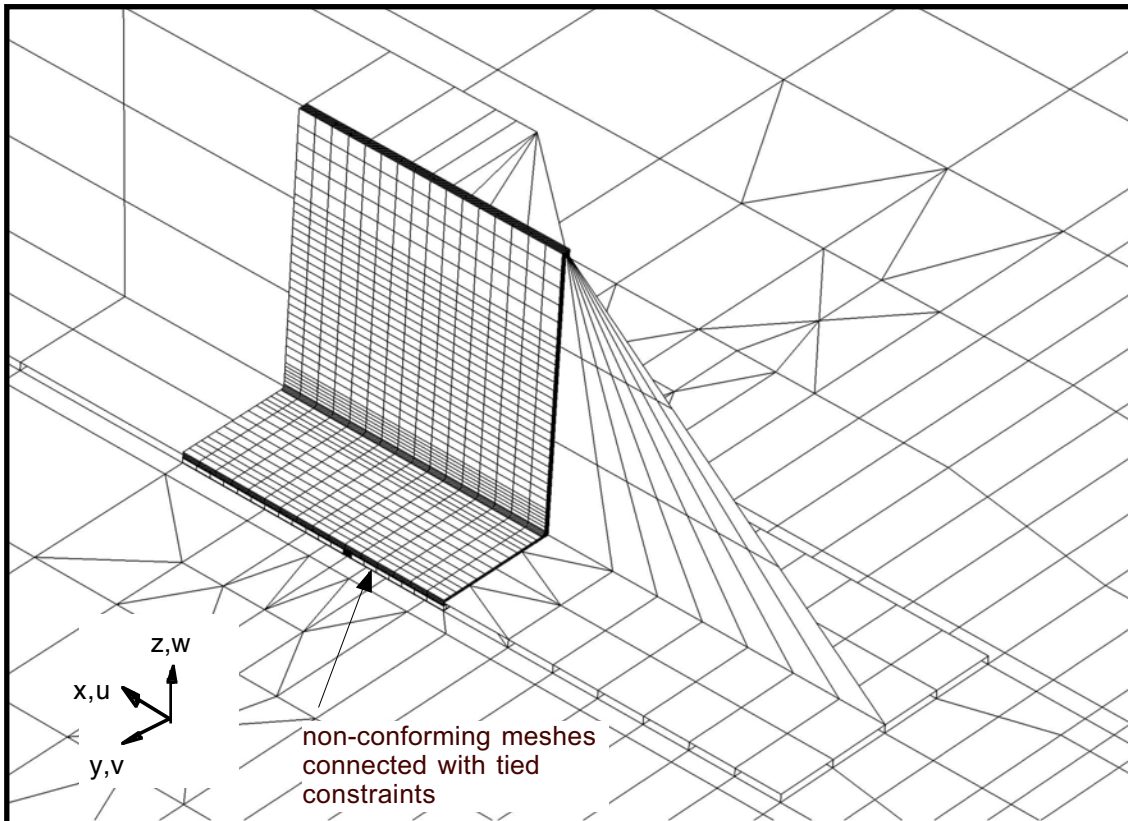
b. Local 3D *T*-stiffener model for  $r=5.08$  mm.

Figure 14. Local 3D *T*-stiffener models.





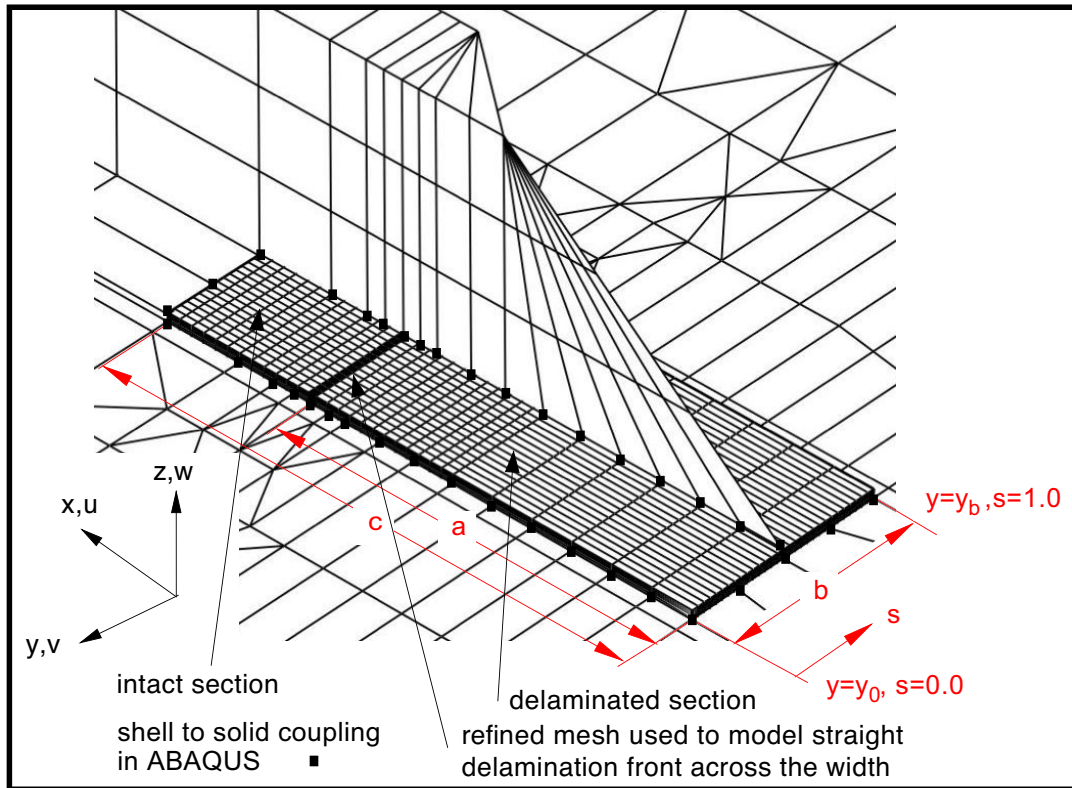
a. Stiffener termination with local 3D skin/delamination model in place.



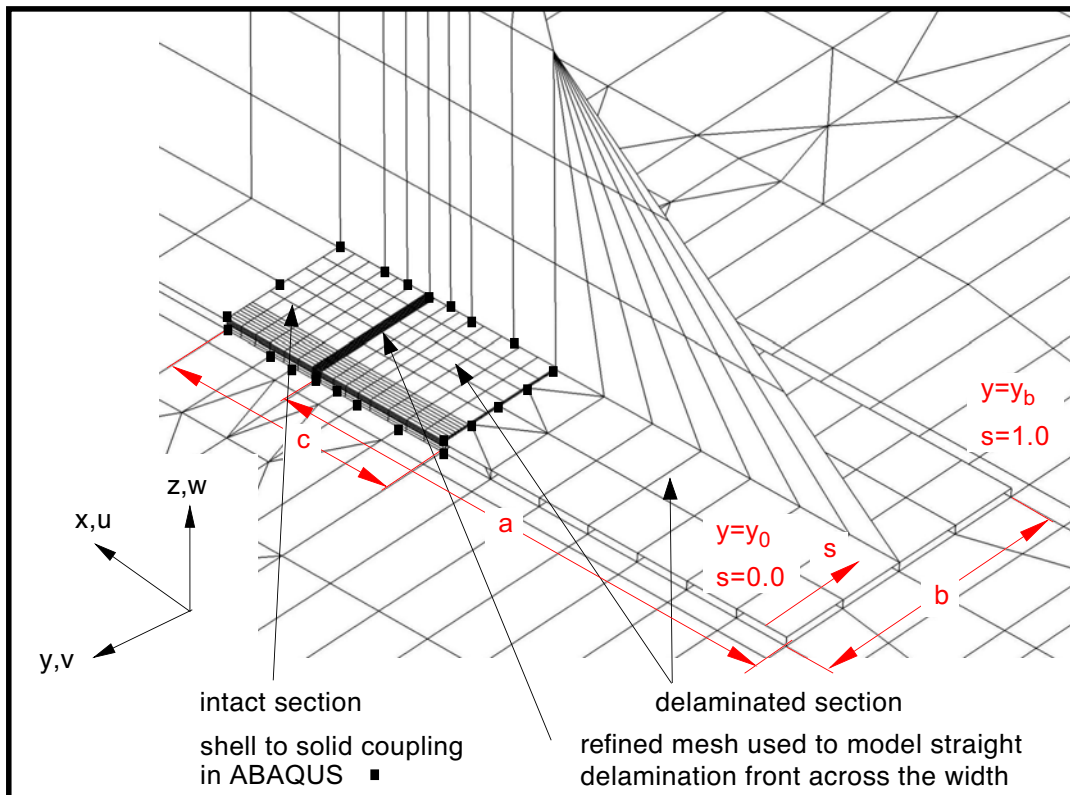
b. Combined local 3D skin/delamination model and 3D T-Stiffener model.

Figure 15. Joint shell and local 3D models.



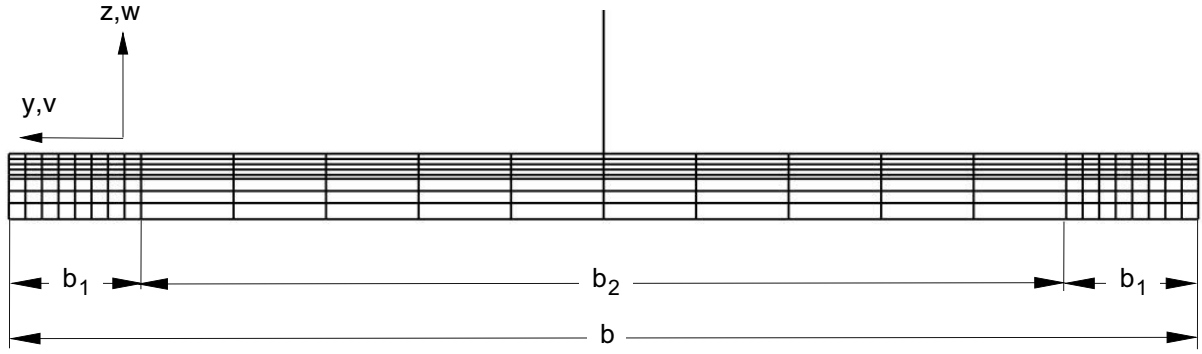


a. Detail of center stiffener with local 3D insert (Axxx).

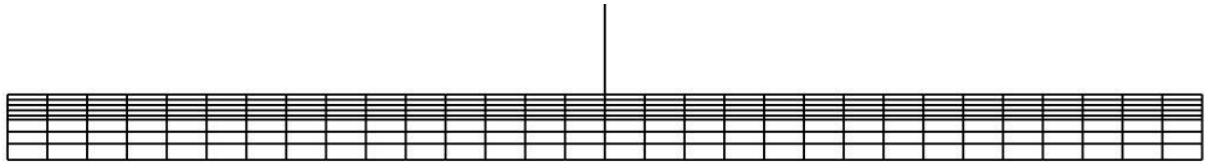


b. Detail of center stiffener with local 3D insert (Bxxx).

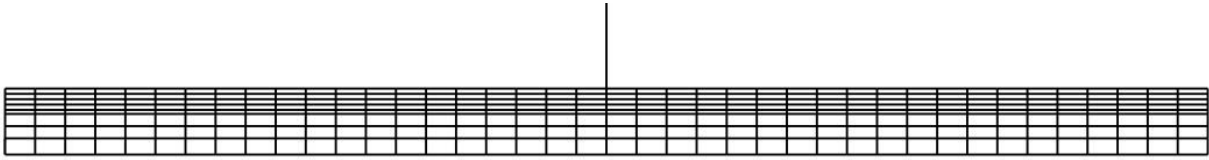
Figure 17. Local 3D skin/foot/delamination models for 81.9 mm delamination length.



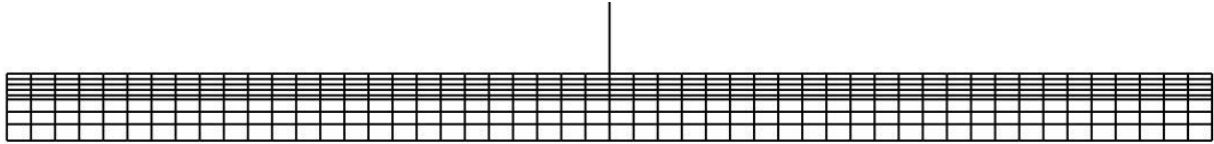
a. Model with refined mesh near the edges (AF-8/10/8, BF-8/10/8).



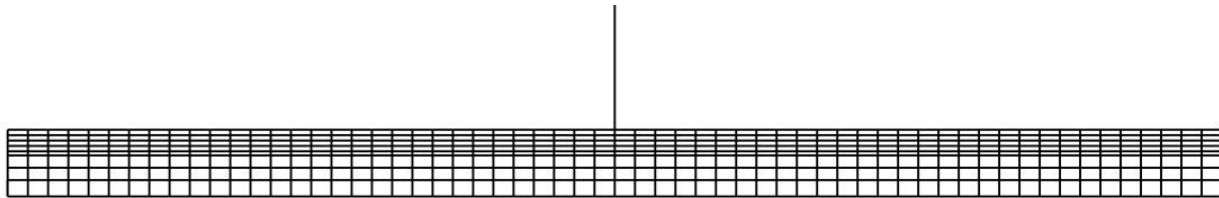
b. Model with 30 elements across the width (AF-U30, BF-U30).



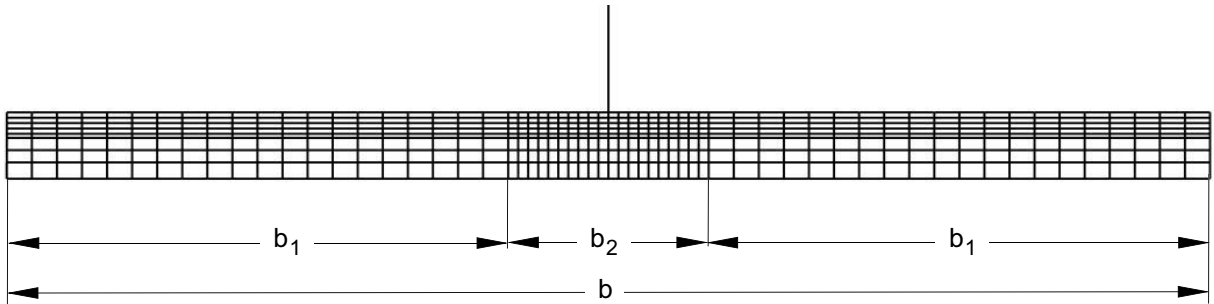
c. Model with 40 elements across the width (AF-U40, BF-U40).



d. Model with 50 elements across the width (AF-U50, BF-U50).



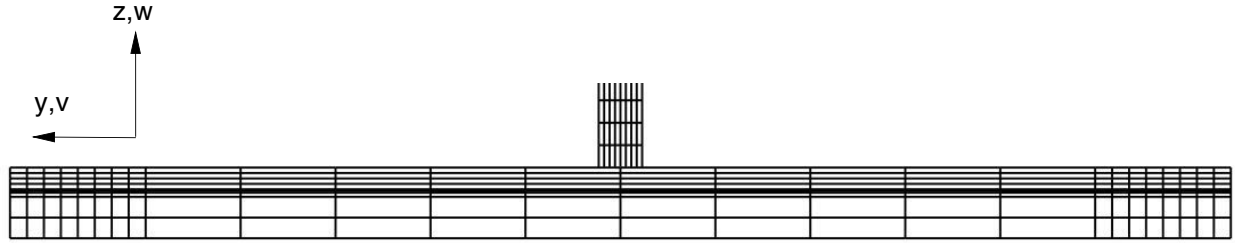
e. Model with 60 elements across the width (AF-U60, BF-U60).



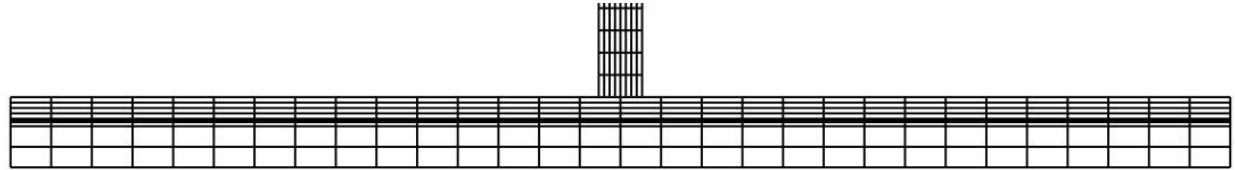
f. Model with refined mesh in the center (AF-20/20/20, BF-20/20/20).

Figure 18. Modeling approaches for skin/stiffener panel.

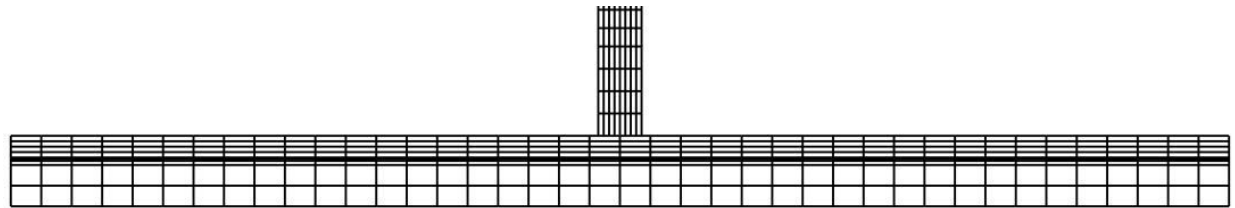




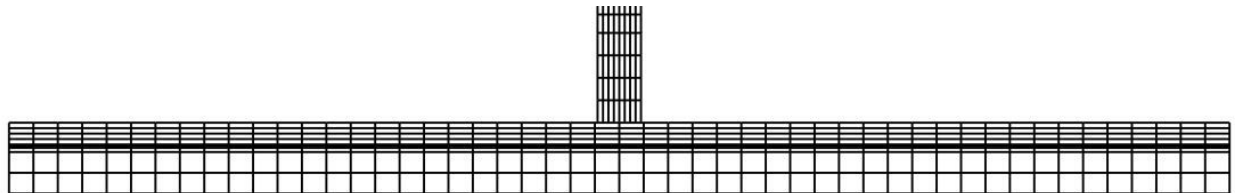
a. Model with refined mesh near the edges (TFL3-8/10/8).



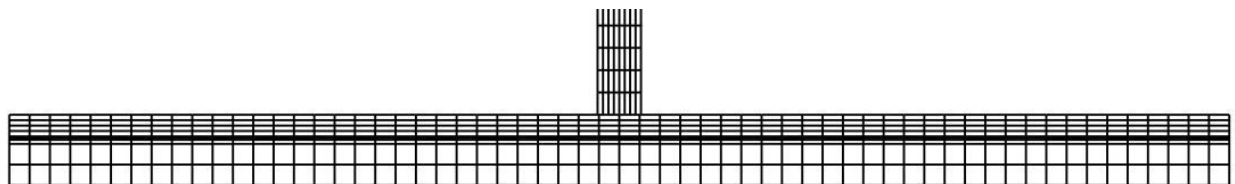
b. Model with 30 elements across the width (TFL3-U30).



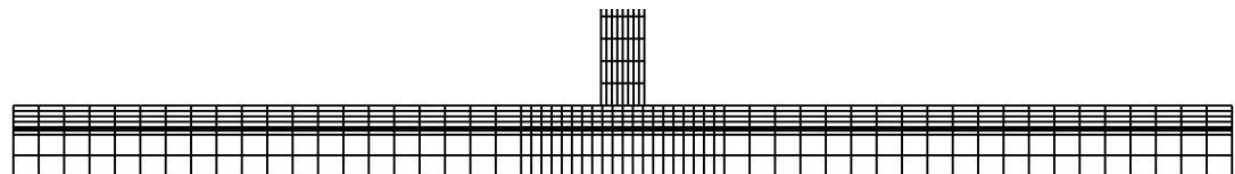
c. Model with 40 elements across the width (TFL3-U40).



d. Model with 50 elements across the width (TFL3-U50).

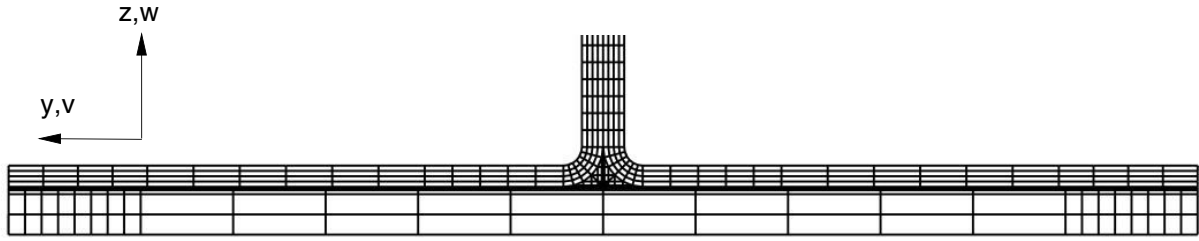


e. Model with 60 elements across the width (TFL3-U60).

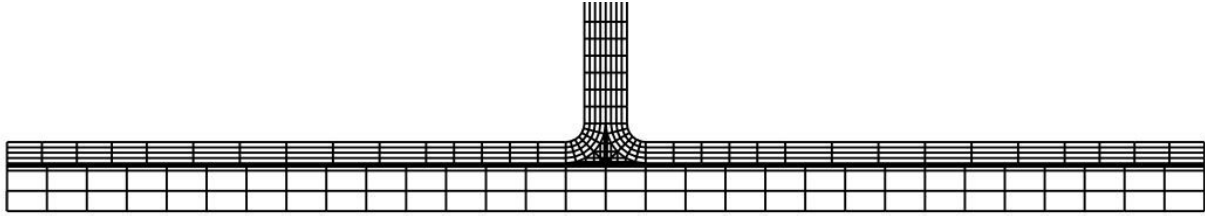


f. Model with refined mesh in the center (TFL3-8/10/8).

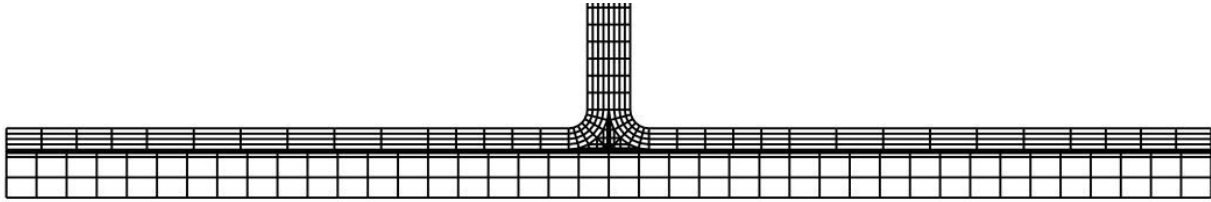
Figure 19. Detail of 3D mesh across the width of the stiffener.



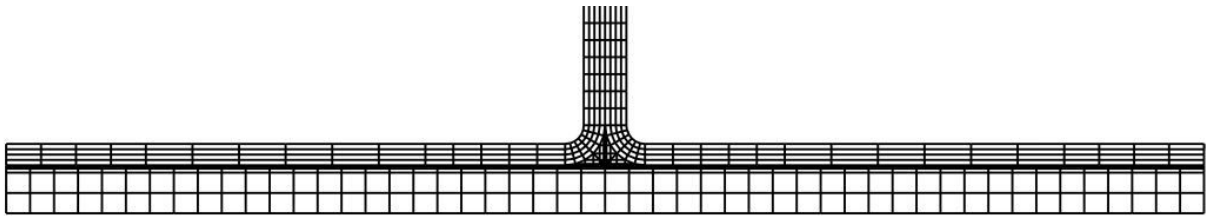
a. Model with refined mesh near the edges (TN1L3C-8/10/8).



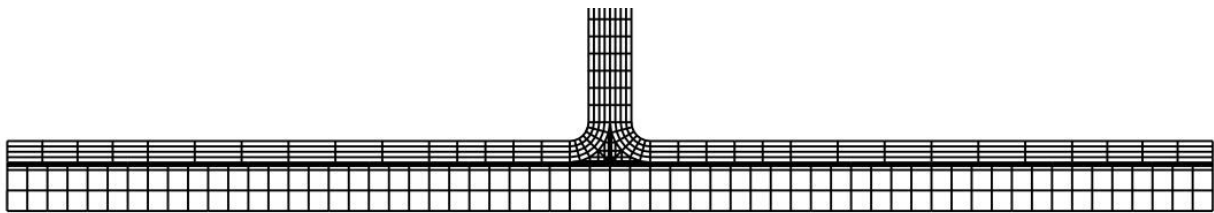
b. Model with 30 elements across the width (TN1L3C-U30).



c. Model with 40 elements across the width (TN1L3C-U40).

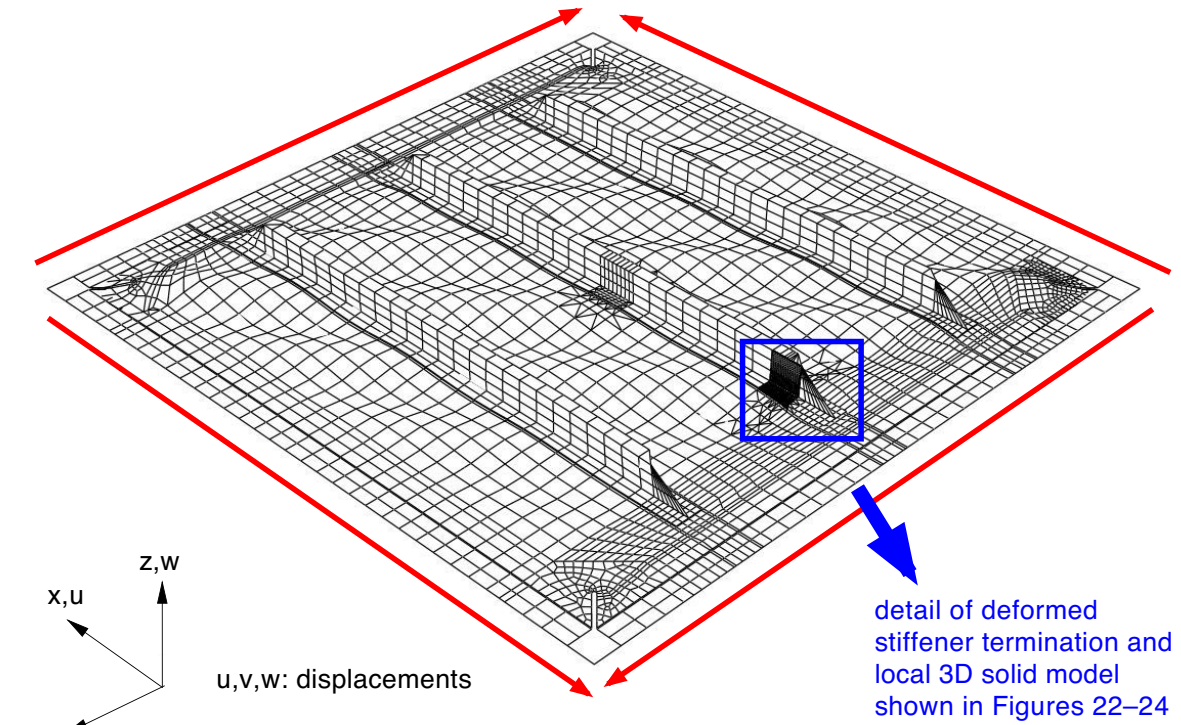


d. Model with 50 elements across the width (TN1L3C-U50).

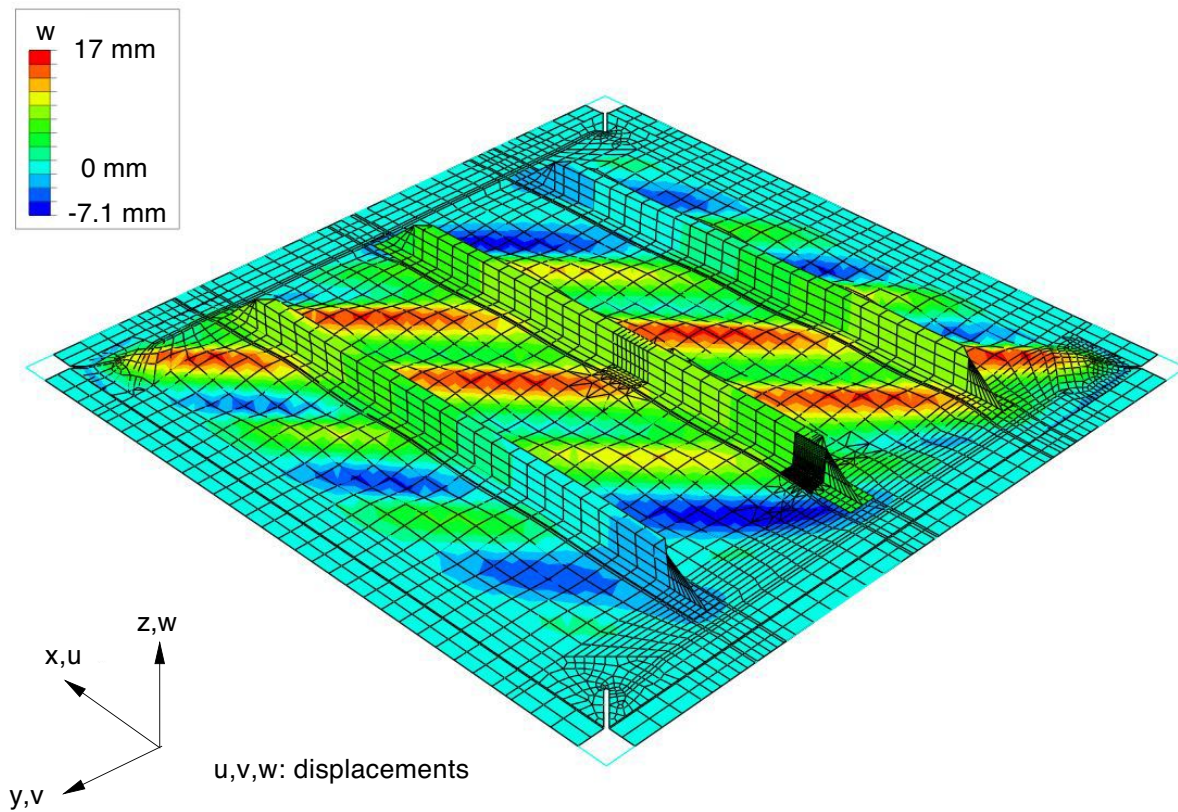


e. Model with 60 elements across the width (TN1L3C-U60).

Figure 20. Detail of 3D mesh across the width of the stiffener (radius  $r=0.711$  mm).

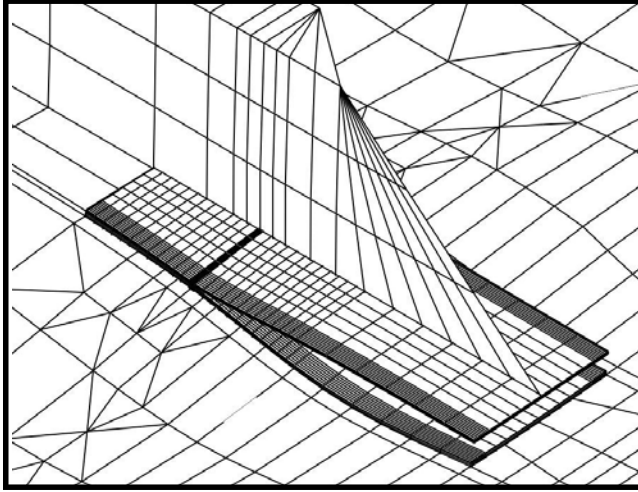


a. Buckled composite panel under shear loading.

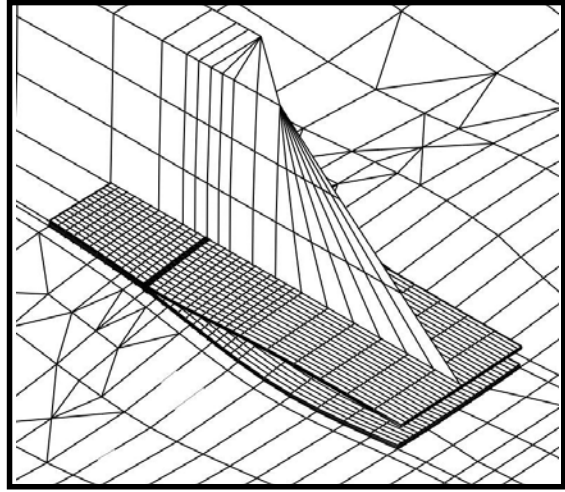


b. Contour plot of out of plane displacement  $w$ .

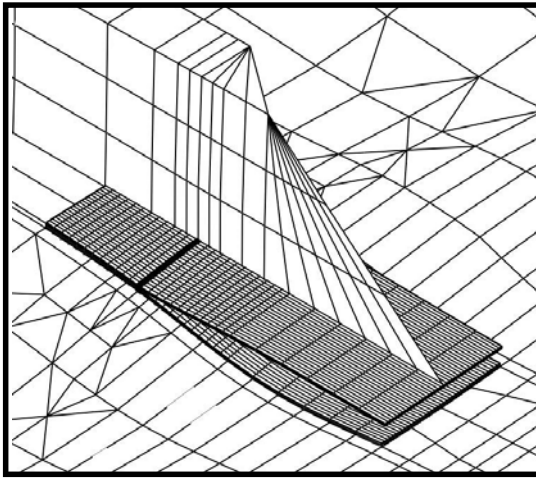
Figure 21. Stiffened composite panel (1016 mm x 1016 mm).



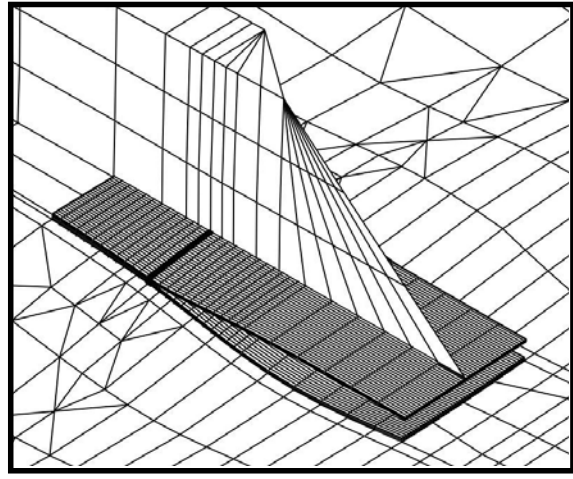
a. Model with refined mesh near the edges  
(AF-8/10/8, AS-8/10/8, AG-8/10/8).



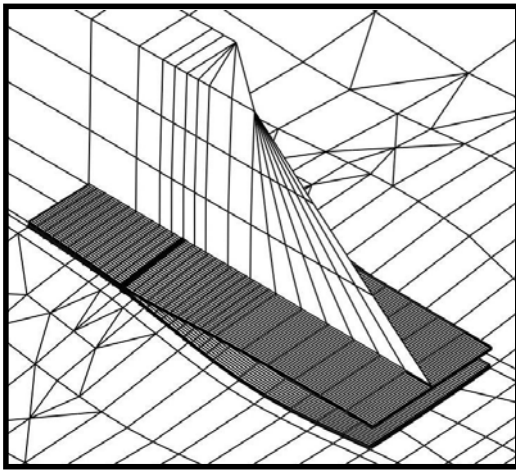
b. Model with 30 elements across the width  
(AF-U30).



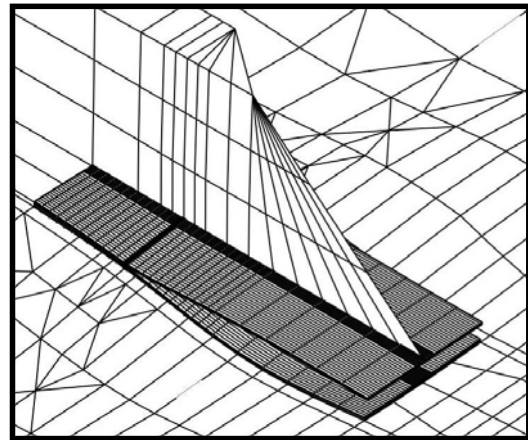
c. Model with 40 elements across the width  
(AF-U40).



d. Model with 50 elements across the width  
(AF-U50).



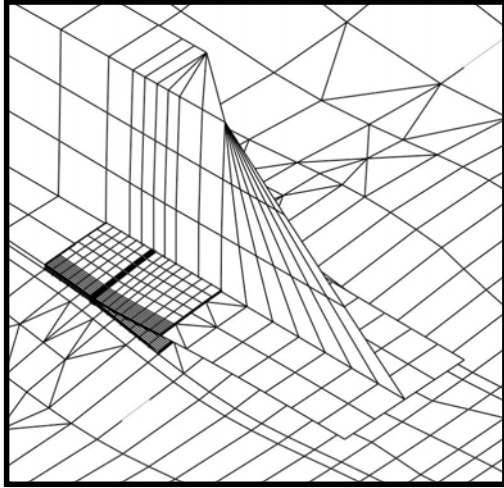
e. Model with 60 elements across the width  
(AF-U60).



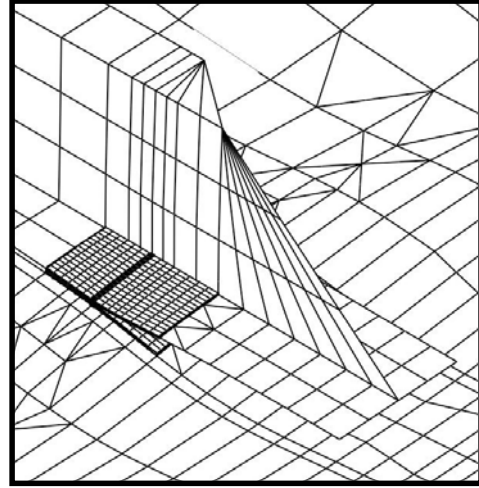
f. Model with refined mesh near the center  
(AF-20/20/20).

Figure 22. Deformed center stiffener with local 3D model of panel skin and stiffener foot.

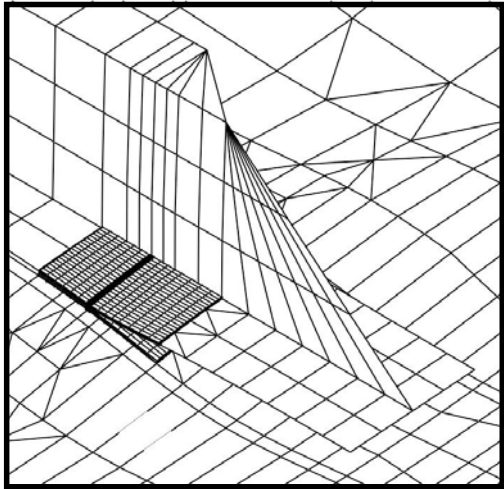




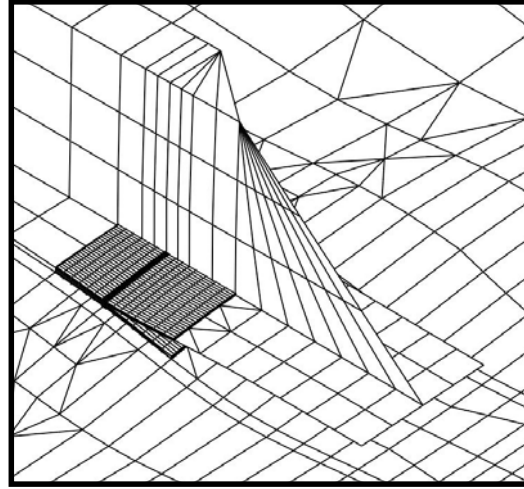
a. Model with refined mesh near the edges  
(BF-8/10/8).



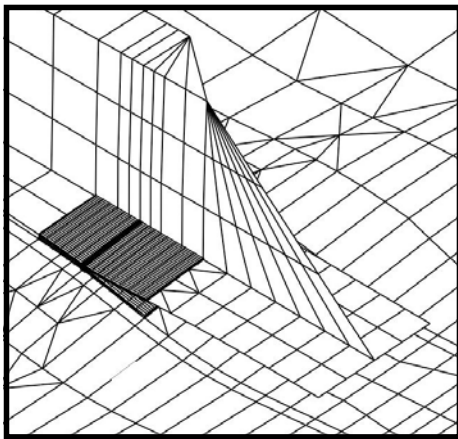
b. Model with 30 elements across the width  
(BF-U30).



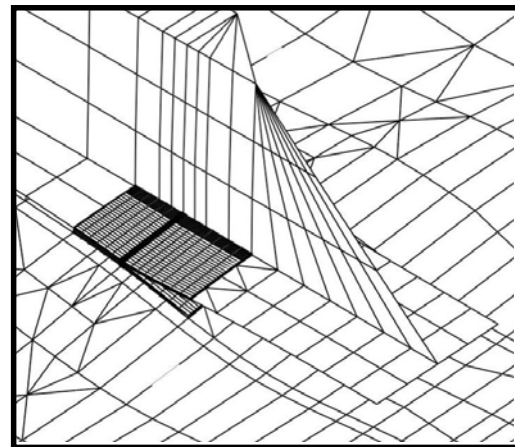
c. Model with 40 elements across the width  
(BF-U40).



d. Model with 50 elements across the width  
(BF-U50).

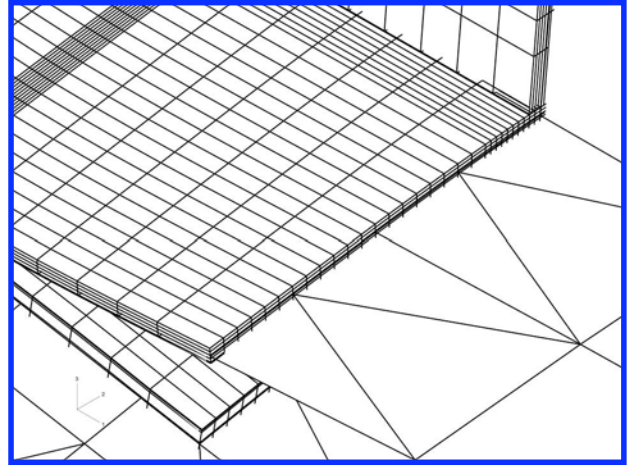
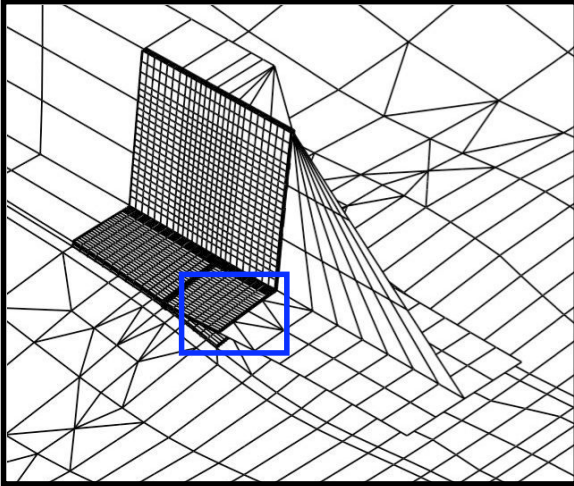


e. Model with 60 elements across the width  
(BF-U60).

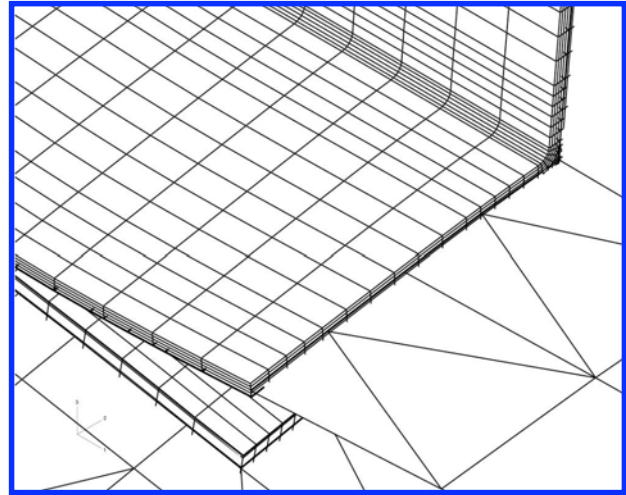
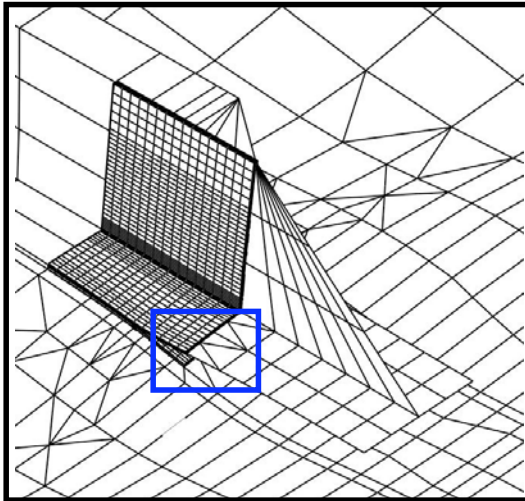


f. Model with refined mesh near the center  
(BF-20/20/20).

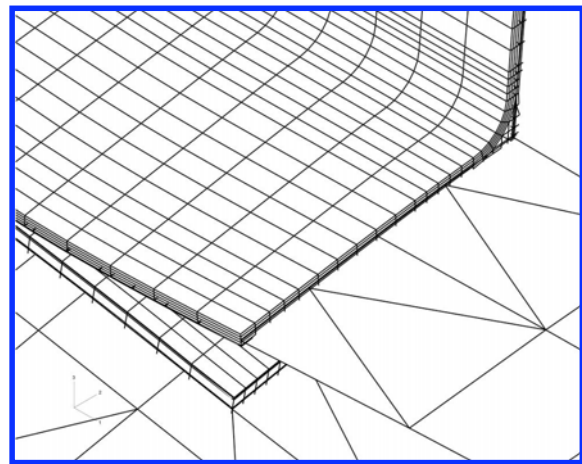
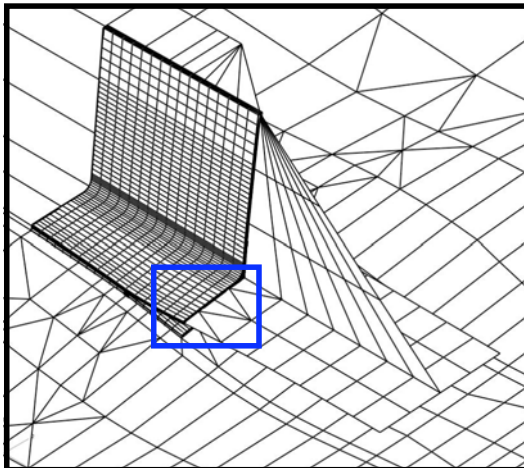
Figure 23. Deformed center stiffener with local 3D model.



a. Deformed finite element model (TFL3-20/20/20).



b. Deformed finite element model for 0.711 mm radius (TN1L3C-20/20/20).



c. Deformed finite element model for 2.54 mm radius (TN2L3C-20/20/20).

Figure 24. Deformed center stiffener with different local 3D models which include the web.

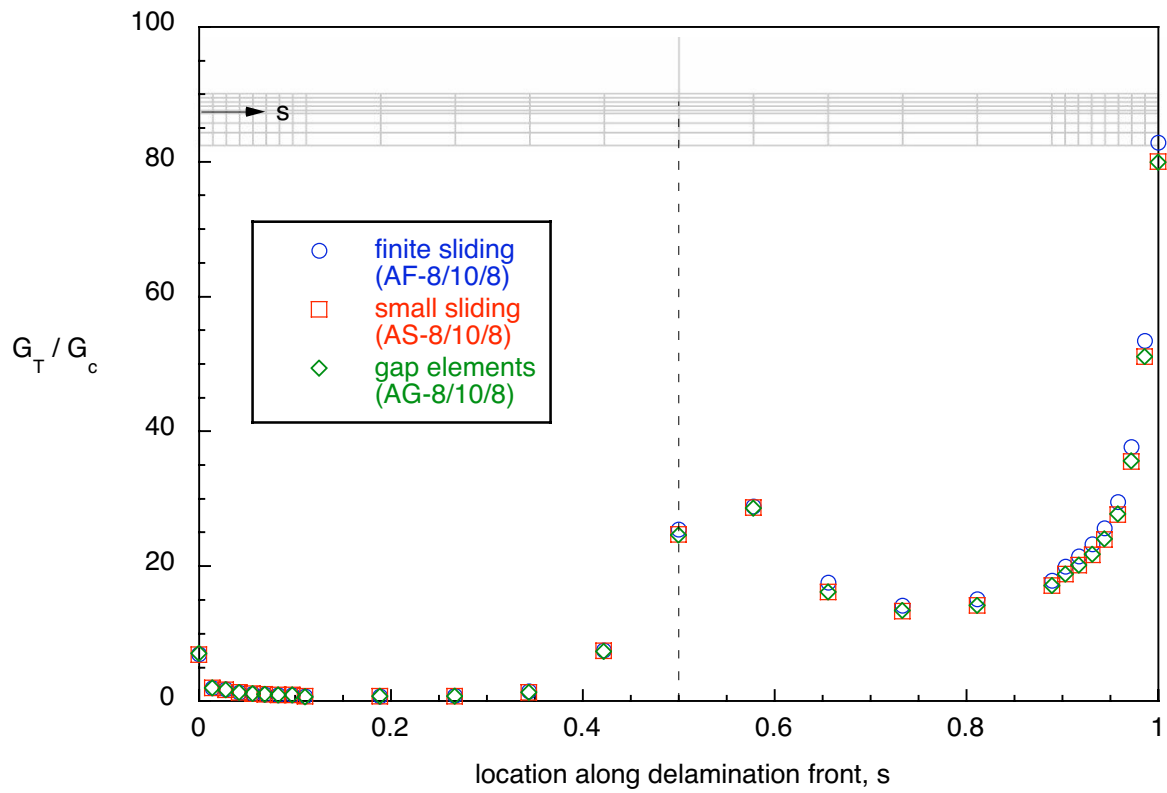


Figure 25. Computed failure index across the width of the stiffener for different contact options.

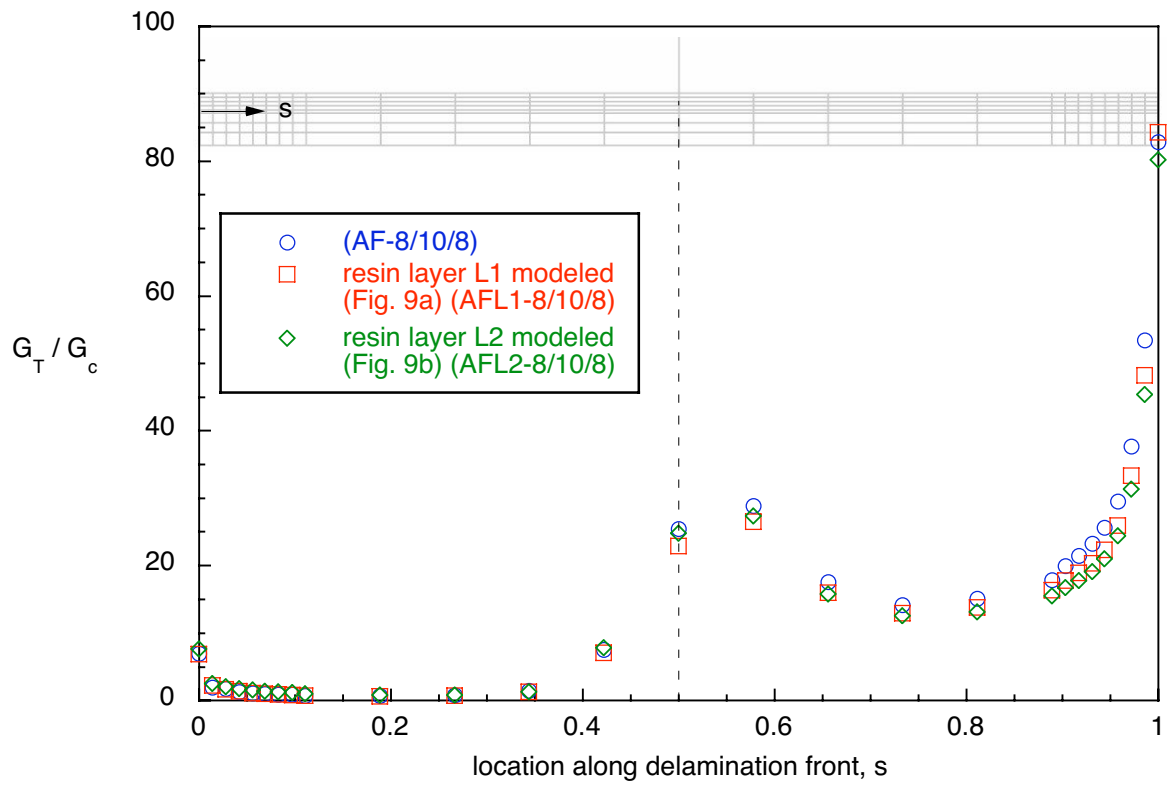


Figure 26. Computed failure index across the width of the stiffener for models including a resin layer.

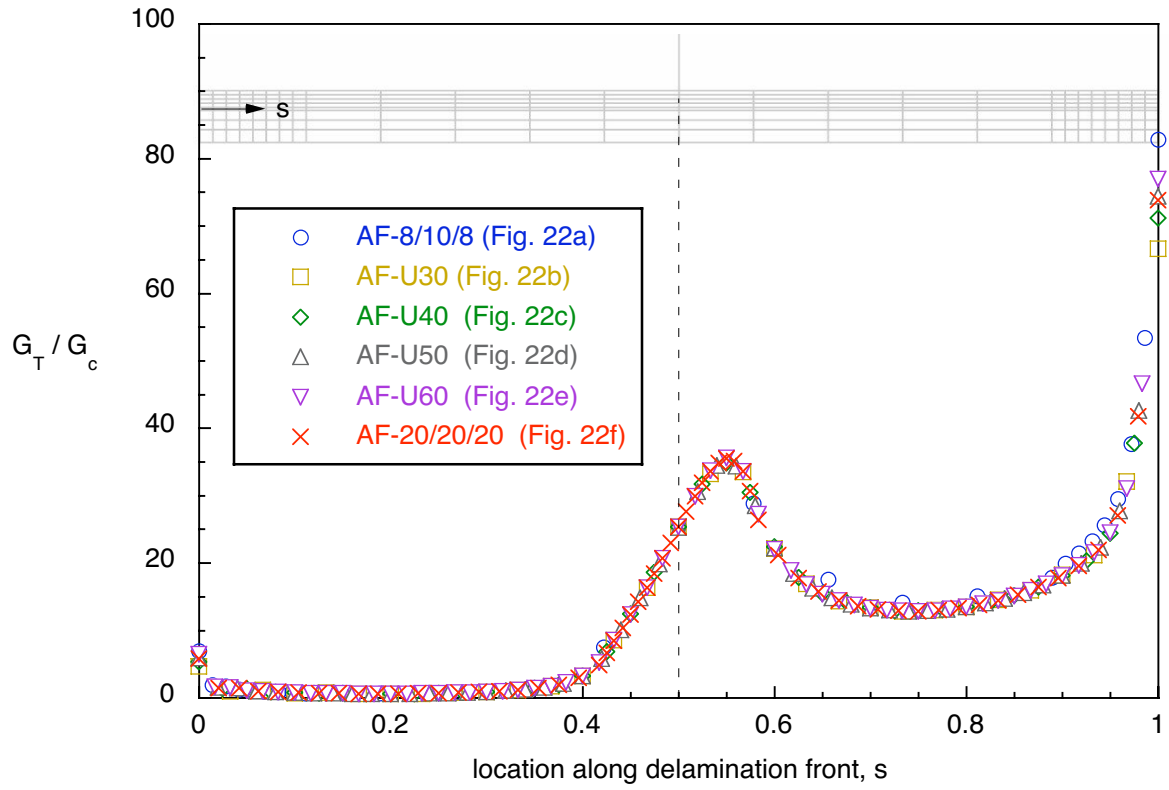


Figure 27. *Computed failure index across the width of the stiffener for models with different mesh refinement.*

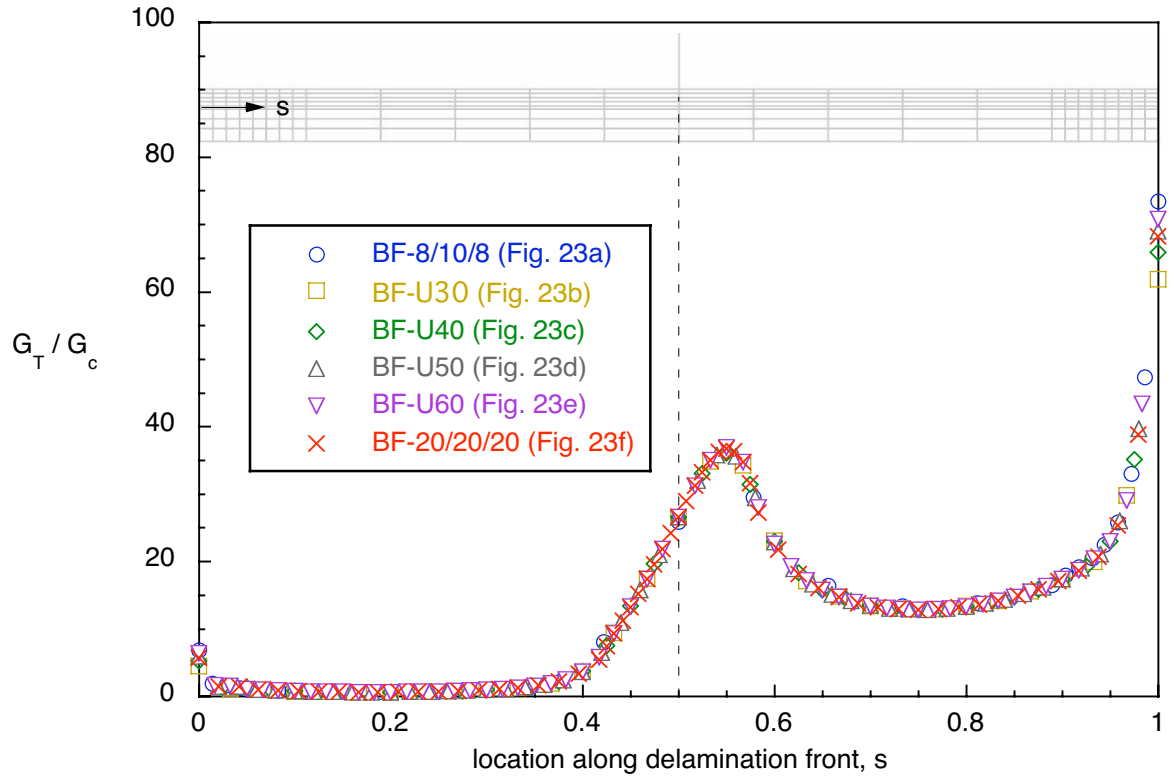


Figure 28. *Computed failure index across the width of the stiffener for models with different mesh refinement.*

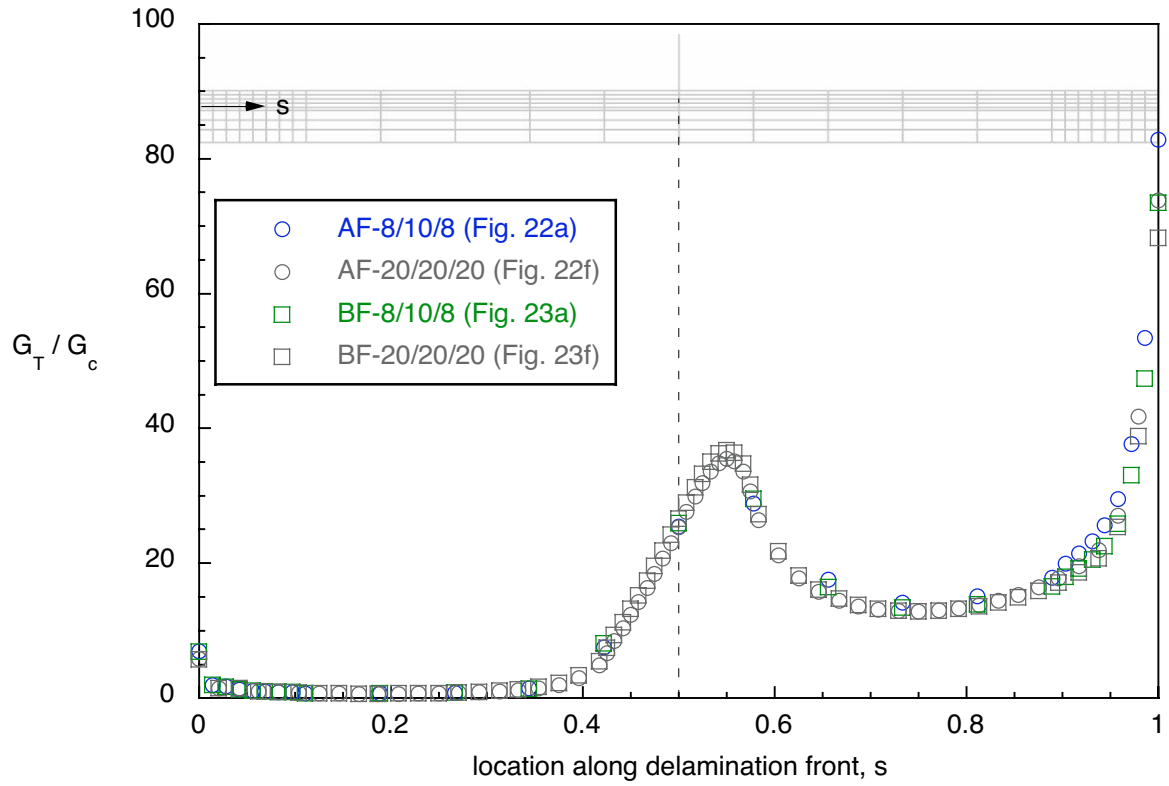


Figure 29. Computed failure index across the width of the stiffener for local 3D models of different length  $c$ .

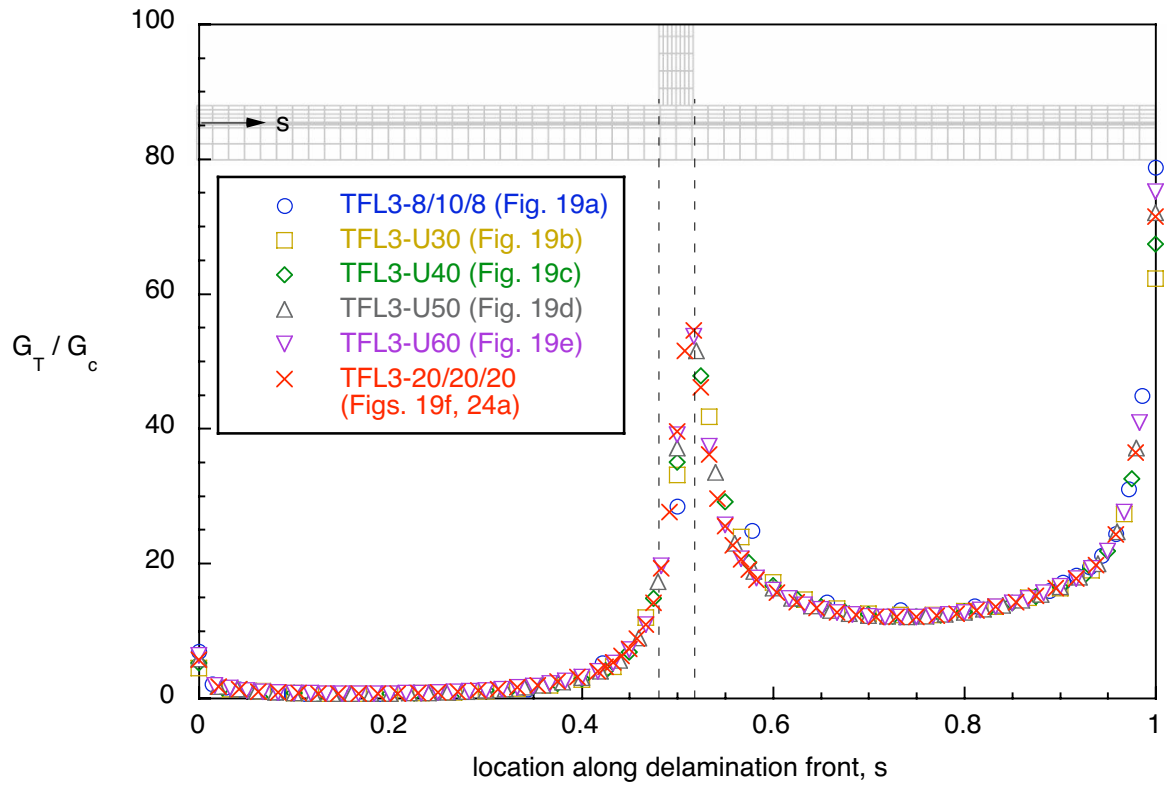


Figure 30. Computed failure index across the width of the stiffener for local 3D models which included the web.

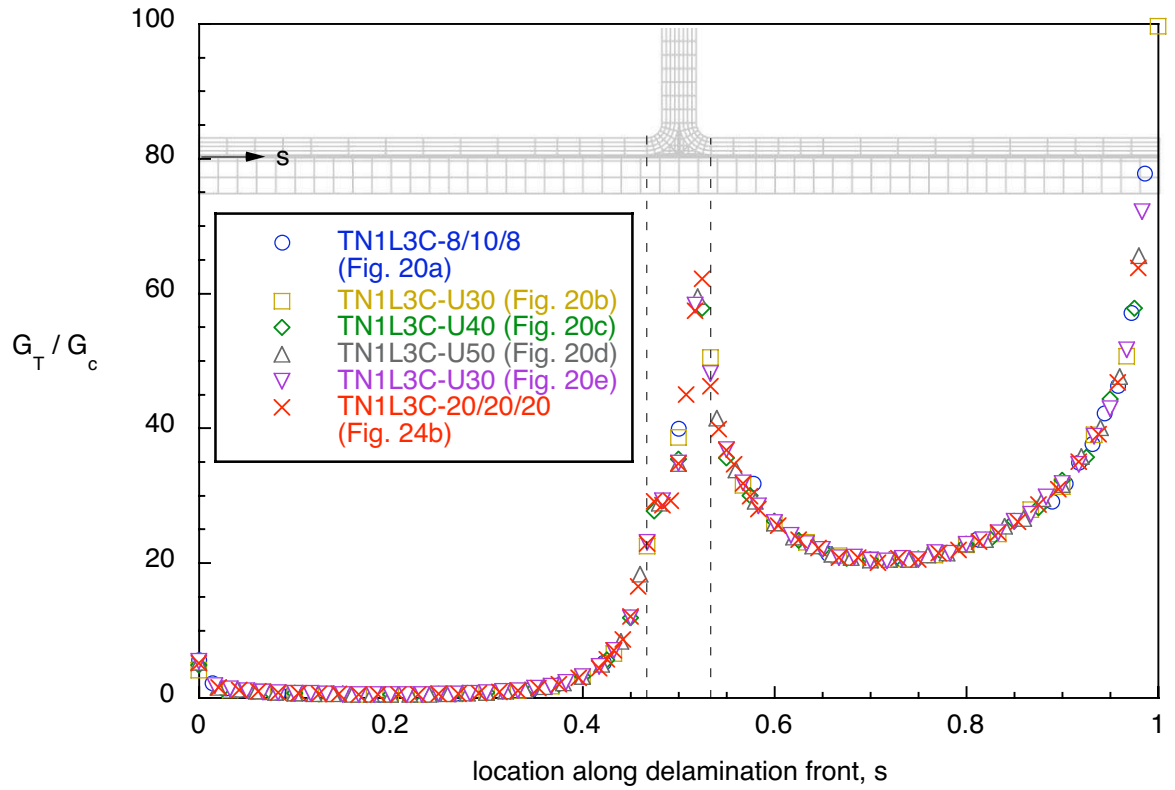


Figure 31. Computed failure index across the width of the stiffener for local 3D models which include the web, noodle and radius ( $r=0.711$  mm).

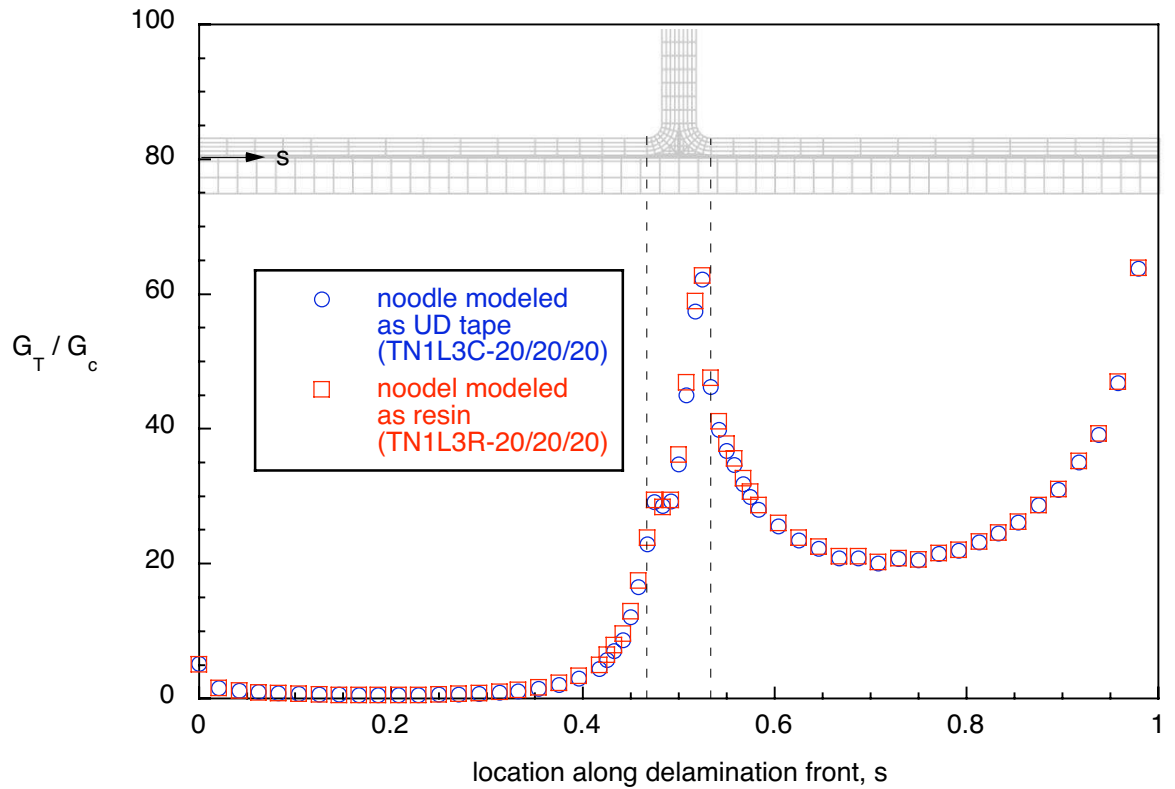


Figure 32. Computed failure index across the width of the stiffener for local 3D models which include the web, noodle and radius ( $r=0.711$  mm).



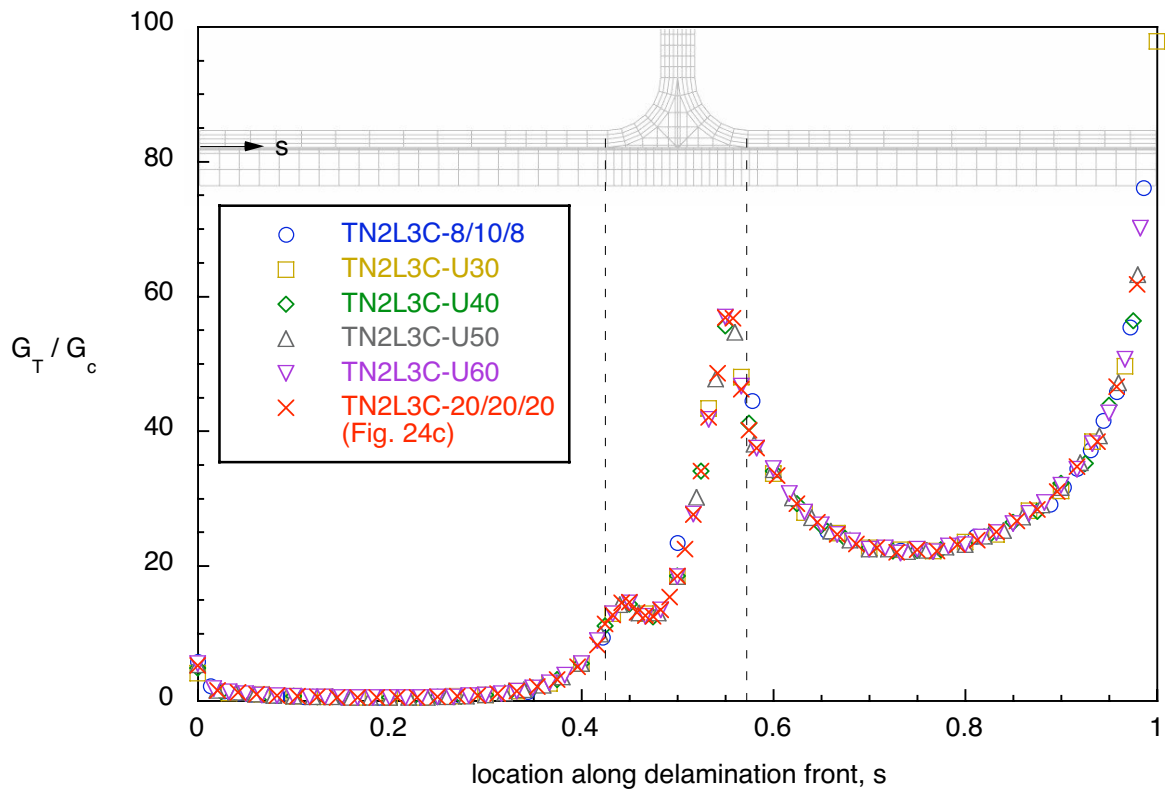


Figure 33. Computed failure index across the width of the stiffener for local solid models which include the web, noodle and radius ( $r=2.54$  mm).

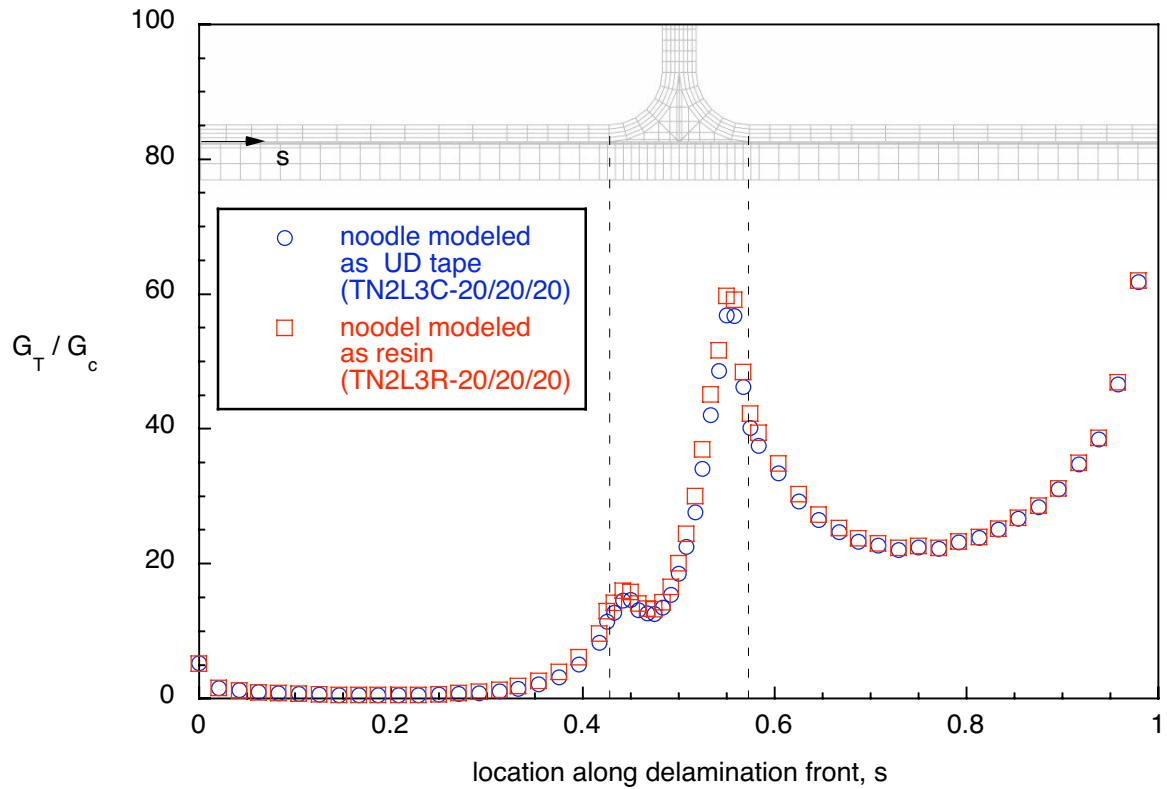


Figure 34. Computed failure index across the width of the stiffener for local 3D models which include the web, noodle and radius ( $r=2.54$  mm).

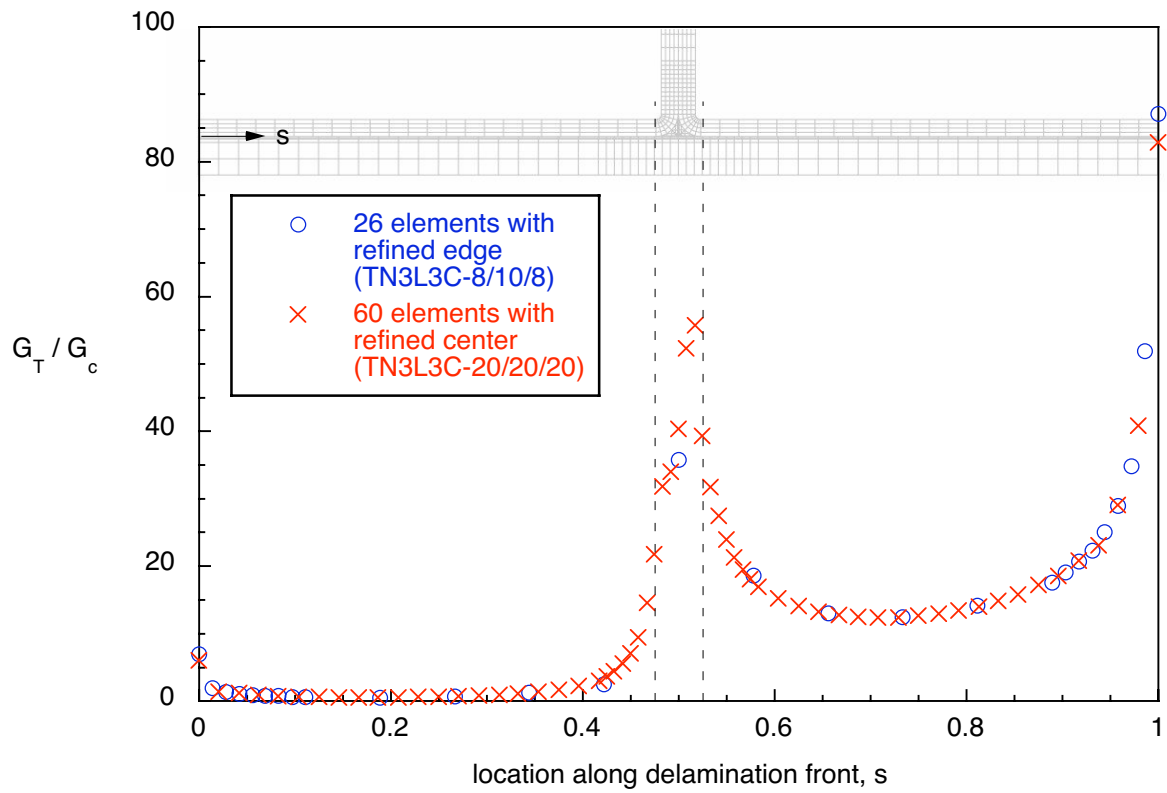


Figure 35. Computed failure index across the width of the stiffener for local solid models which include the web, noodle and radius ( $r=0.254$  mm).

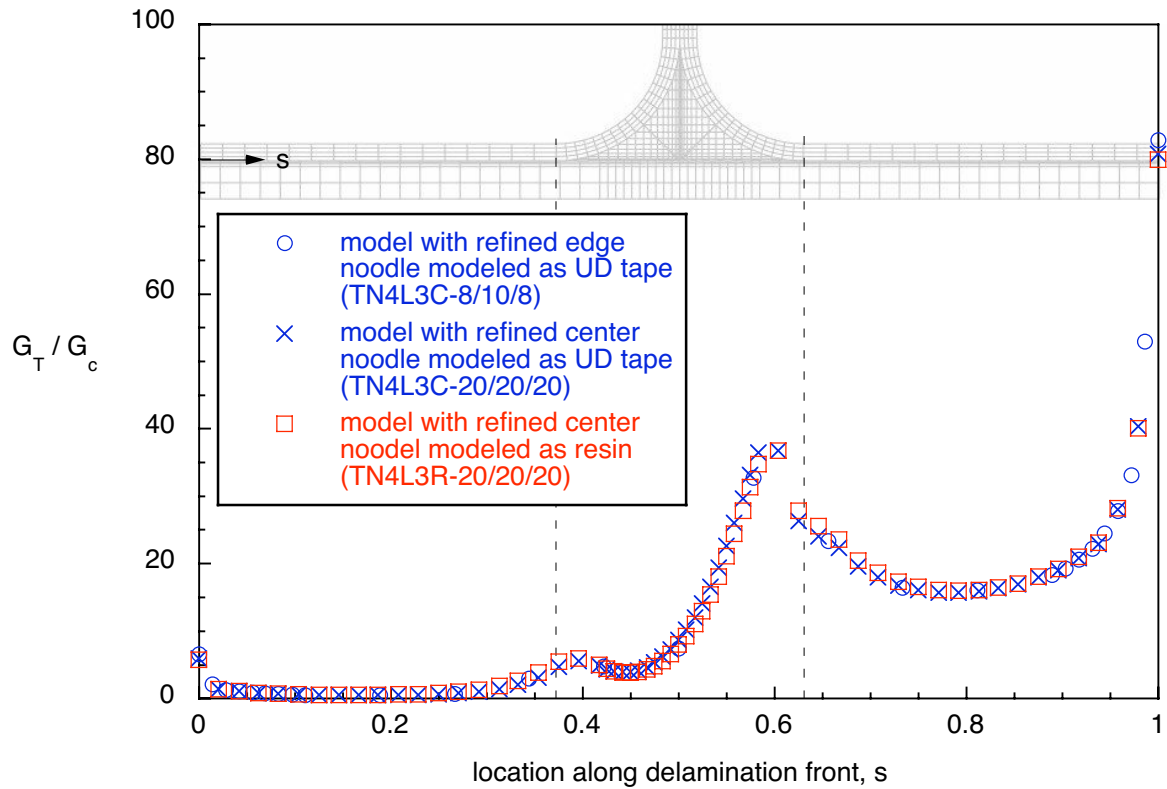


Figure 36. Computed failure index across the width of the stiffener for local solid models which include the web, noodle and radius ( $r=5.08$  mm).



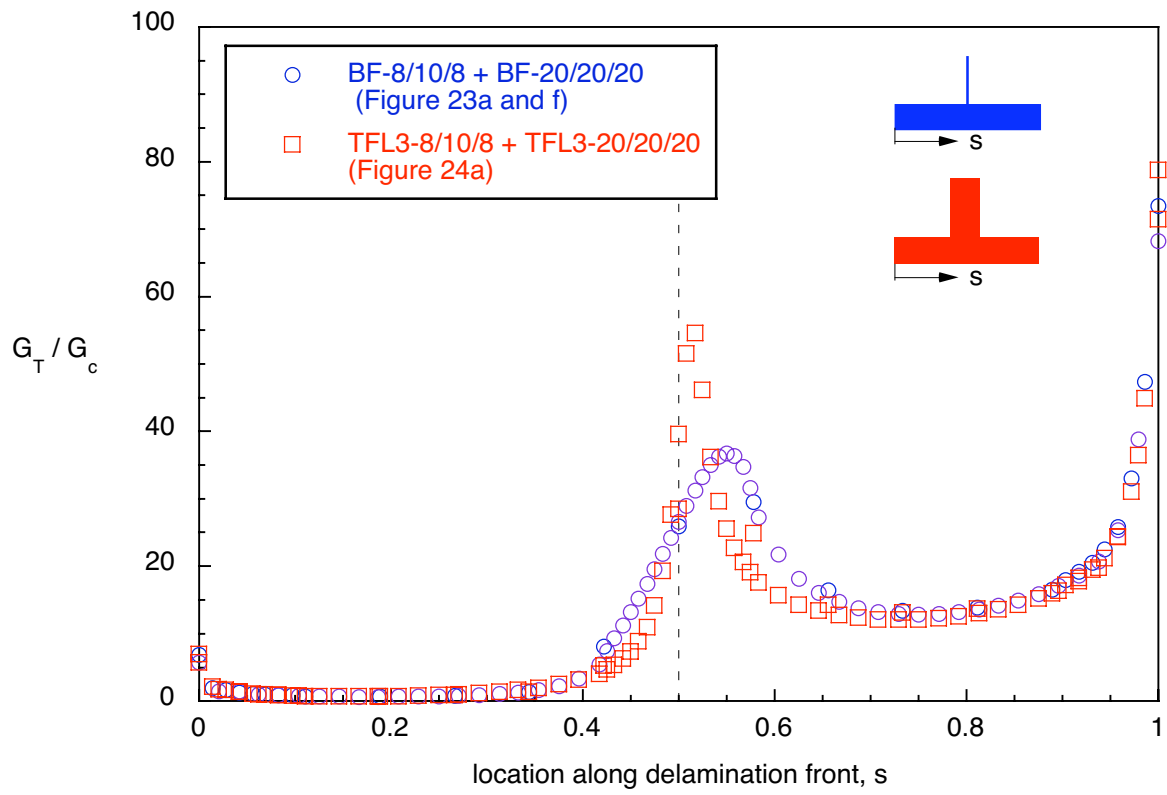


Figure 37. Computed failure index across the width of the stiffener for different local 3D models.

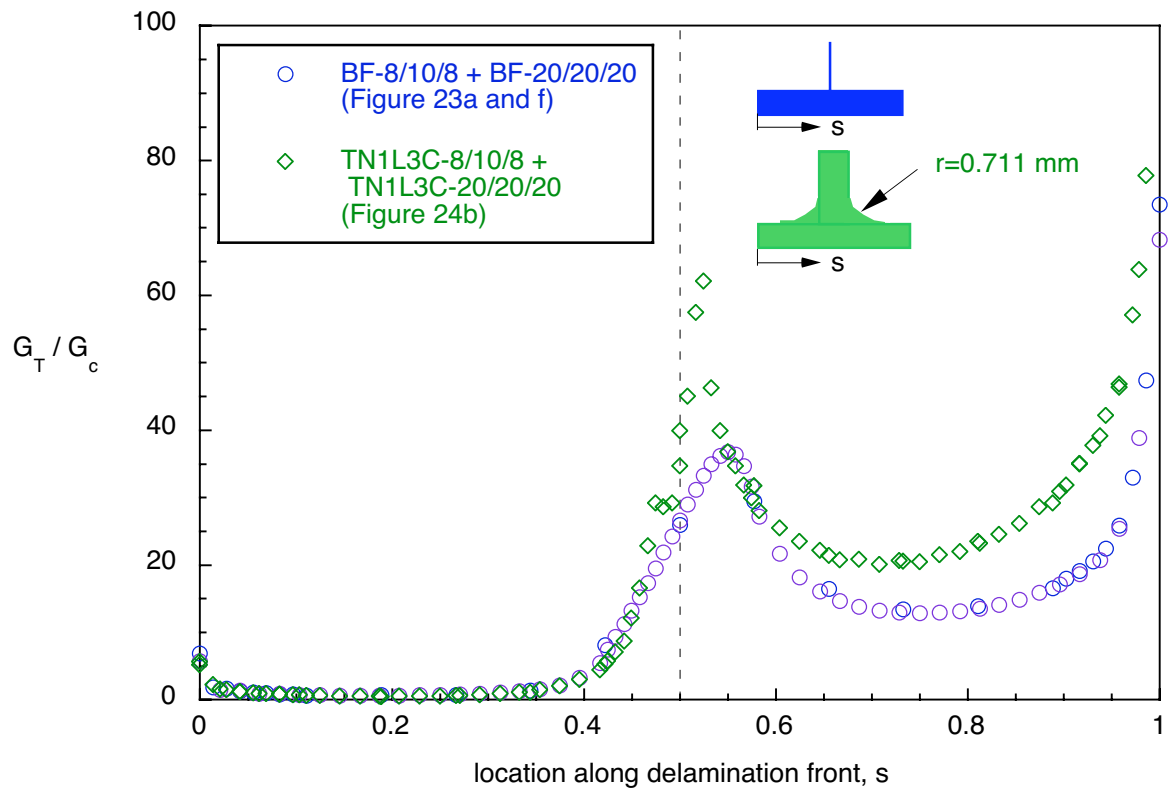


Figure 38. Computed failure index across the width of the stiffener for different local 3D models.

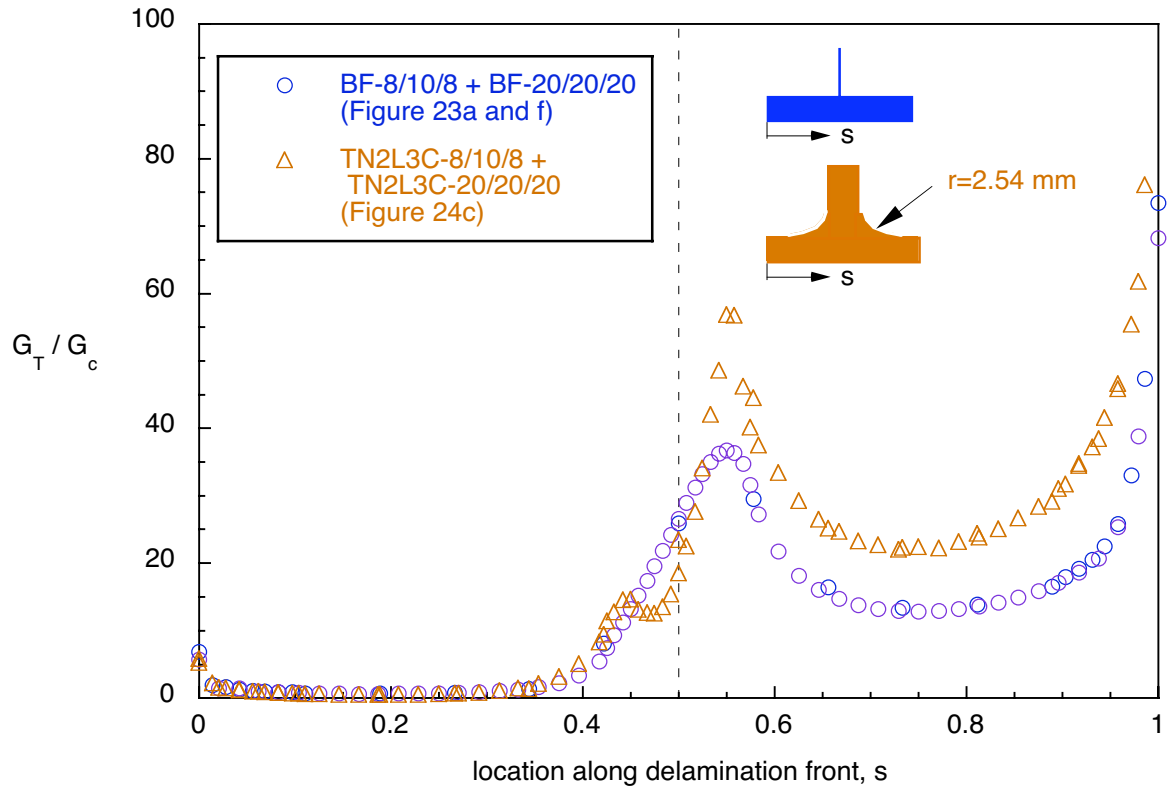


Figure 39. Computed failure index across the width of the stiffener for different local 3D models.

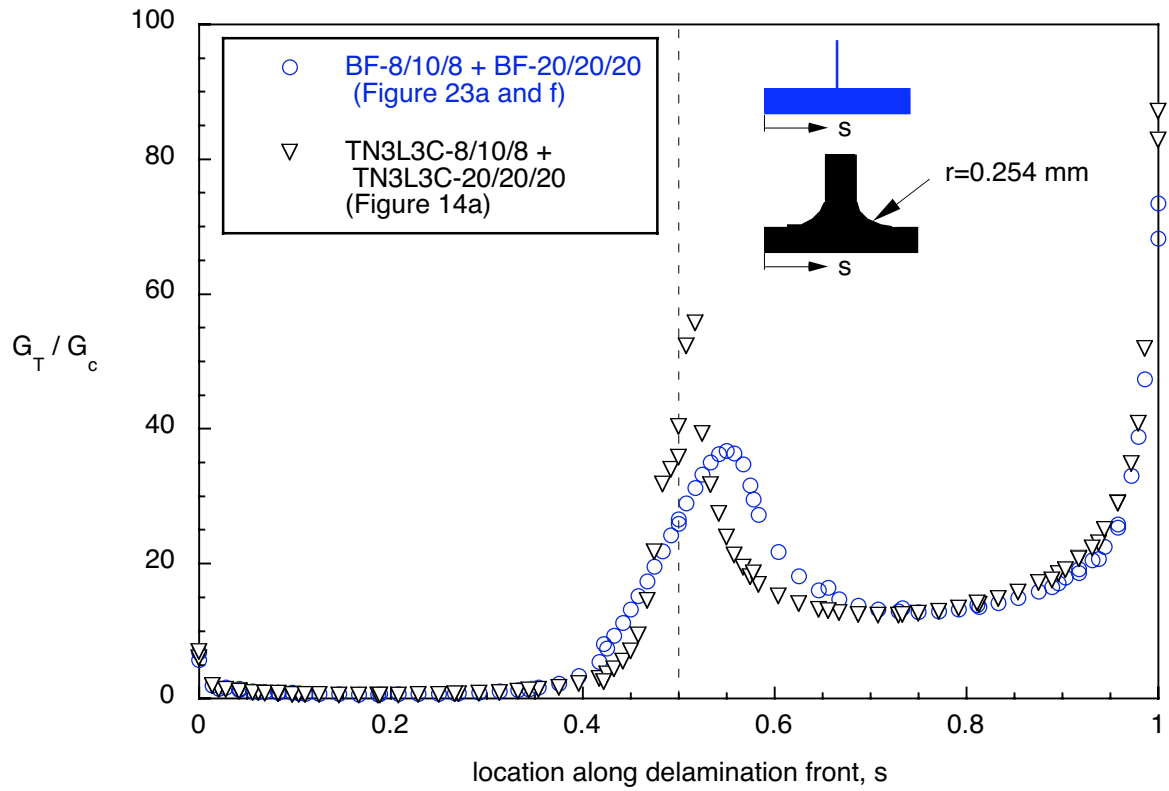


Figure 40. Computed failure index across the width of the stiffener for different local 3D models.

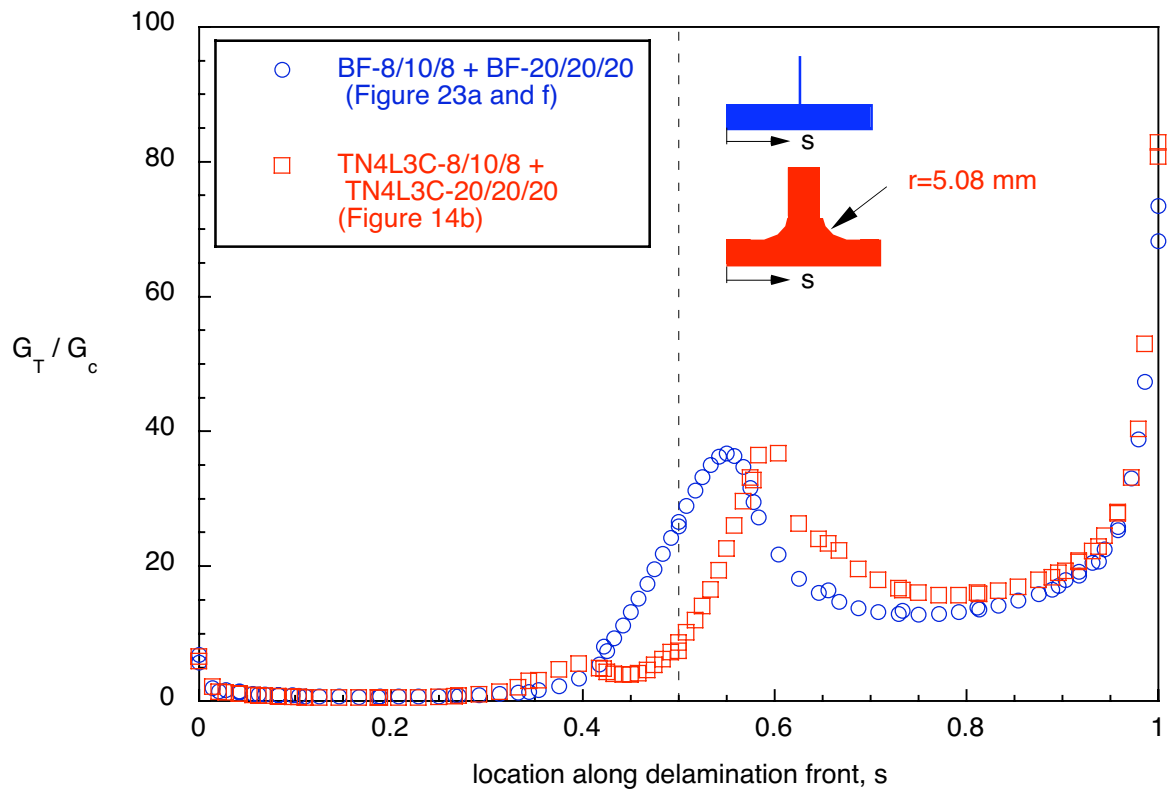


Figure 41. Computed failure index across the width of the stiffener for different local 3D models.

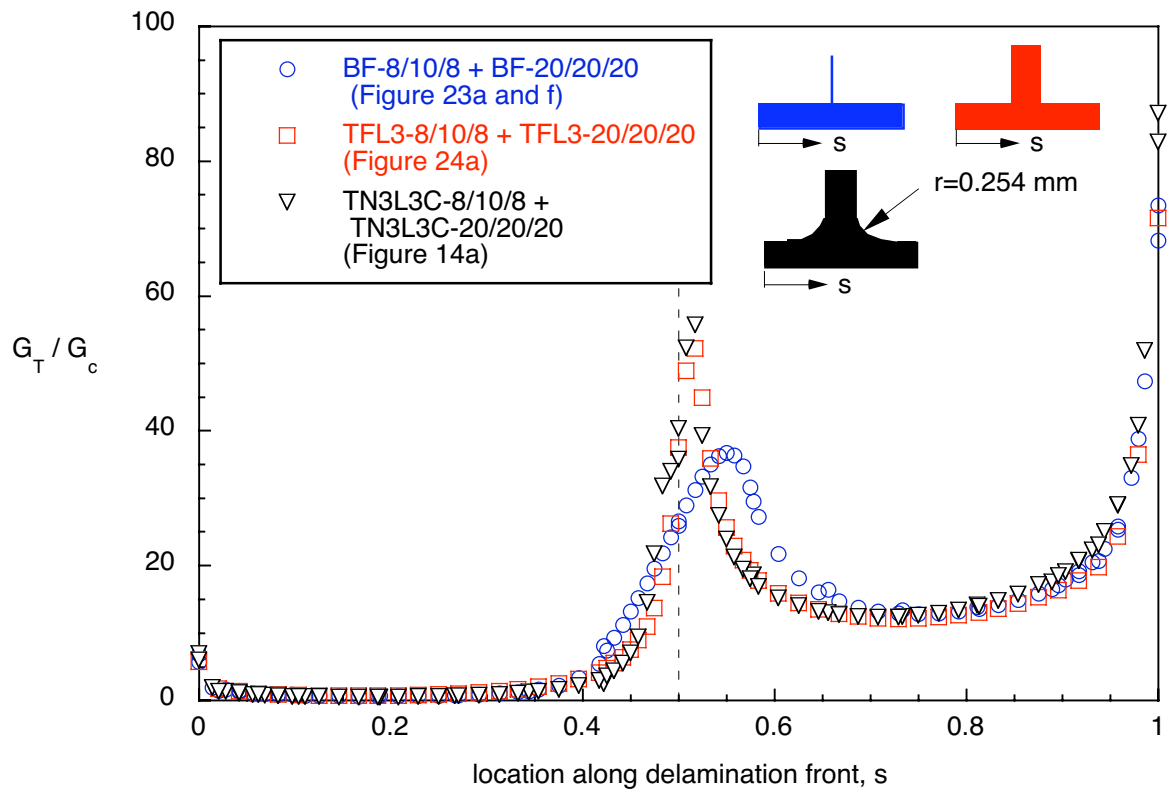


Figure 42. Computed failure index across the width of the stiffener for different local 3D models.

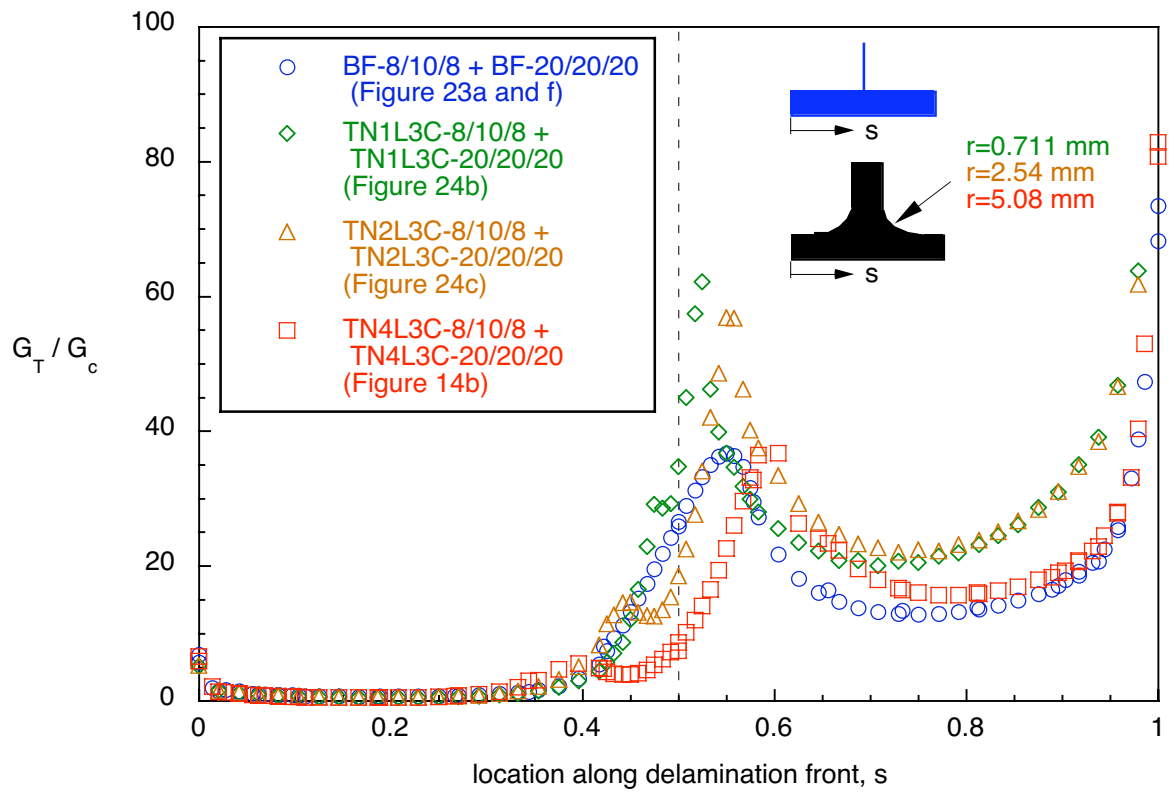


Figure 43. Computed failure index across the width of the stiffener for different local 3D models.

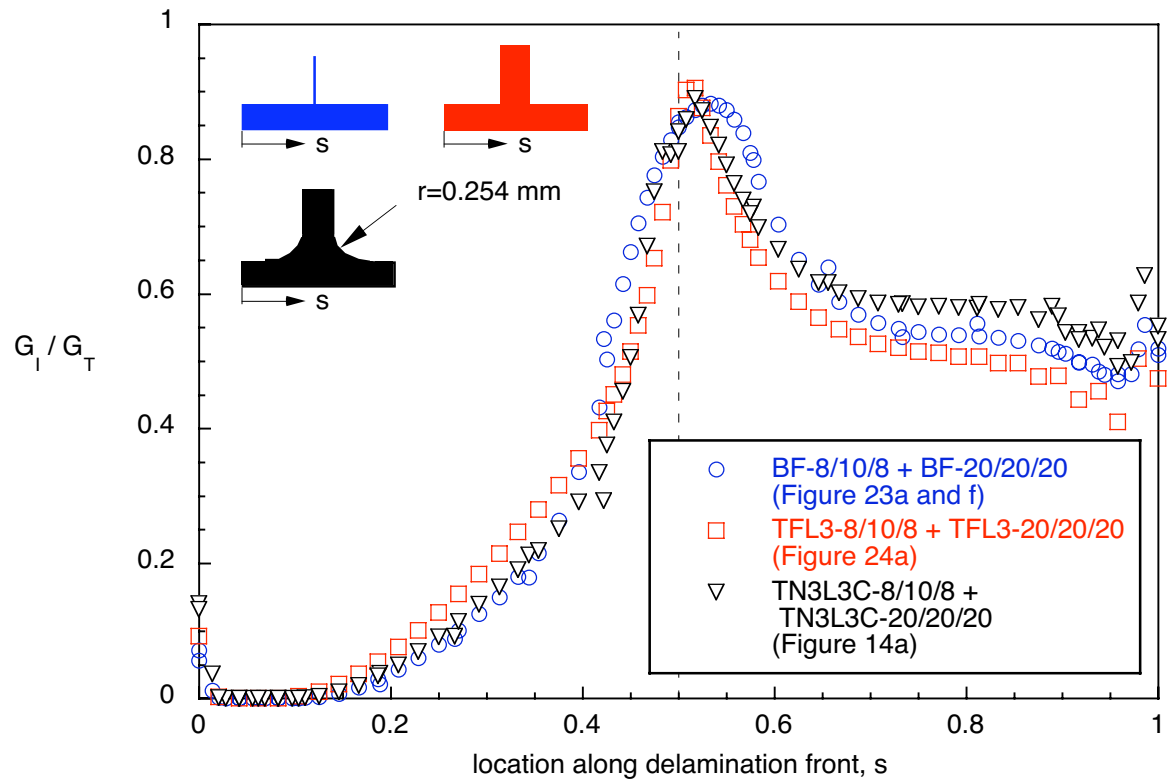


Figure 44. Computed mode I contribution across the width of the stiffener for different local 3D models.

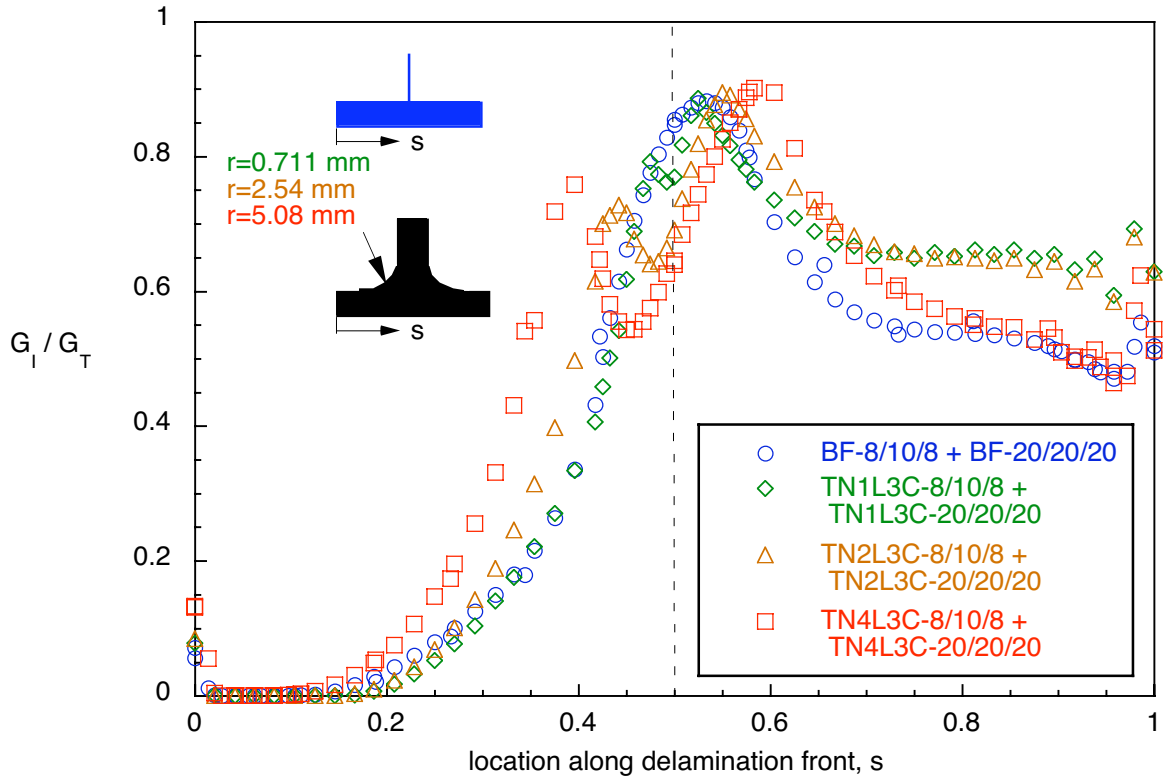


Figure 45. Computed mode I contribution across the width of the stiffener for different local 3D models.

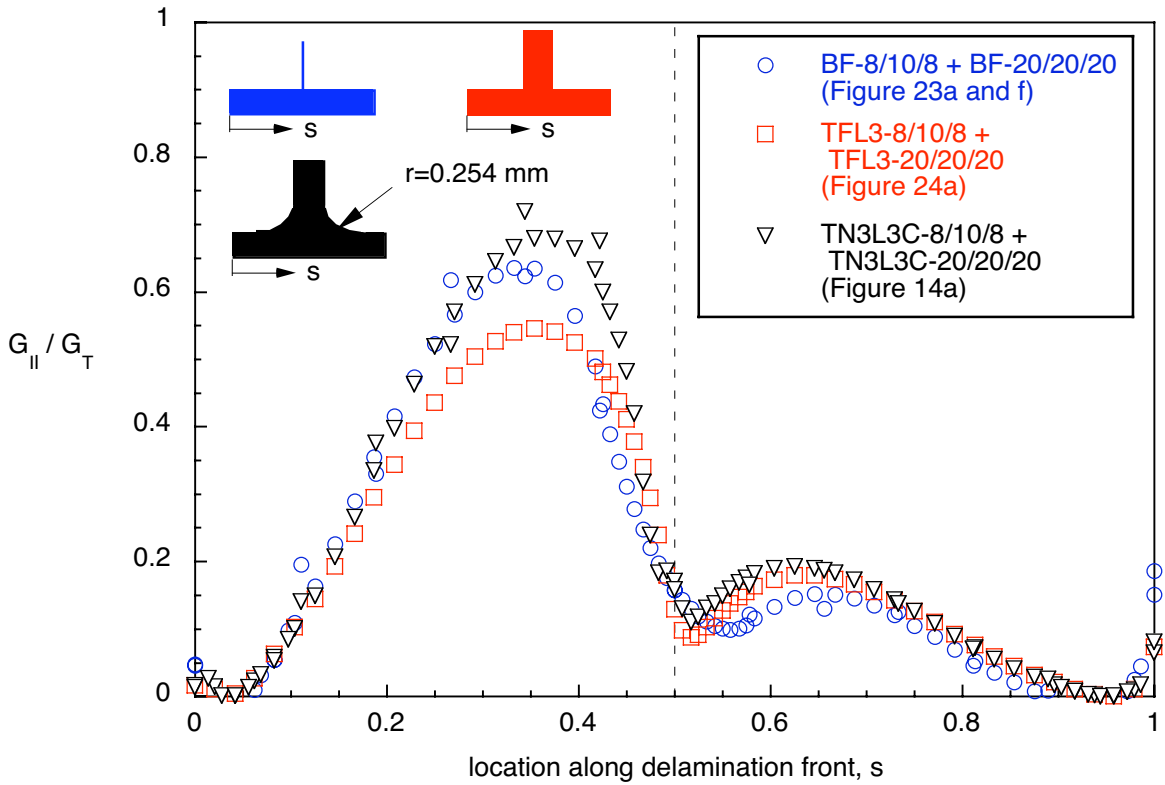


Figure 46. Computed mode II contribution across the width of the stiffener for different local 3D models.

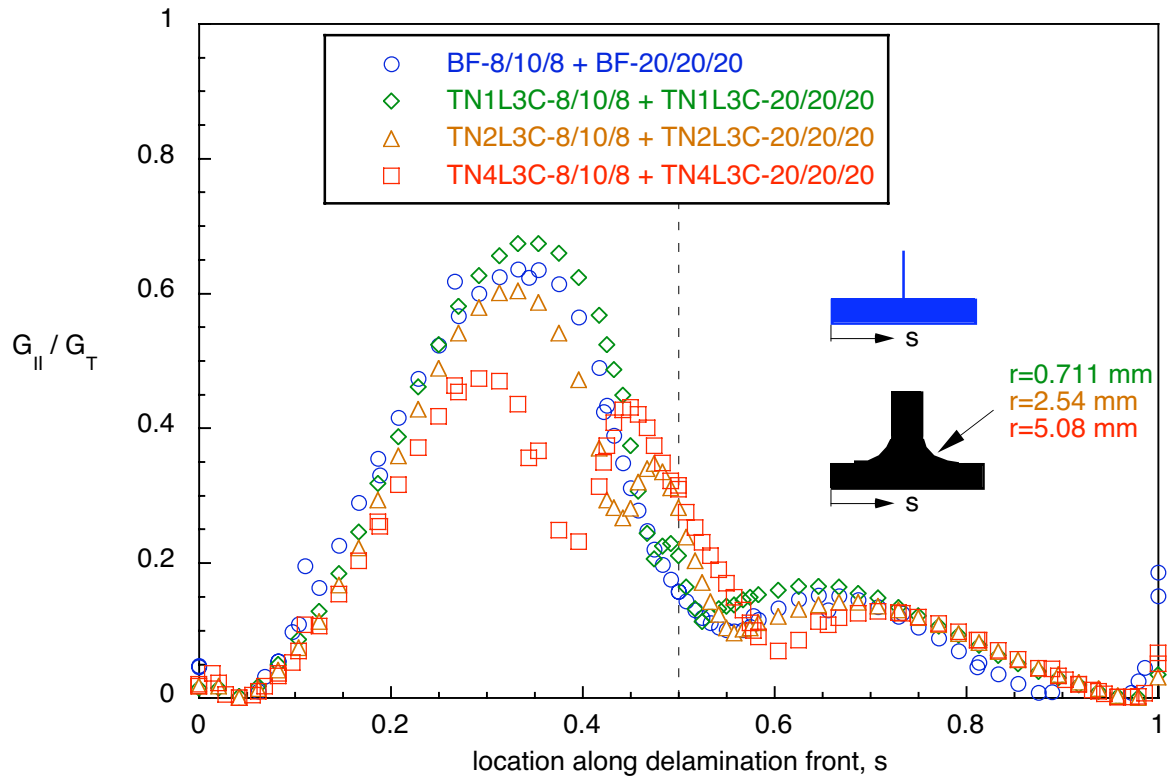


Figure 47. Computed mode II contribution across the width of the stiffener for different local 3D models.

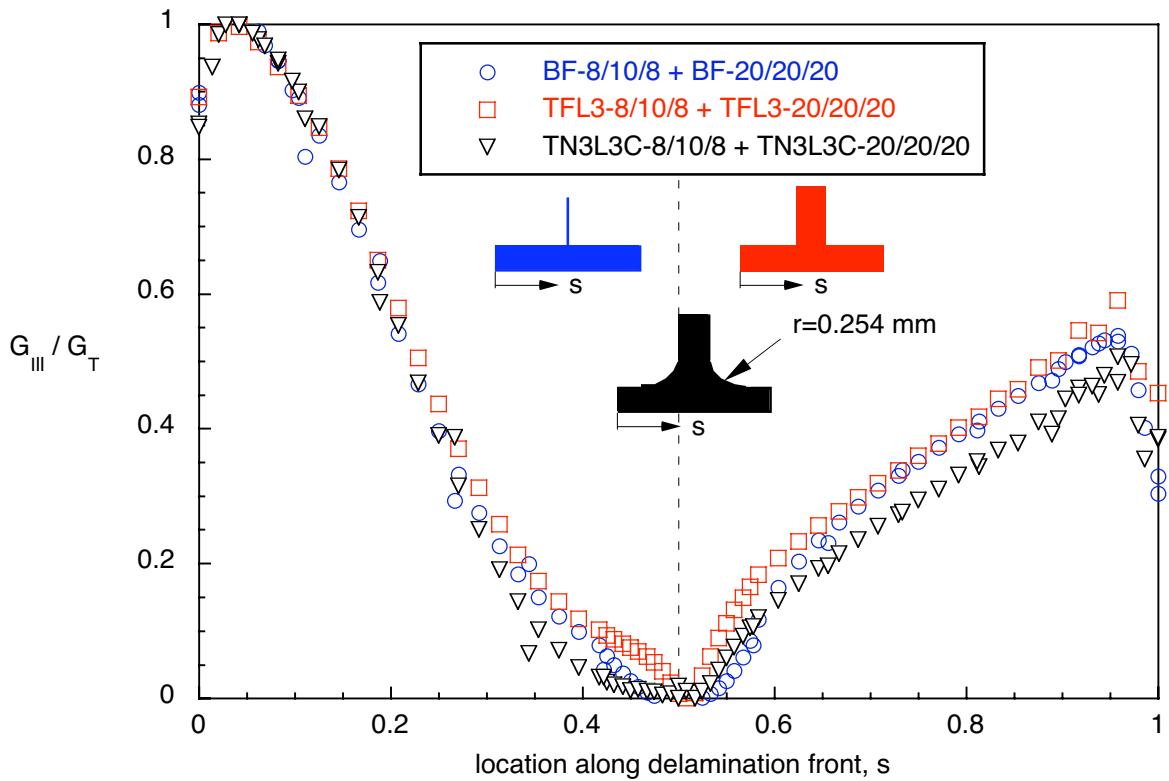


Figure 48. Computed mode III contribution across the width of the stiffener for different local 3D models.

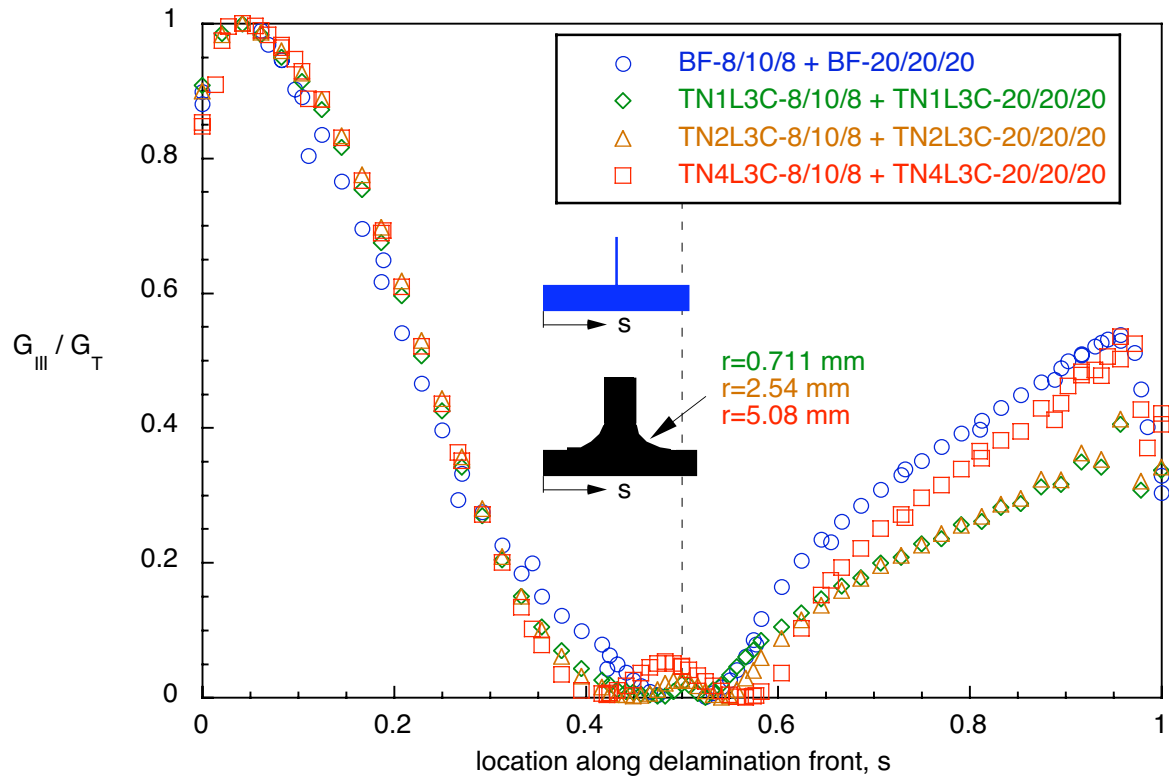


Figure 49. *Computed mode III contribution across the width of the stiffener for different local 3D models.*



REPORT DOCUMENTATION PAGE				Form Approved OMB No. 0704-0188	
<p>The public reporting burden for this collection of information is estimated to average 1 hour per response, including the time for reviewing instructions, searching existing data sources, gathering and maintaining the data needed, and completing and reviewing the collection of information. Send comments regarding this burden estimate or any other aspect of this collection of information, including suggestions for reducing this burden, to Department of Defense, Washington Headquarters Services, Directorate for Information Operations and Reports (0704-0188), 1215 Jefferson Davis Highway, Suite 1204, Arlington, VA 22202-4302. Respondents should be aware that notwithstanding any other provision of law, no person shall be subject to any penalty for failing to comply with a collection of information if it does not display a currently valid OMB control number.</p> <p><b>PLEASE DO NOT RETURN YOUR FORM TO THE ABOVE ADDRESS.</b></p>					
1. REPORT DATE (DD-MM-YYYY) 01/06/2007		2. REPORT TYPE Contractor Report		3. DATES COVERED (From - To)	
<b>4. TITLE AND SUBTITLE</b>  Analysis of Composite Panel-Stiffener Debonding Using a Shell/3D Modeling Technique				5a. CONTRACT NUMBER NAS1-02117	
				5b. GRANT NUMBER	
				5c. PROGRAM ELEMENT NUMBER	
<b>6. AUTHOR(S)</b>  Ronald Krueger James Ratcliffe Pierre J. Minguet				5d. PROJECT NUMBER	
				5e. TASK NUMBER 1002 and 2559	
				5f. WORK UNIT NUMBER	
<b>7. PERFORMING ORGANIZATION NAME(S) AND ADDRESS(ES)</b>  NASA Langley Research Center    National Institute of Aerospace (NIA) Hampton, VA 23681-2199        100 Exploration Way Hampton, VA 23666				<b>8. PERFORMING ORGANIZATION REPORT NUMBER</b>  NIA Report No. 2007-07	
<b>9. SPONSORING/MONITORING AGENCY NAME(S) AND ADDRESS(ES)</b>  National Aeronautics and Space Administration Washington, DC 20546-0001				<b>10. SPONSORING/MONITOR'S ACRONYM(S)</b>  NASA	
				<b>11. SPONSORING/MONITORING REPORT NUMBER</b> NASA/CR-2007-214879	
<b>12. DISTRIBUTION/AVAILABILITY STATEMENT</b>  Unclassified - Unlimited Subject Category 24 Availability: NASA CASI (301) 621-0390					
<b>13. SUPPLEMENTARY NOTES</b>  Langley Technical Monitor: Jonathon Ransom					
<b>14. ABSTRACT</b>  Interlaminar fracture mechanics has proven useful for characterizing the onset of delaminations in composites and has been used successfully primarily to investigate onset in fracture toughness specimens and laboratory size coupon type specimens. Future acceptance of the methodology by industry and certification authorities, however, requires the successful demonstration of the methodology on the structural level. For this purpose, a panel was selected that is reinforced with stiffeners. Shear loading causes the panel to buckle, and the resulting out-of-plane deformations initiate skin/stiffener separation at the location of an embedded defect. A small section of the stiffener foot, web and noodle as well as the panel skin in the vicinity of the delamination front were modeled with a local 3D solid model. Across the width of the stiffener foot, the mixed-mode strain energy release rates were calculated using the virtual crack closure technique. A failure index was calculated by correlating the results with a mixed-mode failure criterion of the graphite/epoxy material.					
<b>15. SUBJECT TERMS</b>  Fracture Mechanics; Delamination; Finite Element Analysis; Shell Analysis; Built-Up Structure					
<b>16. SECURITY CLASSIFICATION OF:</b>			<b>17. LIMITATION OF ABSTRACT</b>  UU	<b>18. NUMBER OF PAGES</b>  64	<b>19b. NAME OF RESPONSIBLE PERSON</b> STI Help Desk (email: help@sti.nasa.gov)
a. REPORT U	b. ABSTRACT U	c. THIS PAGE U			<b>19b. TELEPHONE NUMBER (Include area code)</b> (301) 621-0390